DEVELOPMENT AND REFINEMENT OF ALGORITHMS FOR IMAGE AND TOPOGRAPHY BASED CRATER DETECTION AND MORPHOLOGICAL ATTRIBUTE MEASUREMENTS

Thesis submitted to the Andhra University, Visakhapatnam in partial fulfilment of the requirement for the award of *Master of Technology in Remote Sensing and GIS*

Submitted By

DINESH GUPTA

Supervised By

Dr. R.S. Chatterjee
Scientist 'SF'
Geosciences and Geohazards Department

**Indian Institute of Remote Sensing, ISRO,
Dept. of Space, Govt. of India, Dehradun - 248001
Uttarakhand, India**

August, 2013

Disclaimer

This document describes work undertaken as part of a programme of study at the Indian Institute of Remote Sensing, Dehradun. All views and opinions expressed therein remain the sole responsibility of the author, and do not necessarily represent those of the institute.

Dedicated to my loving parents

Abstract

Impact craters are the most studied features in lunar and planetary science. They are the most outstanding features on the lunar surface and they are important for lunar geologic study. One of the important challenges in lunar research is to estimate lunar surface ages by calculating crater density per unit area. Therefore, proper crater detection, morphological attribute (shape and size) measurement and derived crater size frequency distribution (CSFD) of lunar craters is necessary. Identifying impact craters on planetary surfaces is one of the fundamental tasks in planetary science. Manually extracting craters from remotely sensed data is a difficult task because it requires specific knowledge as well as skills of extraction and a great deal of man power. Hence efficient and effective automatic crater detection method is needed. In this work, an integrated approach of automatic crater detection, image based as well as topography or Digital Elevation Model (DEM) based, using image and DEM data from Terrain Mapping Camera (TMC) sensor on-board CHANDRAYAAN-1 has been developed. Automatic crater detection algorithms (CDA) have been developed for image based as well as DEM based approaches. The algorithms consist of various crater detection techniques like Hough Transform and Wavelet Transform are used for image based approach and Marker Controlled Watershed Transform and Terrain Derivatives are used for DEM based approach. The final craters detected will be the integration of the one of the image based and DEM based crater detection techniques on the basis of the sharpness of the edges of detected craters and image detail preserving coefficient. Further for the computation of crater attributes (shape and size) of the detected craters, Moment Measure technique is being used for which algorithm has been developed. Finally, the CSFD is being computed for lunar (near side, far side and polar region) surface using TMC and MiniSAR (on-board CHANDRAYAAN-1) image data and hence, also the age for the global moon is determined. The crater shape and size attributes retrieved from Moment Measure technique appears to match with the CSFD results obtained with the help of Crater Tool. The lunar surface age obtained from the crater size frequency distribution with the help of CraterStat Tool appears to match well with the established stratigraphic age.

Keywords: Impact craters, Morphological Attributes, Hough Transform, Wavelet Transform, Watershed Transform, CSFD

Acknowledgements

Place: Dehradun   Dinesh Gupta
Date: 08-05-2013

Contents

List of Figures

List of Tables

1 Introduction

1.1 Background

Impact craters are geologic structures formed by the collision of meteoroids, asteroids or comets with planetary surfaces. They are common features on the surface of all planetary solid bodies in the Solar System, but are most abundant on bodies such as the Moon, Mercury, or Mars where they can accumulate over geologically long times due to slow surface erosion rates (Stepinski et al., 2012). They are among the most studied geomorphic planetary features because they provide useful information about the past geological processes like impact history and also provide a tool for measuring relative ages of the surfaces of various planetary or satellite bodies like moon (Urbach and Stepinski, 2009). They are the most outstanding features on the lunar surface and they are important for lunar geologic study. One of the important challenges in lunar research is to estimate lunar surface ages by calculating crater density per unit area(Yue et al., 2008). Therefore, proper crater detection, their morphological attribute measurement (shape and size) and derived crater size frequency distribution (CSFD) are important steps for surface aging (evolution) of the moon (Kim et al., 2005). Hence, proper detection of lunar craters has high priority among all these steps. Identifying impact craters on planetary surfaces is one of the fundamental tasks in planetary science. Manually extracting craters from remotely sensed data is a difficult task because it requires specific knowledge as well as skills of extraction and a great deal of man power. Hence efficient and effective automatic crater detection method is needed (Yue et al., 2008).

1.2 Motivation and Problem Statement

The task of automatic crater detection using remotely sensed images is very difficult. Previous studies in the field of crater detection largely engaged in the development of methods for automatic detection of craters from images (Bue and Stepinski, 2007) . The unsupervised (fully automatic) image based crater detection approaches primarily rely on pattern recognition techniques for identifying crater rims in an image as circular or elliptical features (Barata et al., 2004; Cheng et al., 2003; Honda et al., 2002; Kim et al., 2005). The original image is preprocessed to enhance the edges of the rims and subsequently detection is achieved by using Hough Transform (Hough, 1962), genetic algorithm (Honda et al., 2002), or radial consistency algorithm (Earl et al., 2005). The image based crater detection approaches must be optimized by combining supervised (which requires training samples from domain expert) and unsupervised algorithms to improve the detection rate. But, in spite of such complicated, multistep sophistications, image based algorithms are found to produce limited success over planetary surface because the image data is suitable for human visual interpretation and are skewed representations of the landscape. Image based crater detection algorithms have inherent limitations on the visibility of the craters as a function of quality of the images and depend on the factors namely illumination, surface properties and atmospheric state. One of the main limitations of running the crater detection algorithms on images is the presence of shadows on the image which depends on the illumination factor.

When the impact craters are imaged from an orbit, they show a roughly circular shape. Their contours are marked topographically by elevated rims thus producing shadows (Bue and Stepinski, 2007). But for the improved accuracy of surface chronology (dating), where only diameter and not the depth of the crater is required, detecting craters from images is still necessary (Stepinski et al., 2012).

On the other hand, detecting craters from topographic (DEM) data is, in principle, much easier than detecting them from imagery data. It is because craters are landforms that can be defined in terms of DEM derivatives calculated from DEM. This avoids numerous problems inherent to the detection of craters from optical images, such as illumination. Moreover, with the availability of high resolution digital topographic data over Mars and Moon in the recent years, the importance for developing DEM based crater detection algorithms is continuously gaining significance. A DEM is a raster data set where each pixel is assigned an elevation value. DEM derivatives are another raster data set, where each pixel is assigned a value calculated from the elevation values. Hence, DEMs are suitable for a quantitative geomorphic analysis and well suited for automatic crater detection (Bue and Stepinski, 2007). However, sometimes DEMs are limited in availability and resolution, so image based crater detection is still necessary (Stepinski et al., 2012).

A previous research by Bruzzone et al. (2004) stated about the development of image based automatic crater detection algorithm independent of the remotely sensed data and the target (planetary body). But for the better accuracy of results, integration (data fusion scheme) of image data with DEM data was recommended. Kim and Muller introduced an integrated approach for crater detection process by fusion techniques using both images and DEMs. But it worked well for detecting medium sized craters and failed to detect very large impact craters. Hence a robust and practical automatic crater detection algorithm (CDA) is required which should be able to detect craters of wide range of sizes. This is a significant challenge to the scientific community.

In this work, an integrated approach of automatic crater detection, image based as well as topography or Digital Elevation Model (DEM) based, using image and DEM data from Terrain Mapping Camera (TMC) sensor on-board CHANDRAYAAN-1, has been developed. Automatic crater detection algorithms (CDA) have been developed for both image based as well as DEM based approaches. The algorithms are independent of the planetary (target) body to be considered for crater detection as well as the remotely sensed data (in terms of resolution) acquired from different sensors (optical and synthetic aperture radar (SAR) sensors). The algorithms consist of various image segmentation techniques like Generalized Hough Transform and Wavelet Transform for image based approach and Marker Controlled watershed and Terrain Derivatives for Digital Elevation Model (DEM) based approach. The final craters detected will be the integration of the one of the image based and DEM based crater detection techniques on the basis of the sharpness of the edges (in terms of edge strength) of detected craters and image detail preserving coefficient (in terms of correlation coefficient between preproceesed image and image with detected craters). Further for the measurement of attributes (shape and size) of the detected craters, Moment Measure technique is being used for which algorithm has been developed. Finally, the crater size frequency distribution (CSFD) is being computed for lunar (near side, far side

and polar region) surface using TMC and MiniSAR (on-board CHANDRAYAAN-1) image data and hence, also the age for the selected test sites of moon is determined. The age dating of the test sites is computed using tool (Craterstat in ENVI) taking Crater Size Frequency Distribution (CSFD) as input which is computed using two techniques - Semi-automated (Crater tools in ArcGIS) and Automated (Moment Measure technique).

1.3   Research Identification

1.3.1   Research Objective

The main objective of the present study is to characterize the lunar surface based on crater shape, size and density.

1.3.2   Sub-objectives

- To detect craters automatically.
- To measure morphological attributes (shape and size).
- To analyse spatial variation in the shape, size and density of impact craters in selected test sites of equatorial, north polar and south polar regions over the lunar surface.
- To determine the age of lunar surface for the selected test sites using impact crater size frequency distribution.

1.3.3   Research Questions

For the fulfilment of objectives, present study aims at answering the following questions.
- Which algorithm is best suited for image-based and topography-based crater detection?
- How efficiently the regional descriptor based algorithm work for automatic retrieval of crater shape and size?
- What is the spatial variation pattern of crater shape, size and density for the selected test sites over the lunar surface?
- How does the age vary for the selected test sites over the lunar surface?

1.4   Research Setup

The methodology, adopted to fulfil the desired objectives is carried out in six phases, is described below. Preprocessing, Automatic Crater Detection from image and DEM data, Decision, Integration, Morphological Attributes measurements and Surface Dating of Moon based on CSFD are the different steps performed for fulfilling the objectives of this research work.

1.4.1 Phase 1: Pre-processing

The pre-processing step apply a sequence of filters to remove background features such as mountains that are too large not to be part of craters and to remove features that have shapes not like craters using Median filter, Area filter and Shape filter.

1.4.2 Phase 2: Automatic Crater Detection

This phase consists of two approaches for crater detection which are as follows.

1.4.2.1 Phase 2.1: Image Based Crater Detection

The image based crater detection approach consists of two techniques viz. Generalized Hough Transform and Wavelet Transform.

1.4.2.2 Phase 2.2: DEM Based Crater Detection

The DEM based crater detection approach consists of two techniques viz. Watershed Transform and Terrain Derivatives.

1.4.3 Phase 3: Decision

The integration of the two approaches will be done on the basis of decision parameters like edge strength and correlation coefficient which are calculated for the output images of detected craters using all the segmentation techniques.

1.4.4 Phase 4: Integration

The final craters detected will be the result of integration of one of the image based crater detection techniques and one of the DEM based crater detection techniques.

1.4.5 Phase 5: Morphological Attributes Measurement

For the measurement of crater attributes (shape and size) of the detected craters, Moment Measure technique is being used.

1.4.6 Phase 6: Surface Dating (Evolution) of Moon based on CSFD

The age of lunar surface for selected test sites is determined on the basis of the crater size frequency distribution (CSFD) which is computed semi automatically (using CraterTool in ArcGIS) and automatically (using moment measure technique).

1.5 Structure of the Thesis

This thesis has been organised into six chapters. The first chapter is Introduction which gives an overview of the basic concepts used in this research work and the research identification. The second chapter is Literature Review of the research done for understanding the topics related and relevant to this research work. Third chapter gives information about the Study Area and the Datasets used in this research. The fourth chapter is dedicated to the details of the complete Methodology. The fifth chapter explains and discusses all the Results obtained in this research and the sixth chapter discusses the Conclusions and future Recommendations.

2   Literature Review

The origin of the Earth and Moon are intimately related. Ancient samples of the Earth are likely to be found on the Moon's surface. Human exploration of the solar system starts at the Moon. Impact processes, which affected the Earth's evolution and biosphere, are best studied on the Moon. Impact craters have attracted a lot of attention in the scientific community and hence form a major research element. The disastrous effect of impact cratering phenomena on the environment provoked the scientists to study and understand the impact craters and their characteristics, to explore the effects of such craters on planets and to extract useful information from them which are important not only for scientific research but also for industrial and commercial purposes.

Craters are studied extensively because they provide us the relative age of the surface and more information about the geology of any planetary or satellite body (like moon) in the solar system (Sawabe et al., 2006). Craters play an important role to estimate the age of a planetary surface or surface unit when sample specimen is not available. The importance of impact craters stems from the wealth of information that detailed analysis of their distributions and morphology can bring forth. In particular, in the absence of in situ measurements, crater counting is the only technique for establishing relative chronology of different planetary surfaces (Wise and Minkowski, 1980; Tanaka, 1986). Identifying impact craters on planetary surfaces is one of the fundamental tasks in planetary science. Manually extracting craters from remotely sensed data is a difficult task because it requires specific knowledge as well as skills of extraction and a great deal of man power. Hence efficient and effective automatic crater detection method is needed (Yue et al., 2008). Because of the importance of craters in the field of planetary science, various automatic crater detection algorithms (CDA) have been developed.

Many research works came up with the idea of automatic identification of impact craters on Moon and other planetary bodies. With the help of remote sensing techniques, impact craters on other planetary surfaces could be explored and studied. Recently, many planetary exploration missions were flown and the data brought by these missions help us to reveal the unimagined information of planetary science. For example, high spatial resolution image and DEM data are available from the Terrain Camera (TC) sensor onboard Kaguya (SELENE) with a spatial resolution of 10 meters (Haruyama et al., 2009) and from the Terrain Mapping Camera (TMC) onboard Chandrayan-1 with a spatial resolution of 5 meters (Arya et al., 2012) for the lunar exploration. The availability of these high resolution data has drastically enhanced the detection limit of the craters.

2.1   Development of Automatic Crater Detection Algorithms

2.1.1   Image based Crater Detection Algorithms

In planetary context, high resolution grayscale (panchromatic) images are available, so the task is to find craters in grayscale images. Image based crater detection approaches can be divided into two categories: unsupervised (fully automatic) and supervised (which requires training samples from domain expert) methods. The unsupervised methods rely exclusively

on pattern recognition techniques to identify crater rims having circular or elliptical features in an image (Barata et al., 2004; Cheng et al., 2003; Honda et al., 2002; Kim et al., 2005). The general idea of all these methods is to first preprocess the image to enhance the edges of the crater rims, and then actual crater detection is done using various techniques like Hough Transform (Hough, 1962), genetic algorithms (Honda et al., 2002), or the radial consistency algorithm (Earl et al., 2005) that identifies regions of rotational symmetry. The supervised methods (Plesko et al., 2004; Vinogradova et al., 2002; Wetzler et al., 2005) depends on machine learning concept to train an algorithm for crater detection. In the learning phase, the training set of images containing craters labelled by domain experts is fed to the algorithm. In the detection phase, the previously trained algorithm detects craters in a new, unlabelled set of images. (Burl et al., 2001; Vinogradova et al., 2002) used a continuously scalable template model technique to achieve crater detection. (Wetzler et al., 2005) tested a number of algorithms and found that the support vector machine algorithm achieves the best rate of crater detection. The machine learning based supervised algorithms for crater detection work well for small craters and/or for relatively simple terrain, but their efficiency drops in proportion to the complexity of the terrain (Vinogradova et al., 2002). On the other hand, the pattern recognition based unsupervised algorithms for crater detection work well in the limited context of an autonomous spacecraft navigation system (Cheng et al., 2003) because of the relative simplicity of asteroid surfaces.

Use of image data for crater detection involves multistep procedures to identify craters however; it has its own limitations. Image shadowing, noise, distortions in the image are few factors which result in false crater detection (detection of non-crater structures) which leads to the wrong analysis of the crater characteristics. This led to the use of an alternate technique of detecting craters which utilizes digital topographic data (DEMs) instead of images. DEMs are much more fundamental descriptors of planetary surfaces than images. They are suitable for a quantitative geomorphic analysis and are well suited for automatic crater detection (Bue and Stepinski, 2007). The high resolution DEMs with near global coverage for several planets (Moon, Mars) are available. However there is still very limited work done using DEM data showing a lot of scope to implement different methods which have been applied on the images in many previous researches.

2.1.2 DEM based Crater Detection Algorithms

The research work by Salamuniccar et al. (2011) introduces a hybrid method of automatic crater detection based on topography (DEM) reconstructed from optical images from Moon Mineralogy Mapper (M^3) of CHANDRAYAAN-1 and one selected region of Lunar Reconnaissance Orbiter Wide Angle Camera (WAC) global optical image mosaic. This DEM based crater detection algorithm (CDA) is used for systematic cataloguing of lunar craters. The hybrid crater detection algorithm (CDA) used in this work is integration of the topography (DEM) based CDA and CDA based on crater shape based interpolation method (Salamuniccar and Loncaric, 2010; Salamuniccar et al., 2011). The hybrid CDA resulted in new and improved catalogue with detection of 3570 new lunar craters.

A combination of segmentation and detection algorithm for automatic crater detection on Mars using digital topography (DEM) was developed by Bue and Stepinski (2007). The method applies thresholding of the binary images and segmentation approach for delineation of craters by topographic curvature as it is a preferred parameter to extract topographic rims

of the craters. The algorithm gives a relatively easier tool for identifying small and fresh impact craters but fails to detect heavily degraded craters.

2.2   Development of Image Segmentation Techniques

Image segmentation in general is defined as a process of partitioning an image into homogenous groups such that each region is homogenous but the union of no two adjacent regions is homogenous (Pal and Pal, 1993). It means subdividing the image into regions which are called as objects and background and representing the result images with binary images, label the objects as "1"and the background as "0"commonly. Image segmentation has very wide role in many applications. All previous studies state that image segmentation is present in every kind of image analysis for extracting the information from the image. For example, in machine vision applications, it is viewed as a bridge between low level and high level vision subsystems (Spirkovska, 1993), in medical imaging as a tool to delineate anatomical structure and other regions of interest whose a priori knowledge is generally available (Pham et al., 2000). In remote sensing application, image segmentation is often used for the purpose of change detection and classification. Image segmentation algorithms development has been increased after the availability of high resolution remotely sensed image (Schiewe, 2002; Blaschke, 2010).

Some of the previous studies (Pal and Pal, 1993; Spirkovaska, 1993) state that image segmentation can be categorised based on discontinuity and similarity in the intensity value of image. Figure 2.1 shows the image segmentation hierarchy. Discontinuity based segmentation means partitioning of the image based on abrupt changes in intensity. This change in intensity is due to the presence of points, lines, edges or corners in the image. Hence segmentation is done using edge detection techniques viz. Sobel edge detector (filter). Sometimes the detected edges have gaps. Hence the edge linking technique (viz. Hough transform) is used to group these edges. Similarity based segmentation means partitioning of the image into many regions based on intensity similarity. The partitioning is done on the basis of threshold. The threshold may be global (thresholds the entire image with a single threshold value) and local (partitions a given image into sub images and determines a threshold for each of these sub images) which is decided on the basis of spatial variance. On the basis of the threshold, image is converted into binary image and finally all the similar regions are grouped using region growing techniques and hence the image gets segmented.

Guindon (1997) categorised image segmentation in two approaches: image driven and model driven approaches. It can be said that image driven approach forms object by combining pixels or group of pixels whereas model driven approach moves from splitting the whole image into image objects based on heterogeneity criteria (Benz et al., 2004). Apart from aforementioned categorisation, image segmentation can also be categorised as supervised and unsupervised segmentation. Unsupervised segmentation leads to feature extraction and clustering whereas supervised segmentation incorporates segmentation accuracy as an addition to unsupervised method.

Image based approach works directly on the image pixels and detects objects in the image (Zhang et al., 2010). It extracts edges of objects based on the statistical features of the image derived from the pixels. This is done with the edge based segmentation techniques. Edge based techniques detects edges and then closes the regions by contour generating algorithms. Sawabe et al. (2006) used edge detection techniques (Binarization, Fuzzy Hough transform) for detecting lunar craters with better accuracy. Edge detection is more used for feature extraction in remote sensing (Pham et al., 2000).

Model based approach assumes that objects in an image have certain pattern. Many models like Object-Background threshold model, Fractal model and MRF model have been studied previously for the purpose of image segmentation (Pal and Pal, 1993). Thresholding based object-background methods are not suited for the high resolution images because of high degree of variation of histogram and hidden clustering problem (Beveridge et al., 1989). High computational complexity and mathematical formulation are the drawbacks of MRF model and Fractal model. The newly transformation model (Watershed Transform and Wavelet Transform) showed significant results in the segmentation of the remotely sensed images. Watershed Transform (model) is a mathematical morphological approach based on analogy of flood situation (Beucher, 1992).
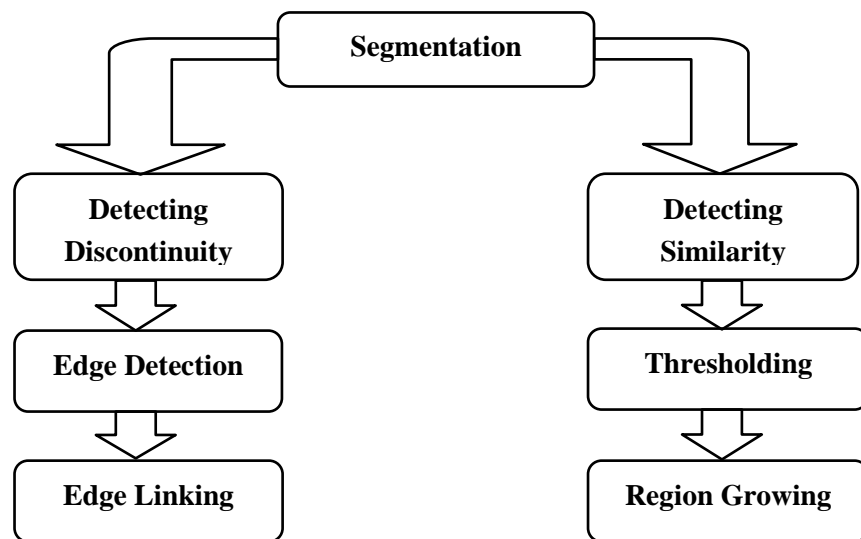
Figure 2.1 Image segmentation hierarchy

In this research work many image segmentation techniques have been used for lunar crater detection using image and DEM. A brief review about these image segmentation techniques used in previous research work is given below to understand their utility in the present work.

2.2.1 Wavelet Transform

Wavelet transform based edge extraction technique has been used in many previous researches. It has been used to detect the edges in the image at various decomposition levels. According to a paper by AL-HALABI and ABD (2005), Wavelet transform offers extracted edges with a natural decomposition of images at multiple resolutions. The efficient results came with the Haar wavelet due to its strictness at breakdown points (Bijaoui et al., 1996). Zhang and Desai (1997) developed a method for image segmentation based on automatic thresholding using multiresolution wavelet transform. The method adaptively chooses thresholds to segment the targets from background using multiscale analysis of the probability density function (PDF) of the image. In a research work carried out by Tamililakkiya (2011) Wavelet (haar) transform was used for extracting edges of linear features (ridges) from lunar images and results were found good.

2.2.2 Hough Transform

Hough transform plays an important role in image segmentation. It deals with the edge linking means it fills the gaps in edges and detects boundary of objects in image. Hough transform has been used widely in crater detection. In a research of recognition and detection of impact craters, Hough transform has been applied on the gradient magnitude image of extracted edges (using Sobel filter) of the craters in the image (Bruzzone et al., 2004). Tamililakkiya (2011) used Circular Hough Transform to detect the craters from lunar images efficiently. The Hough transform may be applied on the edges extracted through edge detection techniques like Wavelet transform followed by morphological operations. In a research work carried out by Bue and Stepinski (2007), Hough transform has been applied on the morphologically closed edges extracted with the combination of thresholded curvature map and connected components of craters in DEM based crater detection algorithm for detecting Martian craters. Kim and Muller introduced an integrated approach of crater detection using image and DEM data in which Hough transform was applied for grouping of edges of craters extracted from image as well as DEM with good detection accuracy.

2.2.3 Watershed Transform

Watershed transform has been widely used for fast computing and high accuracy in locating weak edges of adjacent regions in the field of image segmentation. It is a region based segmentation method based on mathematical morphology (Bhagwat et al., 2010). In a research carried out by Bue and stepinski (2007), segmentation has been done for detecting Martian craters using DEM. Watershed transform was used for segmenting the topographic basins into connected components with good accuracy.

Mathematical morphological functions efficiently deal with watershed segmentation oriented features such as size, shape area or connectivity for automatic image segmentation (Gao et al., 2001). The basic steps used for the segmentation process were simplification, marker extraction and boundary detection. Simplification is the removal of unwanted details from the image by using area morphology for extracting better segments. The markers based on luminance and colours were extracted to precisely locate the boundary of regions of interest. Marker extraction and boundary detection methods utilized colour measurement to

replace gray scale measurement and the spaces. The gray scale space was replaced by the RGB colour space and YUV colour space is replaced by the L ^a^ b colour space. The classical watershed algorithm was having over segmentation problem because of noise or textured patterns.

Gao et al. (2004) introduced a new marker based watershed algorithm to solve over segmentation issue. This technique involves generation of low frequency image generated from the gradient map for the extraction of markers using regional minima. Binary marker image is generated from the extracted regional minima method. This image has been used for suppressing the all intrinsic minima around the extracted markers. The results were obtained by applying watershed algorithm on the modified gradients to perform segmentation. The implementation of this method required less computation and simple parameters when compared to other methods to reduce the over segmentation issues of the watershed algorithm.

2.2.4   Estimation of Terrain Derivatives

DEMs are fundamental descriptors of planetary surfaces as compared to the images. They provide a quantitative geomorphic analysis and are well suited for automatic crater detection. Craters can be defined in terms of terrain morphometric attributes (slope, aspect, topographic curvature) calculated from the DEM. Bue and Stepinski (2007) gave a DEM based automatic crater detection approach in which craters are identified using a combination of segmentation (watershed transform) and detection (Hough transform) algorithms. Craters have been delineated by topographic curvature (in the gradient direction) which reflected the change of slope angle and found well indicator of crater rims on the basis of their concavity. Topographic curvature was found the preferred terrain parameter to extract topographic rims. Thresholding maps of curvature transforms DEM data into a binary image, from which craters are identified using a combination of segmentation and detection algorithms.

2.3   Attribute Measurement

To find an image from remotely distributed databases, the image should be described or represented by certain features. Shape is an important visual feature of an image used to describe image content. There are many shape representation and description techniques developed in the past. These techniques are generally classified into two classes of methods: contour based and region based methods based on whether shape features are extracted from the contour only or from the whole shape region. Contour based shape techniques use shape boundary information only while the region based shape techniques use all the pixels within the shape region rather than only use of boundary information.

Both classes are further divided into sub-classes: global (continuous) and structural (discrete) approaches on the basis of representation of the shape as whole or by segments/regions. Global approach does not divide the shape into sub-parts and a feature vector derived from the integral boundary is used to describe the shape in terms of shape

similarity. Shape similarity is measured usually as a metric distance (Euclidean distance) between the acquired feature vectors. On the other hand, discrete approach breaks the shape into segments (primitives) using particular criteria. The final shape representation is in the form of a string or graph. Shape similarity measurement is done either by string matching or graph matching.

These approaches are further distinguished into space domain and transform domain. The Boundary Moment descriptor is one of the global contour based shape descriptor. The boundary moments are used for reducing the dimensions of the boundary representation. The normalized moments which are invariant to shape translation, rotation and scaling are computed mathematically. This method is easy to implement (Zhang and Lu, 2004).

Shape representation is a prerequisite for similar shape retrieval. For the analysis of 2D shapes, moment measurements have been considered to be very powerful. Size, central location and orientation of the shape feature are the essential descriptors which are moment based attributes (You and Bhattacharya, 2000).

2.4   Surface Age Dating

Dating of planetary surfaces is one of the important task for understanding a planet's origin and evolution. Crater counts can be used to determine relative and absolute ages if the crater production rate and crater size frequency distribution (CSFD) are known (Hartmann, 1966; Oberbeck et al., 1977; Ivanov, 2001). The crater chronology method is based on the simple idea that older surfaces accumulate more craters than the recent ones (Le Feuvre and Wieczorek, 2011). Based on the radiometric dating of existing lunar rock samples, there is linear (constant) cratering rate back to around 3 Ga ago and approximately exponential beyond that time. The relationship can be approximated by a function which is in cumulative form (Michael and Neukum, 2010; Neukum et al., 2001; Stöffler and Ryder, 2001).

According to Michael and Neukum (2010), the determination of the age of the Lunar surface is based on two age functions which are described here.

- **Production Function:** It describes that how many craters of a given size are formed in relation to the number of any size. The assumption here is the CSFD should be of homogeneous surface units of any planetary body (Moon or Mars). Since the older units are characterised by more number of craters and the younger units by lesser number of craters, the production function is constructed by piecewise normalization procedure for the entire diameter range. Figure 2.2 (a) shows CSFD plot who's X-axis represents crater diameter and Y-axis represents crater cumulative frequency.

- **Chronology Function:** The empirical relationship between the crater frequencies plotted versus the radiometric age. The crater chronology function is based on the measurements of the crater size frequency distribution (CSFD), which are linked to

11

the radiometric ages of lunar rocks carried by Apollo missions (Werner and Tanaka, 2011). Figure 2.2 (b) shows cratering chronology function where X- axis is the surface age and the age exponentially increases after 3Ga.
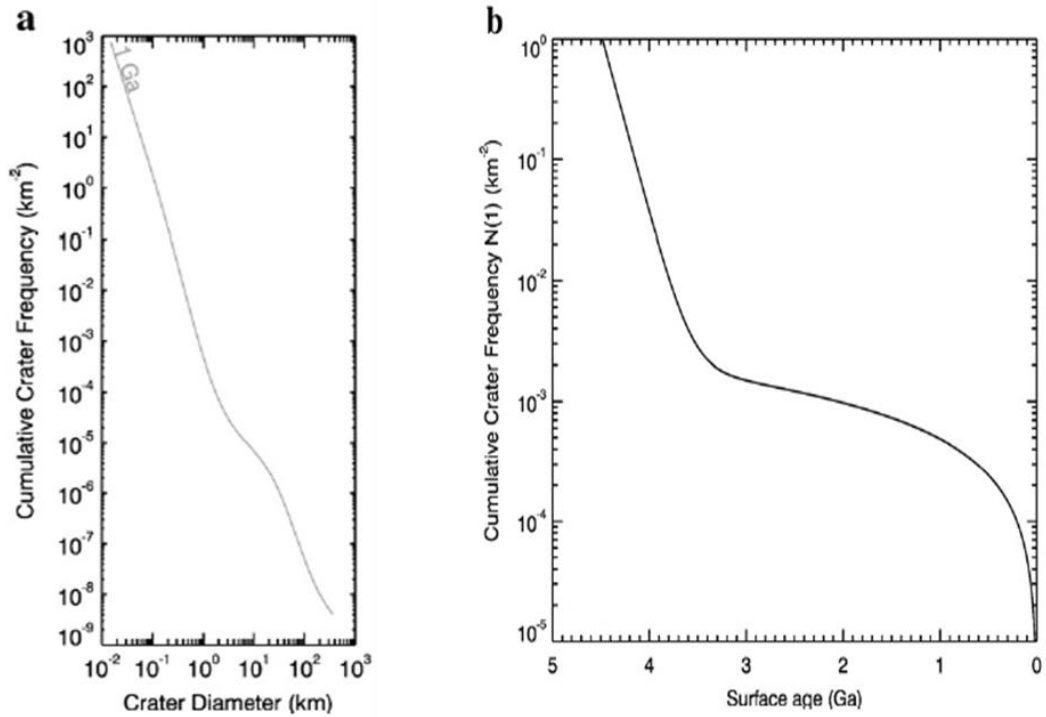
Figure 2.2 Age determination graph for Lunar Chronology

3 Study Area and Data Used

Ancient samples of the Earth are likely to be found on the Moon's surface. Impact processes, which affected the Earth's evolution and biosphere, are best studied on the Moon. To analyse the lunar surface for understanding the age of the moon in relation to impact cratering, we have selected Equatorial region and polar region (North Pole and South Pole region from selective sites of Nearside and Farside) of the moon as the study area in this research.

3.1 Study Area of Equatorial Region

The equatorial test site of lunar surface is shown by an image and DEM is shown in Figure 3.1(a) and (b) respectively. This test site (shown by image and DEM) is used for the portability of the image and DEM based segmentation techniques as well as attribute measurement technique for computing crater attributes. The test site locations for both image and DEM are same and shown in Table 3.2 taken from Indian Space Science Data Centre (ISSDC).

(a)   (b)
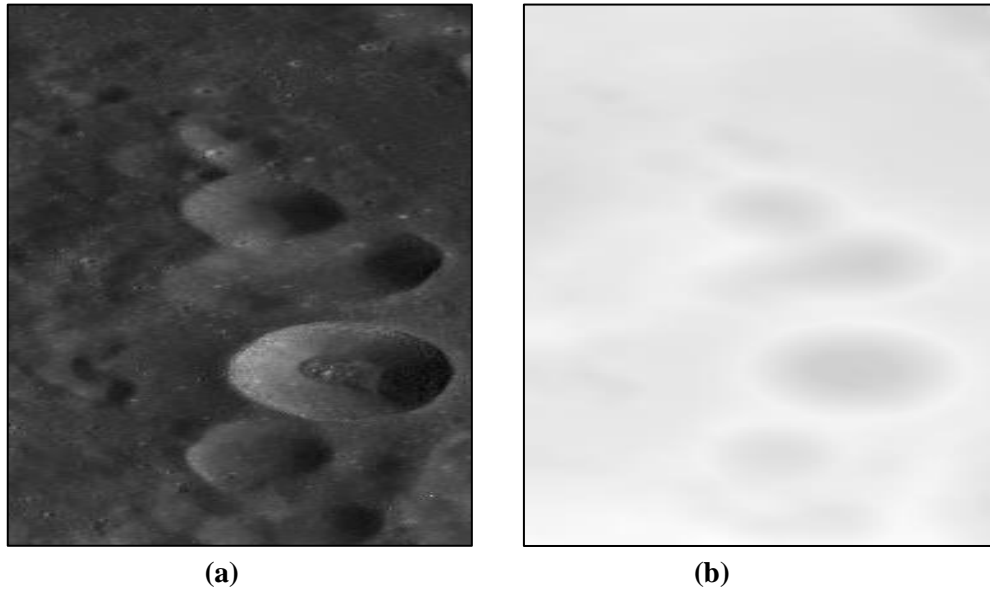
Figure 3.1 Equatorial test site of moon

3.2 Data Sets of Equatorial Region

Chandrayaan-1, the maiden Indian mission to Moon was launched during 22 October, 2008. The main objective of the mission is the photo-selenological and chemical mapping of the Moon. TMC is the prime imaging payload to collect stereoscopic data of lunar surface. It has 5 m spatial resolution and 20 km swath operating in panchromatic band (500-880 nm).

It is an optical imaging payload comprising three cameras with different view angles viz., fore, aft and nadir, accomplished through the use of suitably displaced linear arrays in the focal plane of a single lens. The Selenographic projection has been used for equatorial region. The image based and DEM based crater detection algorithms and the crater attribute measurement technique are applied on both data (image and DEM). The ortho image and digital elevation model (used in this research work) generated from its stereo pair enable a better study of the morphology of various lunar features like craters. The TMC image and DEM data has been taken from the ISRO Science Data Archive (ISDA) node handled by Indian Space Science Data Centre (ISSDC). The data is freely available and has been downloaded from www.issdc.gov.in.

Table 3.1 Location of the test site for equatorial region of moon

Top Left		Top Right		Bottom Left		Bottom Right	
Latitude	Longitude	Latitude	Longitude	Latitude	Longitude	Latitude	Longitude
15.925	226.827	15.925	228.184	10.156	226.827	10.156	228.184

3.3 Study Area of Polar Region

Test sites have been taken from both the poles –North Pole and South Pole from selective sites of Nearside and Farside of the lunar surface. The test site locations are shown in Figure 3.2 and its central Latitude and Longitude located from Virtual Moon Atlas developed by Legrand and Chevalley (2013) are described in Table 3.2.
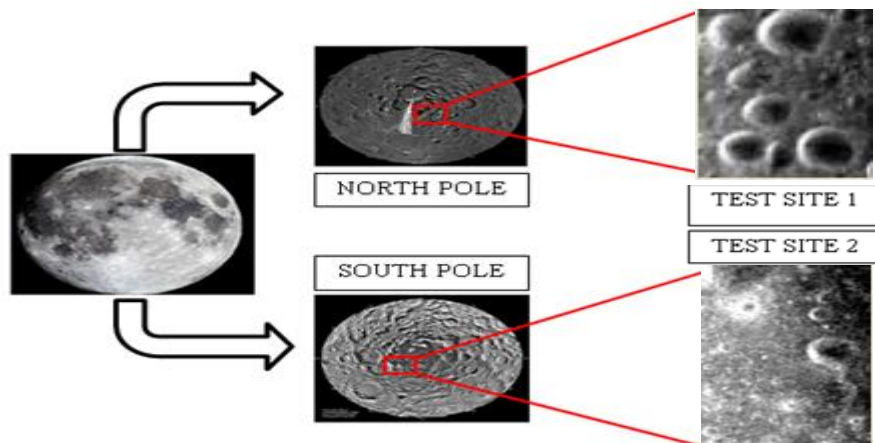
Figure 3.2 North Pole and South Pole test sites of moon (MiniSAR is overlaid on UVVIS Clementine data)

Two test sites have been selected for the current research study. One test site is selected from the North Pole of the near side region and one test site is selected from the South Pole of the far side region of the moon. Both the test sites are used for the portability of the developed image based segmentation techniques as well as for Moment Measure technique for computing crater attributes. The test site in the North Pole is basically in the hilly terrain

while the test site in the South Pole which is permanently under shadow region of the moon is in different geomorphic location.

Table 3.2 Location of the test sites for polar region of moon

Test Site	Description Location (Crater)	Lunar Coordinates	
		Latitude	Longitude
1	Near Peary Crater (Nearside)	87.5	8.8
2	Near Drygalski P Crater (Farside)	-83.0	-93.7

3.4 Data Sets of Polar Region

Miniature Synthetic Aperture Radar (Mini-SAR) on-board Chandrayaan 1 which was launched on 22 October 2008 is an instrument with single frequency S-band (12.6 cm wavelength) with spatial resolution of 75 m per pixel. It employs a unique hybrid polarization architecture, which allows the determination of the Stokes parameters from the reflected signal. The MiniSAR data is level-2 processed dataset in planetary data system (PDS) format that stored radar backscatter response in 4 channels respectively.

Mini-SAR data comprises two intensity images primarily, horizontal (H) and vertical (V) and two cross power intensity images between the H and V received, it exhibits hybrid-polarity SAR where the transmitted field is circularly polarized, and the subsequent resulting backscatter is received in two mutually coherent linear polarizations (Raney, 2006). The four channel bands of MiniSAR are processed to generate the Stokes parameter (Das and Chakraborty, 2011) as given in following equations below

$$S_1 = <|LH|^2 + |LV|^2> \tag{3.1}$$
$$S_2 = <|LH|^2 - |LV|^2> \tag{3.2}$$
$$S_3 = 2Re<LH.LV^*> \tag{3.3}$$
$$S_4 = -2Im<LH.LV^*> \tag{3.4}$$

Where, S1, S2, S3 and S4 are the Stokes parameters. S_1 and S_2 represent the horizontal and vertical intensity images respectively and S_3 and S_4 represent real and imaginary images hybrid polarimetric data of MiniSAR respectively. In this work, intensity images (S_1 and S_2) are used with Polar Stereographic projection. MiniSAR data is freely available at Planetary Data System node and has been downloaded from http://pds.nasa.gov.

4 Methodology

The methodology of this research work is shown below in the flow diagram in Figure 4.1. The methodology adopted for this work is explained here. Various approaches and techniques are adopted starting from the preprocessing of image and DEM data, development of automatic crater detection algorithms for image based and DEM based approaches using image segmentation techniques, integration, development of attribute measurements technique and computing crater size frequency distribution (CSFD) and finally getting age of moon on the basis of computed CSFD.
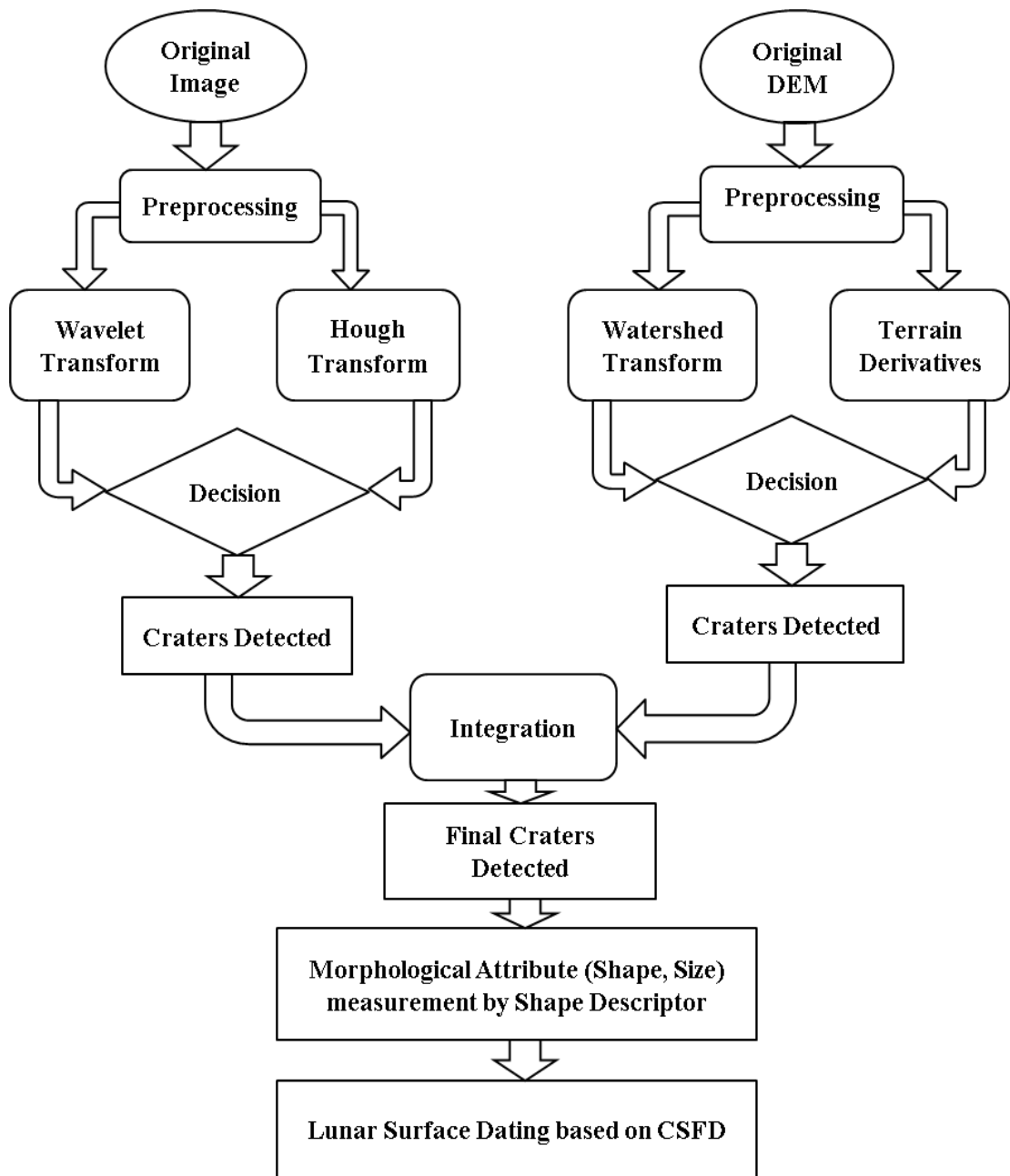
Figure 4.1 Flow of the Research Work

4.1   Pre-processing

An image of a planetary surface contains many features that are not parts of craters such as highlight and shadow. It means the non-crater features also exist which is of no interest to our present method. Thus, it is necessary to remove all such features. In the present work, a series of filters have been implemented in MATLAB to remove such features. The preprocessing has been done for TMC and MiniSAR (North Pole and South Pole) images as well as for TMC DEM. For the current methodology, the preprocessing consists of three steps which are described one by one below.

4.1.1   Noise Filter

A median filter has been applied to the original image and DEM to remove the noise present in the background of image. A median filter consisted of a moving window (5x5) is run over the image and DEM and computed the output pixel as the median value within the input window. The resulting median filtered image having smoothness show only the global features (craters) without any noise in the background. The median filter has also removed the speckle noise present in the MiniSAR image.

4.1.2   Area Filter

An area filter is an attribute filter which uses the number of pixels in a feature as its attribute. The filter has been applied on the binary images obtained by thresholding the median filtered images and DEM using Otsu's method, which chooses the global threshold to minimize the intraclass variance of the black and white pixels (Otsu, 1979). This filter removes all the non-crater features that are not part of craters and also those features that are considered too small for reliable crater detection. Features with less than 1000 pixels have been removed using area filter. The area filter opens the binary image morphologically. The area filtered image is binary image.

4.1.3   Shape Filter

After removal of the noise and non-crater features using median and area filters respectively, the next step is to remove features that have shapes incompatible with craters. For this purpose we have implemented a disk shape filter as a circular averaging filter with radius 5 pixels and run it on the image and DEM. The area filtered binary images and DEM have been converted back into grayscale integer images using 'im2uint16' command in MATLAB and then shape filter has been applied on the gray tone images and DEM. The shape filter preserves and removes features from the image based on their shapes.

4.2   Crater Detection Techniques

In this work, various crater detection techniques have been used for image based and DEM based crater detection approaches. The image based crater detection approach uses Generalized Hough Transform and Wavelet Transform as the crater detection techniques while the DEM based crater detection approach uses Watershed Transform and Terrain Derivatives estimated from DEM as the crater detection techniques. For this purpose, automatic crater detection algorithms have been developed in MATLAB which are described below.

4.2.1 Wavelet Transform

In the current methodology, Wavelet transform based image segmentation technique has been used for the image based crater detection approach. Wavelet transform has been applied on the preprocessed image (TMC and MiniSAR) to get multiscale 2-D wavelet decomposition of gray scale preprocessed image and the corresponding detailed coefficients (horizontal, vertical and diagonal edges responses). The Wavelet decomposition has been done using Haar wavelet transformation since it has been found simplest transformation method of all and effectively served the edge detection purpose. An object in the image which is smaller than the spatial resolution of image can't be identified. Therefore high resolution image is required to solve this problem. If the object size is larger than the spatial resolution then the object may get split. Hence multiscale (multiresolution) approach arises to solve this issue (Dey et al., 2010). The following steps have been followed for implementing edge detection using Wavelet Transform in MATLAB (Mallat, 1989; Open discontdemo.m Matlab 2012 (a) Help).

- Read the original image.
- Preprocessing of the image is done.
- Multiscale 2-D Wavelet (Haar) decomposition of gray scale image has been done. The Haar wavelet applies a pair of low pass and high pass filters to image decomposition. Upto five levels (scales) of decomposition have been done to get the detailed edges of craters for TMC image and three levels for MiniSAR images. The inbuilt function 'wavedec2' of MATLAB has been applied on the image for all the five levels and it returns corresponding wavelet decomposition structure having the decomposition vector C and the corresponding matrix S for all the five levels. The size of vector C and the size of matrix S depend on the type of analyzed image. In our case, C is having (3n+1) sections and size of S is (n+2) - by – 2, where n is the level of decomposition.
- After decomposition of the image at five levels, it is reconstructed for corresponding levels.
- The corresponding detailed coefficients (horizontal, vertical and diagonal edge responses) for all the five levels have been achieved by passing the wavelet decomposition structure, obtained in previous step, to a MATLAB inbuilt function 'detcoef2' as input parameters.
- Visualize all the detailed coefficients for each level as an image.
- Continuous Wavelet Transform using Haar wavelet has been applied on the image with a scale (s) varying from 1 to 32 to get image details in the form of continuous wavelet coefficients using MATLAB inbuilt function 'cwt'.

The main advantage of Wavelet Transform is that it gives the edge details at multiple scales in time-frequency domain. It also gives facility to get details of edge discontinuity at local position. Continuous Wavelet Transform (CWT) detects the abrupt transitions (edges) in the image. The abrupt transitions affect the CWT coefficients at all scales. Abrupt changes in an image or signal produce relatively large wavelet coefficients (in absolute value) centred around the discontinuity at all scales. Because of the support of the wavelet, the set of CWT coefficients affected by the singularity, increases with increasing scale. This is the definition of the cone of influence. The most precise localization of the discontinuity based on the CWT coefficients is obtained at the smallest scales.

4.2.2 Generalized Hough Transform

Hough transform is generally used for edge linking and boundary detection purposes in the image segmentation process. Results of edge detection methods may contain sparse points, instead of straight lines or curves. Therefore, there is need to fit a line to these edge points. In the methodology of this work, generalized Hough transform has been used as an image segmentation technique in image based crater detection approach applied on TMC and MiniSAR images. The generalized Hough Transform has been implemented in MATLAB, as per the given equations (Ballard, 1981) for the input preprocessed image.

- Read the original image.
- Preprocessing of the image is done.
- The Sobel edge detector has been used to get all the edges of objects (craters) in the preprocessed image. Hence binary egde image is obtained.
- Horizontal and vertical edge components (GH and GV) are obtained from the Sobel edge detector.
- Finally for each detected edge pixel, the shortest distance, r, (Euclidean distance) from edge point (GH, GV) to the reference point (X_c, Y_c) has been calculated as per the equation 4.1. Initially(X_c, Y_c) are coordinates of origin (0, 0).
- Direction, β, (angle) has been calculated using GH and GV as per the equation 4.2. It is the inverse tangent angle of the ratio of GV to GH. This direction is also called aspect.
- Update the values (X_c, Y_c, r, β) for each value of distance and angle as per the equations 4.3, 4.4, 4.1 and 4.2 respectively.

$$\text{Distance}, r = \sqrt{((GH - X_c)^2 + (GV - Y_c)^2)} \tag{4.1}$$

$$\text{Direction}, \beta = \tan^{-1}\left((GV - Y_c) \middle/ (GH - X_c) \right) \tag{4.2}$$

$$X_c = GH + r * \cos(\beta) \tag{4.3}$$

$$Y_c = GV + r * \sin(\beta) \tag{4.4}$$

The main advantage of generalized Hough transform is that it can tolerate noise and gaps in edge image and it is invariant to scale changes, rotations and foreground/background reversals.

4.2.3 Watershed Transform

A watershed is the ridge that divides areas drained by different river systems. The watershed lines determine the boundaries in an image that separate image regions. In the topographic representation of an image, the watershed transform computes the catchment basins and ridge lines. The catchment basins correspond to the image regions and ridge lines correspond to the region boundaries. The watershed transform is often applied for separating touching objects in an image. It finds "catchment basins" and "watershed ridge lines" in an image by treating it as a surface where light pixels are high and dark pixels are low. In this research work, marker controlled watershed transform has been used as image segmentation technique under DEM based crater detection approach. It has been applied on the optical

DEM data of TMC. A connected component belonging to an image is termed as a marker (Gonzalez et al., 2009). A set of internal markers which are inside of the object of interest and a set of external markers which are contained within the background are generated. Gradient image generated from the gray scale image is modified using these generated markers. There is a one to one relationship of marker to a specific watershed region. Thus the number of markers generated will be equal to the final number of segmented regions by watershed transform. The algorithm implemented in MATLAB for generating marker controlled watershed transformation, shown in figure 4.2, is as follows.

- Read the original DEM.
- Pre-processing of the DEM is done.
- Find the gradient magnitude image using sobel filter.
- Applying watershed transformation directly on the gradient image generates over segmentation which is a serious problem. So to avoid this, marker computations is done.
- The foreground markers are generated by using the morphological operators such that it must generate the connected blobs of pixels inside each of the foreground objects. These operators also used for enhancing the object of interest and then finally, performing the regional minima function for marking the crater as objects.
- The background markers are also generated to segment the background so that it should not be too close to the boundaries of the objects. The watershed transform based on the distance transform can be used for thinning the background.
- The final step is to compute the watershed transform of the marker images. The superimposition of the marker image on the mask image (gradient magnitude image) needs to be done to run the watershed function to extract the final object boundaries.
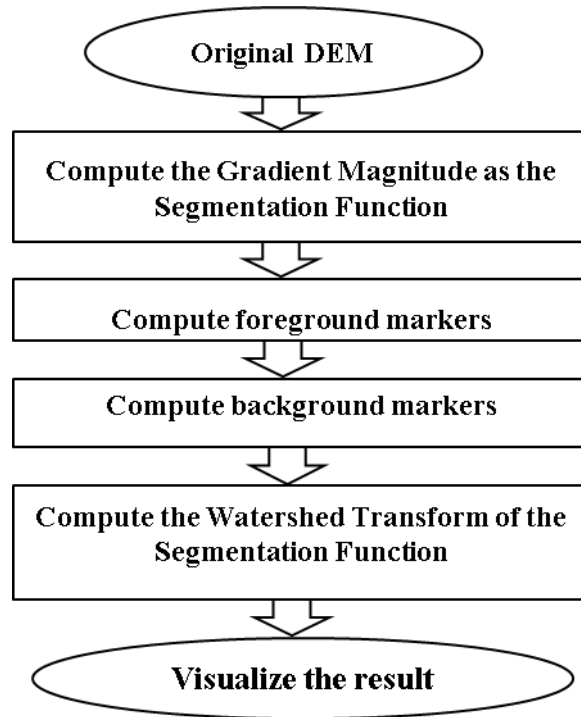
Figure 4.2 Flowchart of Marker Controlled Watershed Transform

The discussed watershed algorithm consists of the following functions (in MATLAB) to delineate the precise boundary of the craters.

- In this research work the gradient magnitude of the DEM is calculated which represents the gray scale transition from base of the craters to the crater rims as the intensity in the preprocessed input image. The gradient magnitude image clearly represents the craters and crater boundaries from the background. The foreground and background markers when used with the gradient magnitude image extract precise boundaries of the craters.

- Morphological operations are used for the analysis and processing of geometrical structures on the basis of set theory and topology. These operations are done on binary images and gray scale images based on morphology and shapes. Each output pixel has a value which is based on the corresponding input pixel and its neighbours (Jähne, 2004). The size and shape of the neighbourhood can be selected such that a morphological operation constructed is sensitive to specific shapes in the input image.

- The fundamental morphological operations are erosion and dilation. Dilation states that if a pixel in the input pixel's neighbourhood is one, the output pixel is also one otherwise zero in the case of binary image, whereas it increases the brightness of objects when applied to the gray scale images (Jähne, 2004). It is performed by taking the neighbourhood maximum when passing the structuring element over the image. Dilation results in growing of the area of the object (crater) and thus removal of small holes in the object. In erosion if every pixel in the input pixel's neighbourhood is one the output pixel is one otherwise zero. While in the dilation, erosion when applied to the gray scale images reduces the brightness and thus

21

reduces the size of the bright objects on a dark background. It is performed by taking the neighbourhood minimum while the structuring element is passed over the image. Erosion results in shrinking the object's area and small isolated regions disappear. The structuring element size and shape is responsible for the number of pixels added or removed from the objects in an image (Jähne, 2004).

- The morphological opening and closing operators are the mixture of erosion and dilation operators. The morphological opening of an image is defined by performing erosion function followed by dilation function with the same structuring element used for both operations. On the other hand the morphological closing is the reverse as it performs dilation function followed by erosion function with the same structuring element (Gonzalez et al., 2009).

- The structuring element has been used as an essential part of all the morphological operations in the marker controlled watershed transformation. It consists of a matrix (with 0's and 1's) that can have arbitrary shape and size. The neighbourhood is defined by the pixels with the value of 1. The 'disk' structuring element has been used in this research work. It creates a disk shaped, flat structuring element along with the radius (R) specified. The radius must be a positive integer and neighbour connectivity (N) should be 0, 4, 6 or 8. When N is greater than 0, the approximation of the disk shaped structuring element is done by a sequence of N periodic–line structuring elements. No approximation is used when N equals 0 and in this case the structuring element members consist of all pixels whose centres are not greater than radius away from the origin. The default value of N is 4 when N is not specified.

- The gray scale image can be considered as a three dimensional image where the x and y axis represent position of the pixel and the z axis denotes the intensity of each pixel. The intensity values can be stated as the elevation of the pixel. The high intensity values and the low intensity values of the image can be considered as the peaks and valleys in topographical terms respectively. The markers at the low intensity valued pixels of the image are determined using the concept of regional minima. The regional minima function takes gray scale image as input and generates a binary image as output. The values are set to 1 for the regional minima pixels and all other are set to 0.

- The superimposition of the marker image on the gradient magnitude image can be done to perform the final watershed transformation on the image. The imposition of the marker image consisting of regional minima generated by the morphological functions to extract the objects of interest from the mask image is done. The marker image creates new minima in the mask image and eliminates all the values of other pixels in the image.

- The process of Skeletonization is used to remove the boundaries of the objects (craters) without breaking the object apart and without changing the essential structure of the image. The remaining pixels build up the image skeleton.

- Distance Transform has been used for measuring of the separation of points in the image. The distance is calculated between each pixel that is set to 0 and the nearest non zero pixel for the binary images. The Euclidean distance which is the straight line distance between two pixels in the image is calculated for watershed transform.

4.2.4 Estimation of terrain derivatives

Topographic information and terrain (DEM) derivatives (slope, aspect, curvature etc.) are used to ideally model the terrain. Craters, being morphological features, can be characterized well using the topography of the terrain and DEM derivatives. Terrain morphometric attributes calculated from the DEM can be used to define the craters. Hence, detecting craters from topographic data is much easier than detecting them from imagery data. Each pixel in a DEM, which is a raster data set $E(x, y)$, is assigned an elevation value $Z(x, y)$. The attributes also can be regarded as raster data set, in which each pixel value (x_0, y_0) is assigned a value calculated from the z values. The value of an attribute at (x_0, y_0) is evaluated using only values of z in the immediate neighbourhood of (x_0, y_0). Slope, aspect and topographic curvature are the examples of such attributes (Bue and Stepinski, 2007).

4.2.4.1 Slope and Aspect

Slope and the aspect are the two first order derivatives of any topographic surface. Slope is defined by a plane tangent to the surface as modelled by the DEM at any given point and comprises two components named as Gradient and Aspect. Gradient is the maximum rate of change of altitude whereas the aspect is the compass direction of this maximum rate of change. Gradient is usually measured in per cent, degrees or radians while aspect is measured in degrees (Evans, 1980).

Aspect identifies the steepest downslope across a surface. It can be thought of as slope direction (compass direction) a hill faces. It is usually measured clockwise in degrees from 0 (due north) to 360. The value of each location in an aspect dataset indicates the direction the surface slope faces. The following steps are followed while computing aspect from DEM data of TMC.

- Read the original DEM.
- Preprocessing of the DEM is done.
- The Sobel edge detector has been used to get all the edges of objects (craters) in the preprocessed DEM.
- Gradient magnitude has been calculated using horizontal edge component (GH) and vertical edge component (GV) obtained using Sobel edge detector. It is the square root of the sum of the squares of GH and GV components as per the equation 4.5. This gradient magnitude is known as the slope of the surface.
- Direction (angle) has been calculated using same GH and GV. It is the inverse tangent angle of the ratio of GV to GH as per the equation 4.6. This calculated direction is known as the aspect of the surface.

$$\text{Slope(gradmag)} = \sqrt{(GH^2 + GV^2)} \qquad (4.5)$$

$$\text{Aspect(direction)} = \tan^{-1}\left(\frac{GV}{GH}\right) \qquad (4.6)$$

Craters can be seen very clearly with the help of the parameters like slope and aspect estimated from DEM data. There is no issue of shadow with these parameters. Hence slope and aspect are very useful in crater detection using DEM.

4.3   Decision

After detecting the craters from image based and DEM based crater detection approaches by implementing various image segmentation techniques, a decision has been taken for choosing a better crater detection technique in each approach. The decision parameters are the edge strength and image detail preserving coefficient which are described below.

4.3.1   Edge Strength

Edge strength tells about the sharpness of the edges of the craters detected using image segmentation techniques. Edge strength is the magnitude of the gradient obtained from the edges present in an image (Gonzalez et al., 2009). The steps implemented in MATLAB for calculating the edge strength are as follows.

- The Sobel edge detector has been used to get all the edges of objects (craters) present in the output images with detected craters using image segmentation techniques.
- Gradient magnitude has been calculated using horizontal edge component (GH) and vertical edge component (GV) obtained using Sobel edge detector. It is the square root of the sum of the squares of GH and GV components as per the equation 4.5. This gives the pixel by pixel edge strength.
- Summation of all the edge pixels of the gradient magnitude image gives the overall edge strength of the detected craters.
- Dividing this overall edge strength by the total number of edge pixels of the gradient magnitude image obtained in step 2 gives the overall edge density (normalized edge strength) of the detected craters.
- The higher the value of edge strength or edge density the better is the sharpness of the edges of the craters.

4.3.2   Image Details Preserving Coefficient (Correlation Coefficient)

The image detail preserving coefficient tells that how much detail of the features present in the input preprocessed image is still there in the output image obtained after applying segmentation techniques. It is the coefficient of correlation between the output image with detected craters and the input preprocessed image (Qiu et al., 2004). Correlation measures the association between two variables and quantitates the strength of their relationship. The coefficient of correlation (r) is calculated between the output image (B) with detected craters using the image segmentation techniques and the input preprocessed image (A), as per the given equation 4.7.

$$r = \frac{\sum_m \sum_n (A_{mn} - \overline{A})(B_{mn} - \overline{B})}{\sqrt{(\sum_m \sum_n (A_{mn} - \overline{A})^2)(\sum_m \sum_n (B_{mn} - \overline{B})^2)}} \qquad (4.7)$$

where $\overline{A}$ and $\overline{B}$ are the mean of image matrices A and B respectively and subscript m and n are the rows and columns of the matrices.

In this research work, image matrix B is considered as the dependent variable while the image matrix A is considered as the independent variable. A significant advantage of the

correlation coefficient (r) is that it does not depend on the units of the variables (A and B) and can therefore be used to compare any two variables regardless of their units. The value of r exists between -1 to +1. Depending on the value of r, the correlation can be classified as negative correlation ($-1 < r < 0$), no correlation ($r = 0$), positive correlation ($0 < r < 1$) and linear correlation($r = 1$). The higher the value of r (highly correlated), the better is the detail preservation in the image. In our study, it is positive and negative correlation only between the output image (B) of all image segmentation techniques and input preprocessed image (A).

4.4   Integration

The integration of one of the image based and DEM based crater detection techniques gives the craters which are finally detected. The integration depends upon the values of the decision parameters evaluated for each segmentation technique. After evaluating the decision parameters for each technique, it is found that aspect which is estimated from the DEM under DEM based crater detection approach and the vertical coefficient of wavelet at level 3 which is the result of multilevel 2-D wavelet decomposition under image based crater detection approach show higher value of edge strength as well as coefficient of correlation among all the techniques. It means the edges are more sharp and the correlation between A and B is more positive in both cases. Hence both the results are integrated to get the final detected craters. The steps implemented in MATLAB for the integration of both these results are as follows.

- The aspect image is converted into binary image.
- The vertical coefficient image at level 3 is converted into binary image.
- If the dimension (size) of both the binary images is not matching with each other, resize them with respect to each other.
- The binary images are then multiplied with each other and finally the output is in the binary format.
- Visualize the result as image having final craters detected using the integrated approach.

4.5   Crater Attributes Measurement using Moment Measure Technique

Crater attributes (shape, size) have been measured using moment measure technique. Moment measure technique is a regional based descriptor which involves two steps:

- Region of interest identification in the image and differentiating them into individual components.
- Determining the attributes for the components using regional descriptors.

Gonzalez and Wintz (1977) stated that for the two dimensional continuous function $f(x, y)$ the moment of order $(p + q)$ is represented as per the equation 4.8.

$$m_{pq} = \int_{-\infty}^{\infty} \int_{-\infty}^{\infty} x^p y^q f(x, y) dx dy \qquad (4.8)$$

For p, q = 0, 1, 2…

$$f(x, y) = 1 \qquad \text{(Object or target; region of interest)}$$
$$f(x, y) = 0 \qquad \text{(Background; outside region of interest)}$$

The two first order moments representing the centre of mass of the image f (x, y) are represented as per the equations 4.9 and 4.10 respectively.

$$m_{10} = \int_{-\infty}^{\infty} \int_{-\infty}^{\infty} x f(x, y) dx dy \tag{4.9}$$

$$m_{01} = \int_{-\infty}^{\infty} \int_{-\infty}^{\infty} y f(x, y) dx dy \tag{4.10}$$

The centre of mass is the point in an image where the mass of the image can be concentrated without changing the first moment of any given axis. The centre of mass is used to represent the location of the image in the field of view (equation 4.9, 4.10) can be used as a reference point to locate the location of the image. Lai et al (2008) stated that the centroid of an image or the centre of gravity is the balancing point of the image function f (x, y) and m_{00} is the zero order moment, m_{10} is the first order row moment and m_{01} is the first order column moment.

Central moments and normalized central moments are derived from the objects from which length of the major and minor axes and orientation of the objects are determined. Zhou et al. (2009) defined central moment as certain particular weighted average of the image pixel's intensities and are useful for interpreting an object after segmentation because of their relation to object shape where the object (region of interest) is found based on image moments, like area, centroid and orientation.

4.5.1   Moment Measures

A MATLAB program is written for crater attribute measurement using inbuilt 'regionprops' function. It measures properties of image regions based on moment measures. The output is a structure array with length equal to the number of objects in binary image. It measures a set of properties for each connected component (object) in the binary image. The fields of the structure array denote different properties for each region. The 'properties' can be a comma-separated list of strings, a cell array containing strings, the single string 'all', or the string 'basic'. If 'properties' is the string 'all', regionprops computes the parameters for the shape measurements like 'Area', 'Orientation', 'Extent', 'Perimeter', 'Centroid', 'Eccentricity', 'MajorAxisLength', 'EquivDiameter', 'MinorAxisLengt'. If 'regionprops' is applied on a grayscale image, it also returns the parameters like 'MaxIntensity', 'MinIntensity', 'WeightedCentroid', 'MeanIntensity', 'PixelValues' for pixel value measurements. If 'properties' is not specified or if it is the string 'basic', regionprops computes only the 'Area', 'Centroid', and 'BoundingBox' measurements.

In the current methodology, we have applied 'regionprops' function on a structure of connected components of the binary image with final detected craters. The structure of the connected components is obtained using 'bwconncomp' which is inbuilt function in MATLAB and it returns the connected components (CC) found in the binary image. The binary image can have any dimension. CC is a structure with four fields which are Connectivity (Connectivity of the connected components (objects)), ImageSize (Size of the binary image), NumObjects (Number of connected components in binary image) and PixelIdxList. 'bwconncomp' uses a default connectivity of 8 for two dimensions, 26 for

three dimensions. In this methodology, we have used the default connectivity. The steps implemented in MATLAB to get the shape measurement parameters from the binary image are as follows.

- Reading the binary image.
- Getting the structure of connected components (CC) present in the binary image using 'bwconncomp' function in MATLAB.
- Applying 'regionprops' on the structure of connected components (CC) which returns a structure array with length equal to the number of objects in binary image.
- The function 'regionprops' returns the shape measurement parameters for the connected components. These parameters are centroid, area, diameter, eccentricity, extent, orientation, minor axis length, major axis length, and perimeter. All these parameters are supported for 2-D input label matrix which is used to visualize connected components (CC).
- The inbuilt function 'labelmatrix' is used to create a label matrix from the output (CC) of 'bwconncomp'. The function 'labelmatrix' stores the label matrix in the smallest numeric class necessary for the number of objects.

The shape measurement parameters are described one by one below.

Centroid: It is a vector that specifies the centre of mass of the region. The first element of centroid is the horizontal coordinate (x-coordinate) of the centre of mass and the second element is the vertical coordinate (y-coordinate). All other elements of centroid are in order of dimension.

Area: It is a scalar quantity representing the actual number of pixels in the region.

Diameter: It is a scalar that specifies the diameter of a circle with the same area as the region. It is the square root of the ratio of four times the value of area obtained to the value of pi as per the equation 4.11.

$$\text{Diameter} = \sqrt{\frac{(4*\text{Area})}{\text{pi}}} \qquad\qquad (4.11)$$

Eccentricity: It is a scalar that specifies the eccentricity of the ellipse that has the same second-moments as the region. The eccentricity is the ratio of the distance between the foci of the ellipse to the major axis length as per the equation 4.12. The value of eccentricity is between 0 and 1. An ellipse whose eccentricity is exactly 0 is actually a circle, while an ellipse whose eccentricity is 1 is ellipse only.

$$\text{Eccentricity}, e = \frac{\text{Focal distance}}{\text{Major axis length}} \qquad\qquad (4.12)$$

Extent: It is a scalar that specifies the ratio of pixels in the region to pixels in the total bounding box. Bounding Box is the smallest rectangle containing the region. Extent is computed as the area divided by the area of the bounding box.

Orientation: It is a scalar specifying the angle (in degrees ranging from -90 to 90 degrees) between the x-axis and the major axis of the ellipse that has the same second-moments as the region.

Minor Axis Length: It is a scalar specifying the length (in pixels) of the minor axis of the ellipse that has the same normalized second central moments as the region.

Major Axis Length: It is scalar specifying the length (in pixels) of the major axis of the ellipse that has the same normalized second central moments as the region.

Perimeter: It is scalar specifying the distance around the boundary of the region. The function 'regionprops' computes the perimeter by calculating the distance between each adjoining pair of pixels around the border of the region.

The parameters like diameter and area of the detected craters are used to determine the crater size frequency distribution (CSFD) which tells the age of the craters and hence about the evolution of the lunar surface.

4.6   Surface Age Dating

Counting (frequency) of impact craters is a simple method which is often used to estimate the ages of geologic units (craters) on the planetary surfaces when in situ rock samples are not available (Le Feuvre and Wieczorek, 2011). It is possible to determine the ages of planetary surface units by measuring the crater frequencies using remotely sensed image data (Morota et al., 2008). Crater size frequency distributions (CSFDs) have been used to get absolute ages with the help of remotely sensed image data (Kneissl et al., 2011). In this work, crater size frequency distribution (CSFD) of impact craters has been used for age determination of lunar surface using TMC data (equatorial region of moon) and MiniSAR data (North Pole and South Pole of moon). Some basic assumptions given by Michael and Neukum (2010) have been taken in this research for crater chronology of lunar surface. These are given below.
- The particle flux is constant over the entire surface of moon.
- The frequency of the impact craters can be measured with respect to the size of the craters.
- The area of interest to be dated is a homogenous unit.

The concept of the age determination involves fitting the observed crater size frequency distribution (CSFD) of a given surface unit to a known crater production function (PF) and to use the crater frequency for certain crater sizes together with a calibrating chronology function (CF) to get absolute age. Therefore, to measure the age of the lunar surface unit, cumulative crater size frequency distribution normalized to a unit area is plotted and the production function is shifted until it fits the data points. Hence it is possible to read the cumulative frequency at standard crater diameter (Michael and Neukum, 2010).
The steps adopted for crater chronology of lunar surface are described here one by one.

- **Crater Size Frequency Distribution (CSFD):** It computes the number of craters per unit area as a function of crater size. The size of the crater (diameter) and the frequency of the crater distribution (number of craters per unit area) are the two basic parameters that control the crater density of a particular surface. Crater size frequency distribution (CSFD) is computed semi automatically in GIS environment using 'CraterTools' and automatically using shape descriptor technique (based on moment measures) which has been implemented in MATLAB. 'CraterTools' which is a software extension in ArcMap (ArcGIS) toolbar has been used for measuring CSFDs on lunar surface. The measured CSFD is independent of map projection and image data. The workflow of the 'CraterTools' software is divided into two processes. The first process is the determination of correct sizes of the impact craters present in the homogeneously cratered areas. The second process comprises of digitization of the impact craters in the same homogeneous area and determination of their correct size in the form of diameters. 'CraterTools' computes size frequency distribution by generating two empty shape files with attributes that are later used for calculation of the crater age. The first polygon shape file is for storing one or several measurement areas and second shape file is for storing impact craters. The shape file for the impact craters is drawn by three point's tool which digitises the craters using three points on the crater rim from which a circle is drawn. The two polygon shape files act as input for generation of CSFD age determination (Kneissl et al., 2011). Finally the 'CraterTools' gives the size (diameter) of craters which is stored as '*.diam' text file.

- **Production Function:** It describes formation of number of craters of a particular size in relation to the number of craters of any other size. In this work, Neukum Production Function (NPF) is used which is 11th order polynomial fit to the cumulative number of craters, N per square kilometer with diameters larger than a particular diameter D. For the time period of 1Ga, N (D) may be expressed as per the equation 4.13 given below.

$$\log_{10}(N) = a_0 + \sum_{n=1}^{11} a_n [\log_{10}(D)]^n \tag{4.13}$$

Here, D is in km and N is the number of craters with diameters > D per km^2 per Ga. This equation is valid for D = 0.01 km to 300 km.

- **Chronology Function:** After plotting of the production function with respect to the diameter of the craters, the production function is derived from the SFD plot and that value is substituted in the equation 4.14 to calculate the age of the lunar surface.

$$N_{cum}(D > 1\ km) = 5.44 * 10^{-14}[\exp(6.93 * t) - 1] + 8.38 * 10^{-4} * t \tag{4.14}$$

Here, N is the cumulative crater frequency per km^2 for D > 1 km and t is the crater accumulation time (Ga).

In this research work, 'Craterstats' tool, an extension in ENVI is used to get the lunar surface ages. The CSFD based diameter files, generated by 'CraterTools' software in

ArcGIS, are fed to the 'Craterstats' tool along with the lunar production function. The imported data are binned and the craters are counted. The lunar production function is fitted to the CSFD of the detected craters. The production function is shifted until it fits the data points and finally we get the age of lunar surface. The age is displayed as isochron and the image is exported into '*.png' file format and the composite files are saved (Michael and Neukum, 2010).

4.7   Softwares /Tools Used

MATLAB 12
ArcGIS 10
ENVI 5

Automatic crater detection algorithms for all the image segmentation techniques used in the methodology of this research work have been developed and implemented in MATLAB 2012 software. The decision parameters also have been computed in MATLAB 2012 software only. The integration of image based and DEM based crater detection approaches have been done in MATLAB 2012 software.

ArcGIS 10 software has been used as a support (platform) to Crater Tools which is a set of tools to measure crater size-frequency distribution (CSFD) for lunar surface.

ENVI 5 software has been used as a support (platform) to Craterstats software tool which has been used for getting production function and crater chronology (age) function for lunar surface.

5 Results and Discussion

5.1 Pre-processing

5.1.1 Noise Filter

(a)

(b)

(c)

(d)
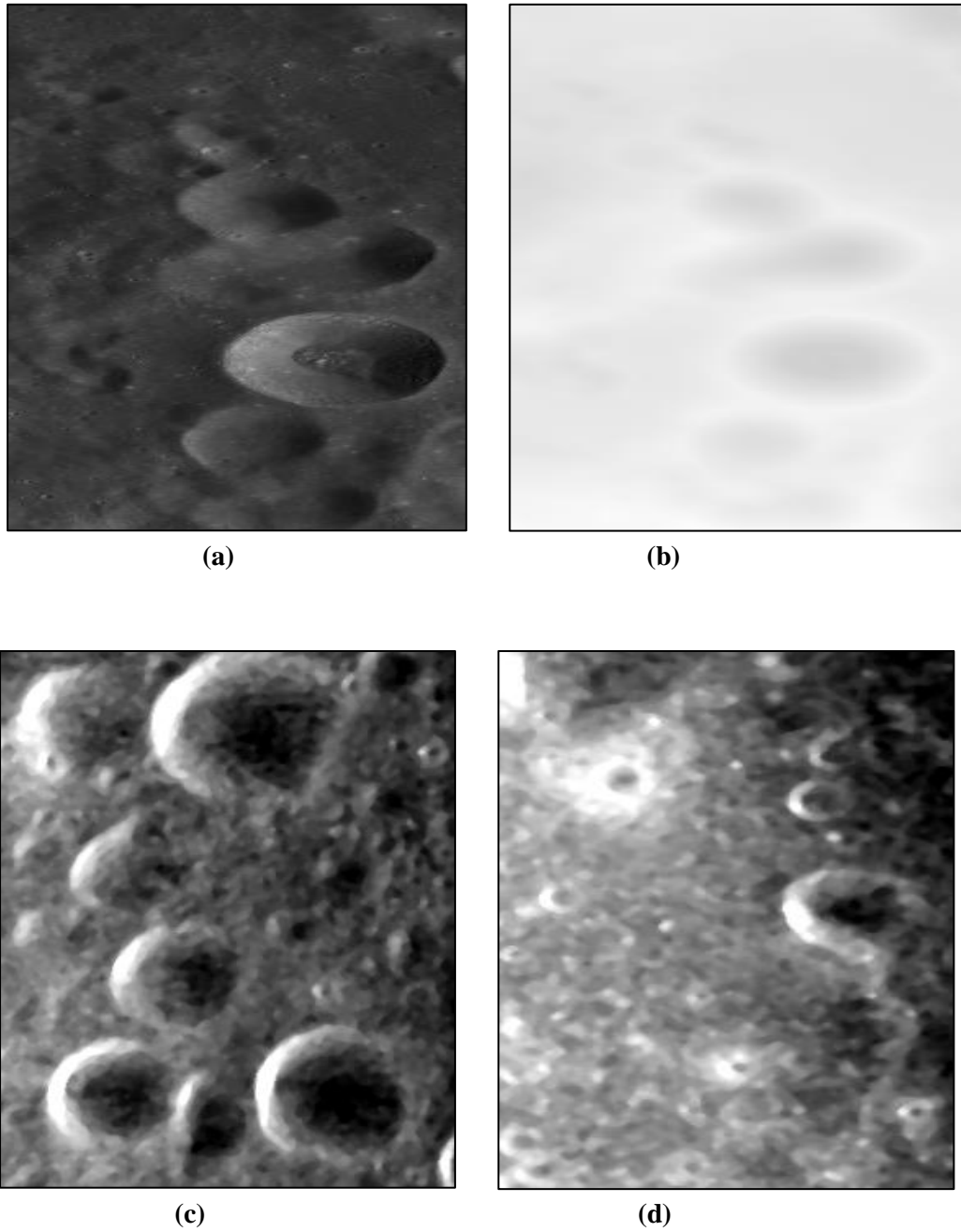
Figure 5.1 Results of noise filter

The noise present in the original images and DEM has been removed using median filter. The same median filter has been applied on all the images as well as on DEM. Figure 5.1 shows the results obtained after removing the noise. Figure 5.1(a), (b), (c) and (d) shows the results of noise filter applied on TMC image, shown in Figure 3.1(a), TMC DEM, shown in Figure 3.1 (b), North Pole MiniSAR image and South Pole MiniSAR image, shown in Figure 3.2, respectively.

5.1.2   Area Filter

(a)   (b)

(c)   (d)
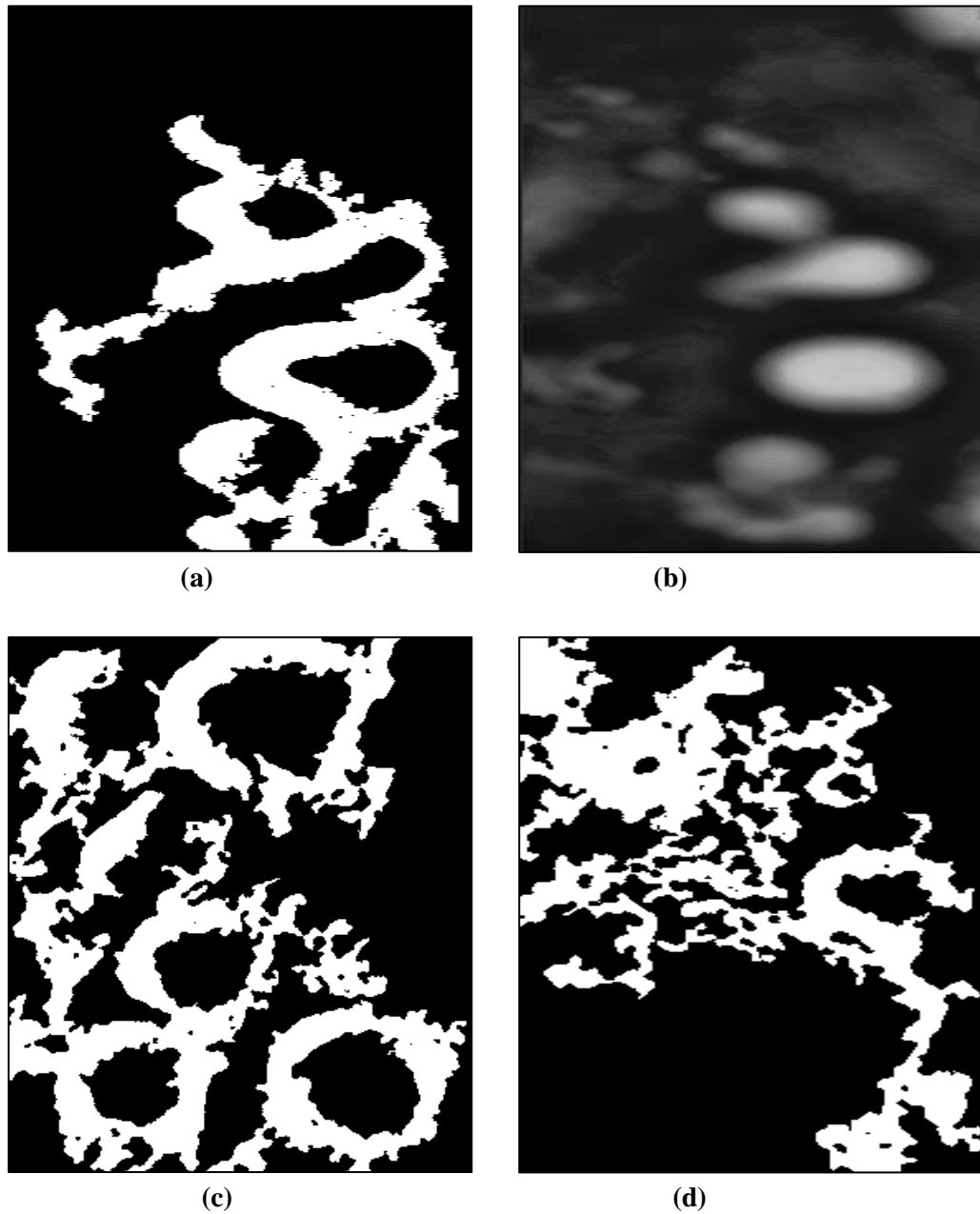
Figure 5.2 Results of area filter

Figure 5.2 (a), (b), (c), (d) shows the area filtered TMC image, TMC DEM North Pole MiniSAR image, South Pole MiniSAR image respectively. In these figures the background features such as mountains (non-crater features) that are too large not to be part of the craters have been removed by applying area filter on the median filtered images and DEM. The output (result) of Area filter is in the binary format.

5.1.3 Shape Filter

(a)

(b)

(c)

(d)
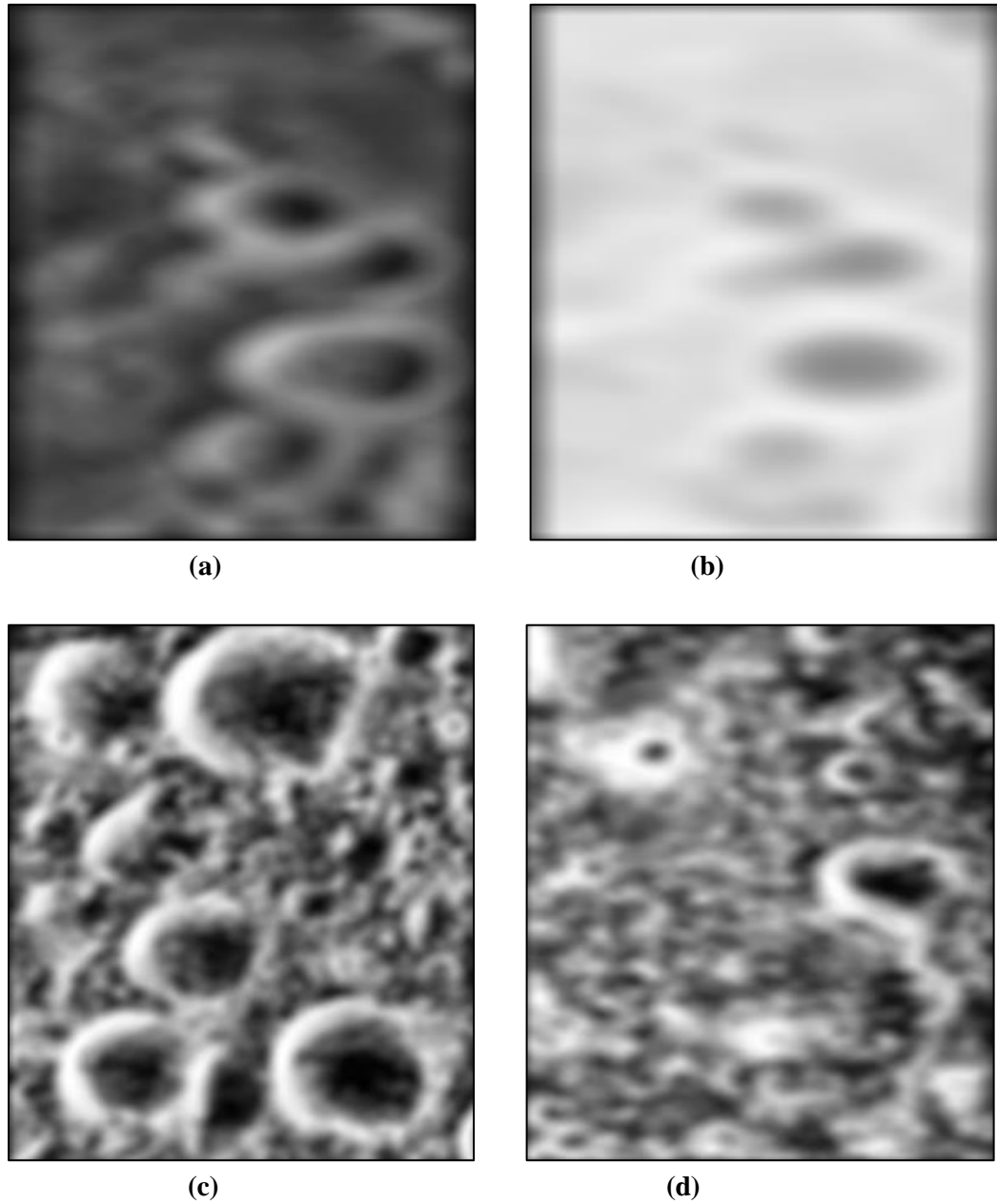
Figure 5.3 Results of shape filter

Figure 5.3 (a), (b), (c), (d) shows the shape filtered TMC image, TMC DEM, North Pole MiniSAR image, South Pole MiniSAR image respectively. These results show the features

having shapes comparable to the shape of craters. Only circular and elliptical shapes are preserved and other shapes have been removed using shape filter applied on the area filtered images and DEM.

5.2 Crater Detection Techniques

5.2.1 Wavelet Transform

- **Decomposition of TMC image at scale (level) 1:**

(a)

(b)

(c)

(d)
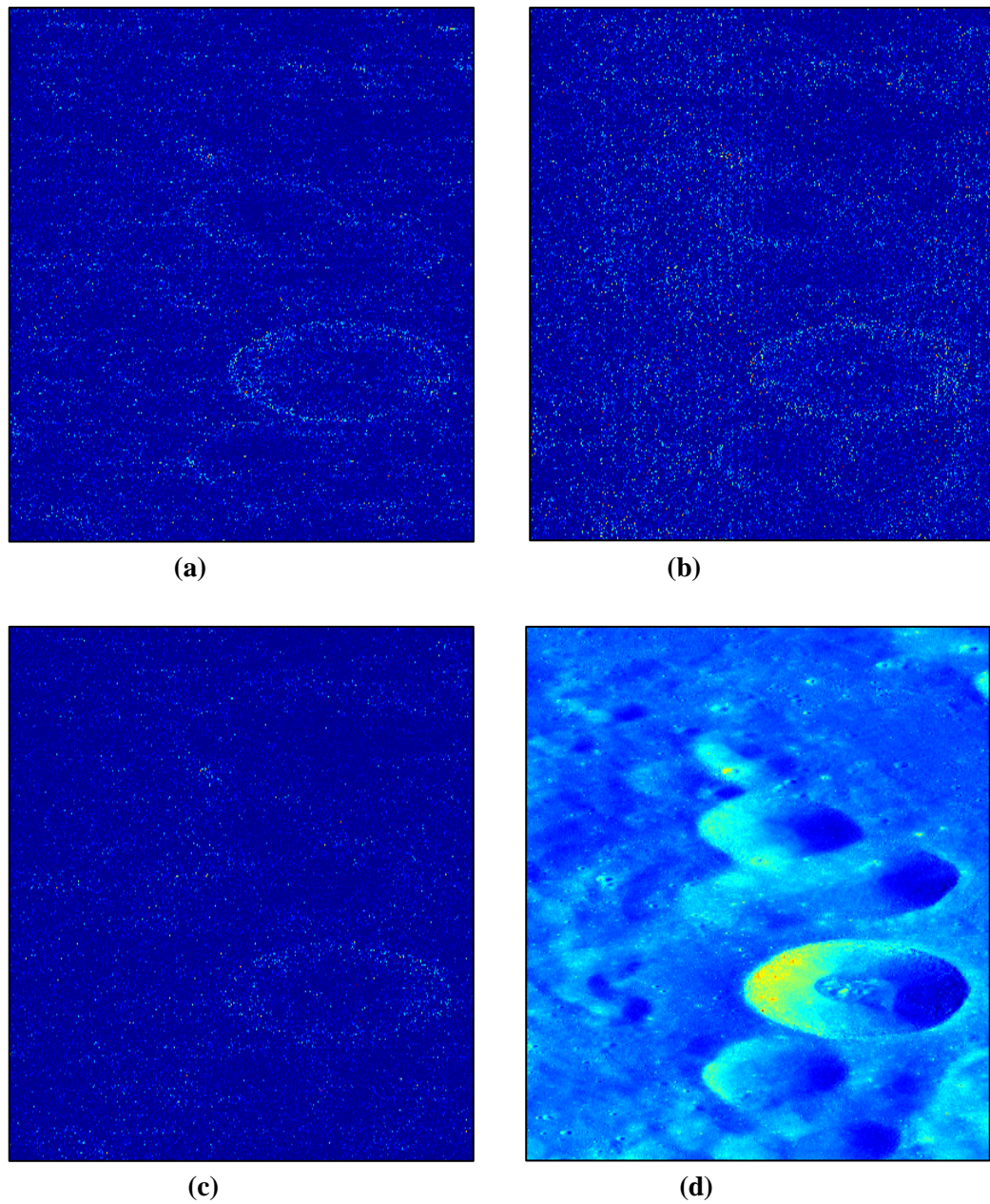
Figure 5.4 Results of Wavelet decomposition at scale 1 on TMC image

The above results show the detected edges using Haar wavelet decomposition of the TMC image at scale 1. Figure 5.4 (a) shows the horizontal coefficient obtained after wavelet decomposition at scale 1. The horizontal coefficient gives edge details in horizontal direction. Figure 5.4 (b) shows the vertical coefficient obtained after wavelet decomposition at scale 1. The vertical coefficient gives edge details in vertical direction. Figure 5.4 (c) shows the diagonal coefficient obtained after wavelet decomposition at scale 1. The diagonal coefficient gives diagonal edge details. Among all the three coefficients, vertical coefficient gives most clear and sharp edges. Figure 5.4 (d) shows the image reconstructed from the decomposition structure (matrix) at scale 1. The decomposition at scale 1 is not detecting all the edges of craters in the image and even the detected edges (boundaries) of craters are not very clear and sharp.

- **Decomposition of TMC image at scale (level) 2:**

(a)

(b)

(c)

(d)

Figure 5.5 Results of Wavelet decomposition at scale 2 on TMC image

The above results show the detected edges using Haar wavelet decomposition of the TMC image at scale 2. Figure 5.5 (a) shows the horizontal coefficient obtained after wavelet decomposition at scale 2. Figure 5.5 (b) shows the vertical coefficient obtained after wavelet decomposition at scale 2. Figure 5.5 (c) shows the diagonal coefficient obtained after wavelet decomposition at scale 2. Among all the three coefficients, vertical coefficient gives most clear and sharp edges. Figure 5.5 (d) shows the image reconstructed from the decomposition structure (matrix) at scale 2. The decomposition at scale 2 gave better results of crater detection than the decomposition at scale 1.

- **Decomposition of TMC image at scale (level) 3:**

(a)

(b)

(c)

(d)

Figure 5.6 Results of Wavelet decomposition at scale 3 on TMC image

The above results show the detected edges using Haar wavelet decomposition of the TMC image at scale 3. Figure 5.6 (a) shows the horizontal coefficient obtained after wavelet decomposition at scale 3. Figure 5.6 (b) shows the vertical coefficient obtained after wavelet decomposition at scale 3. Figure 5.6 (c) shows the diagonal coefficient obtained after wavelet decomposition at scale 3. Among all the three coefficients, vertical coefficient gives most clear and sharp edges. Figure 5.6 (d) shows the image reconstructed from the decomposition structure (matrix) at scale 3. The decomposition at scale 3 gave better results of crater detection than the decomposition at scale 1 and scale 2.

- **Decomposition of TMC image at scale (level) 4:**
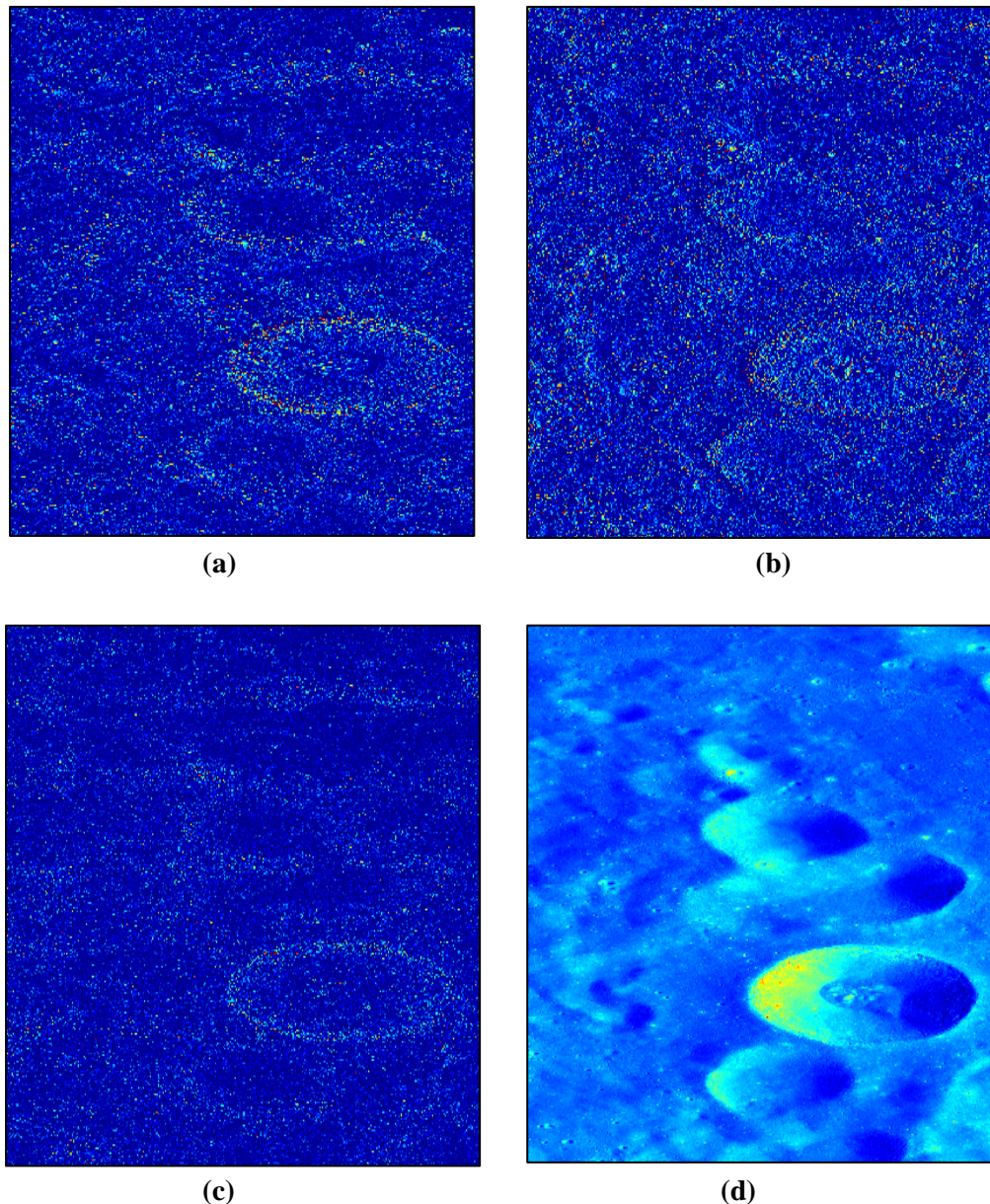

(a)

(b)

(c)

(d)

Figure 5.7 Results of Wavelet decomposition at scale 4 on TMC image

The above results show the detected edges using Haar wavelet decomposition of the TMC image at scale 4. Figure 5.7 (a) shows the horizontal coefficient obtained after wavelet decomposition at scale 4. Figure 5.7 (b) shows the vertical coefficient obtained after wavelet decomposition at scale 4. Figure 5.7 (c) shows the diagonal coefficient obtained after wavelet decomposition at scale 4. Among all the three coefficients, vertical coefficient gives most clear and sharp edges. Figure 5.7 (d) shows the image reconstructed from the decomposition structure (matrix) at scale 4. The decomposition at scale 4 gave very coarse details of edges at pixel level. At this scale of decomposition, shape of craters got destroyed. Hence the craters are not detectable at scale 4.
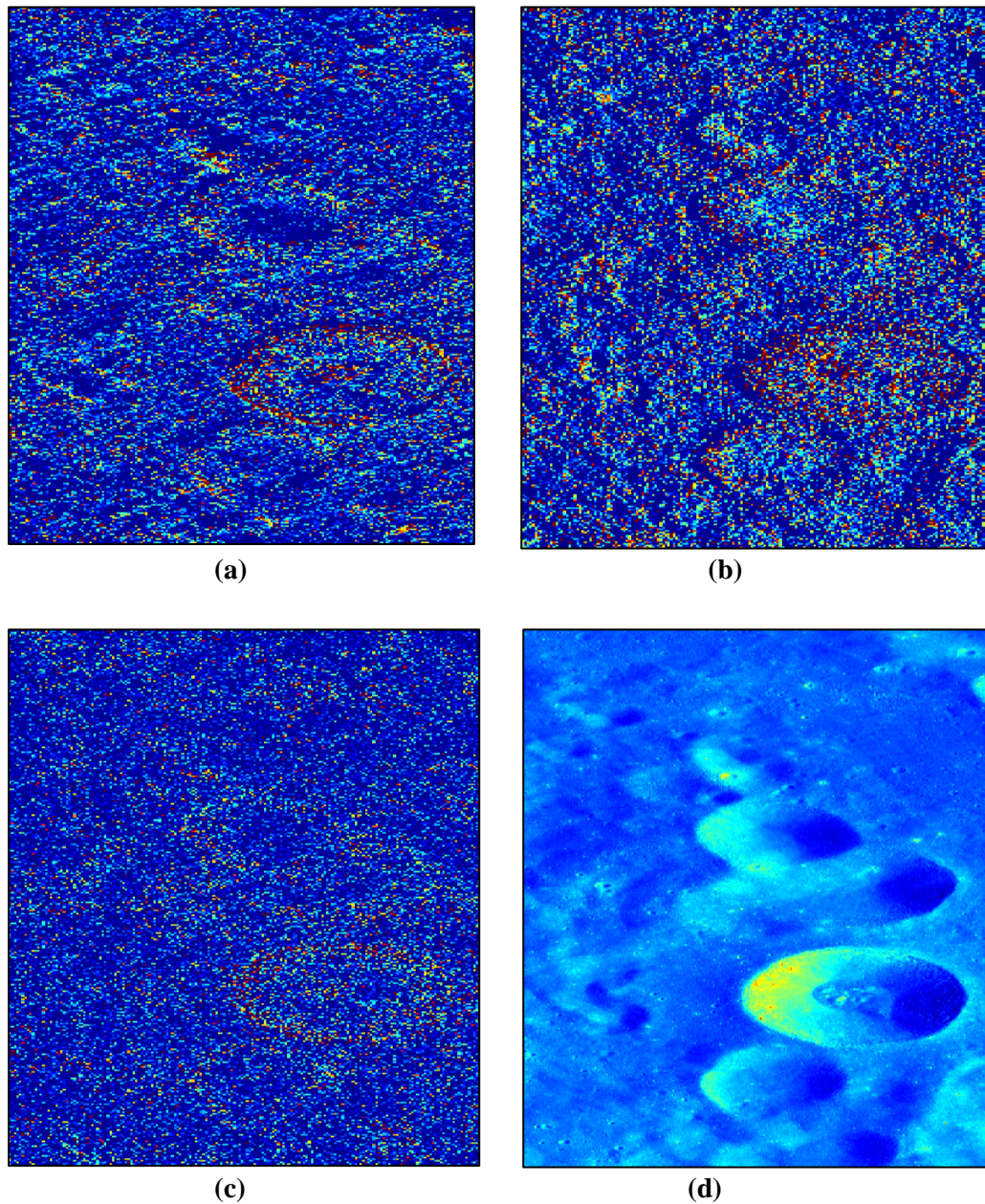
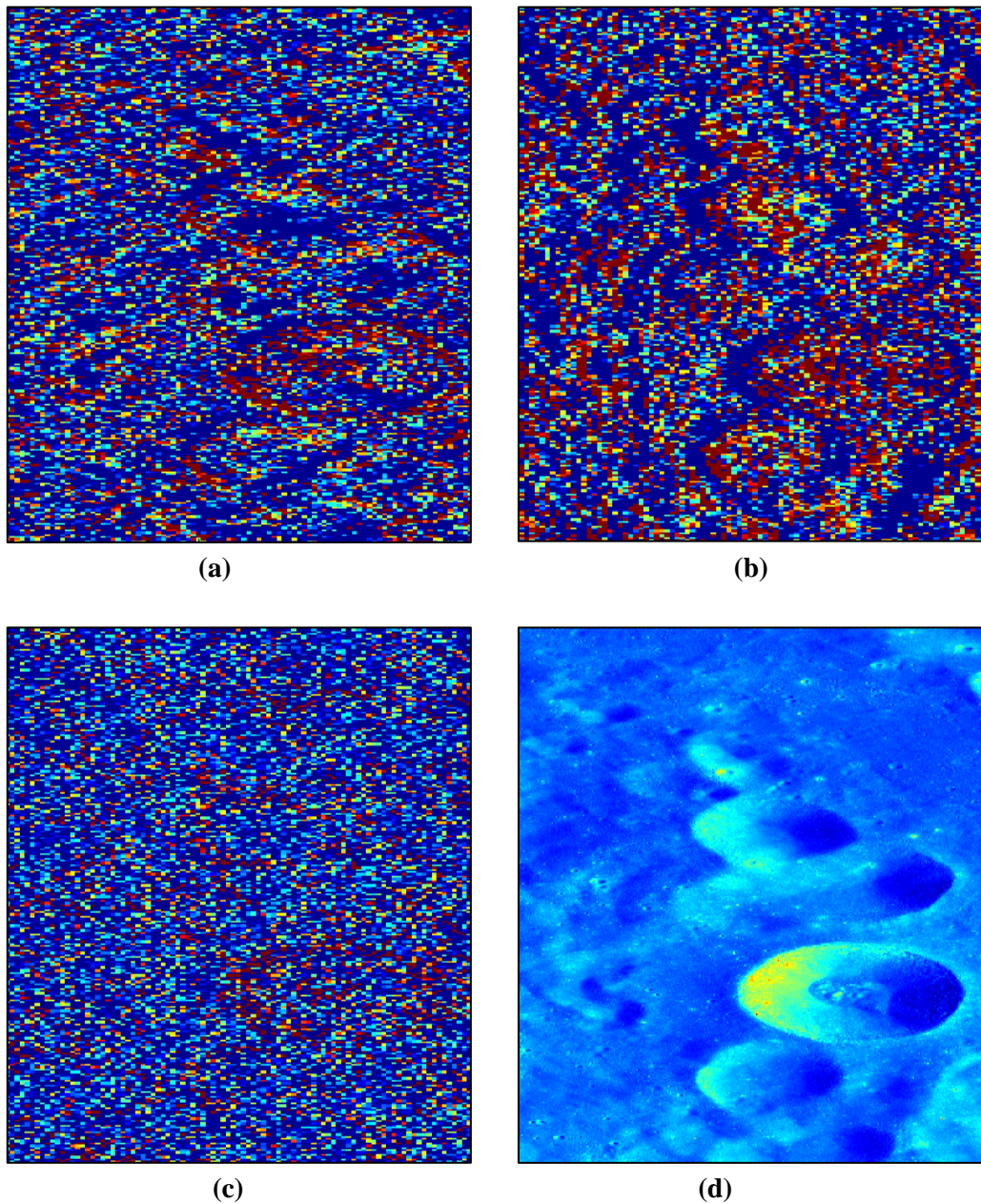- **Decomposition of TMC image at scale (level) 5:**

(a)

(b)

(c)

(d)
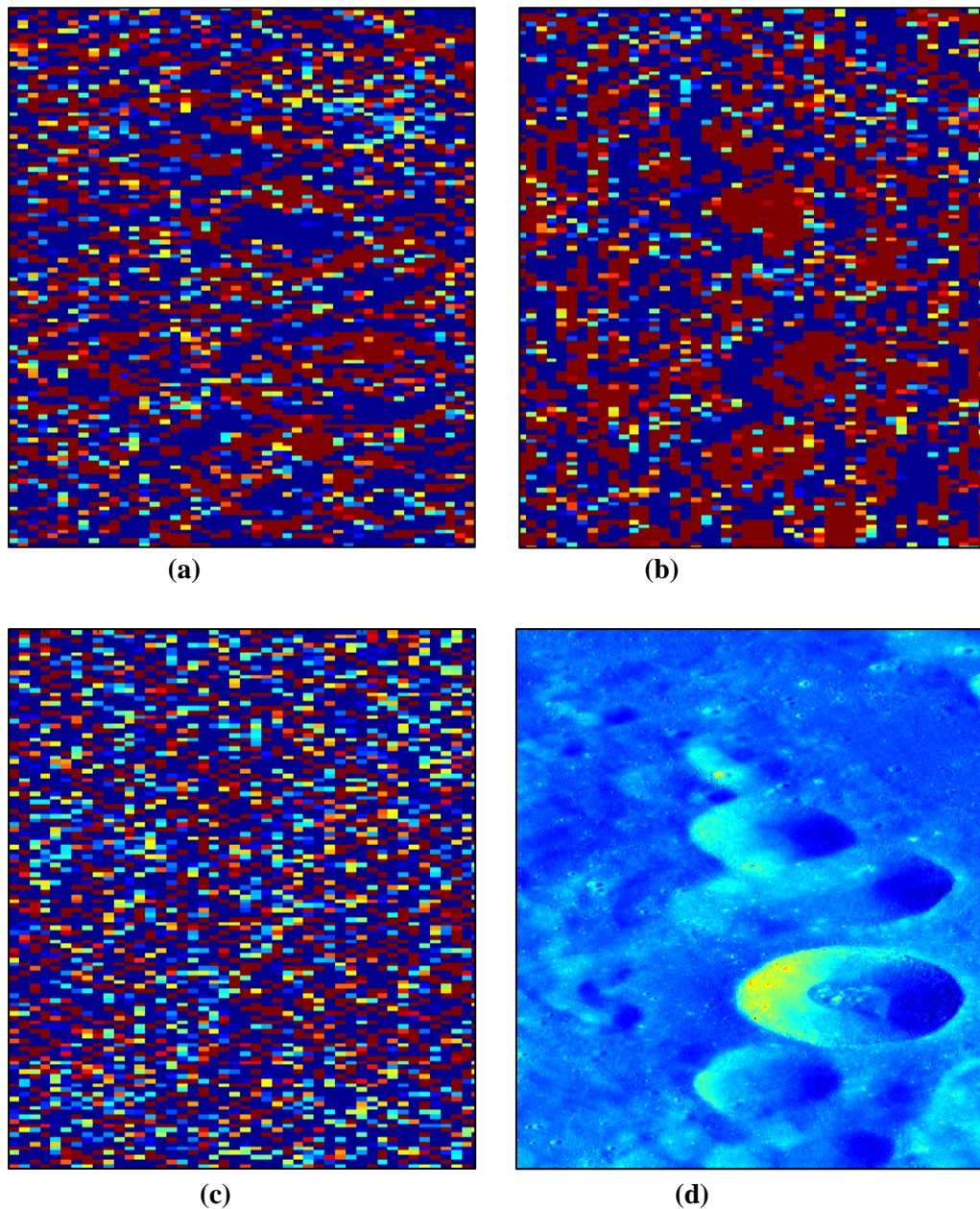
Figure 5.8 Results of Wavelet decomposition at scale 5 on TMC image

The above results show the detected edges using Haar wavelet decomposition of the TMC image at scale 5. Figure 5.8 (a) shows the horizontal coefficient obtained after wavelet decomposition at scale 5. Figure 5.8 (b) shows the vertical coefficient obtained after wavelet decomposition at scale 5. Figure 5.8 (c) shows the diagonal coefficient obtained after wavelet decomposition at scale 5. Among all the three coefficients, vertical coefficient gives most clear and sharp edges. Figure 5.8 (d) shows the image reconstructed from the decomposition structure (matrix) at scale 5. The edge details at scale 5 are coarser than the edge details at scale 4.

Larger is the scale, the details are coarser. As the scale of decomposition increases, shape of craters is also getting destroyed. Hence the craters in the TMC image are not detectable at scale larger than 3. Craters are best detected at scale 3 with their preserved shapes in the TMC image.

- **Continuous Wavelet Transform (CWT) of TMC image:**

(a)   **(b)**

(c)
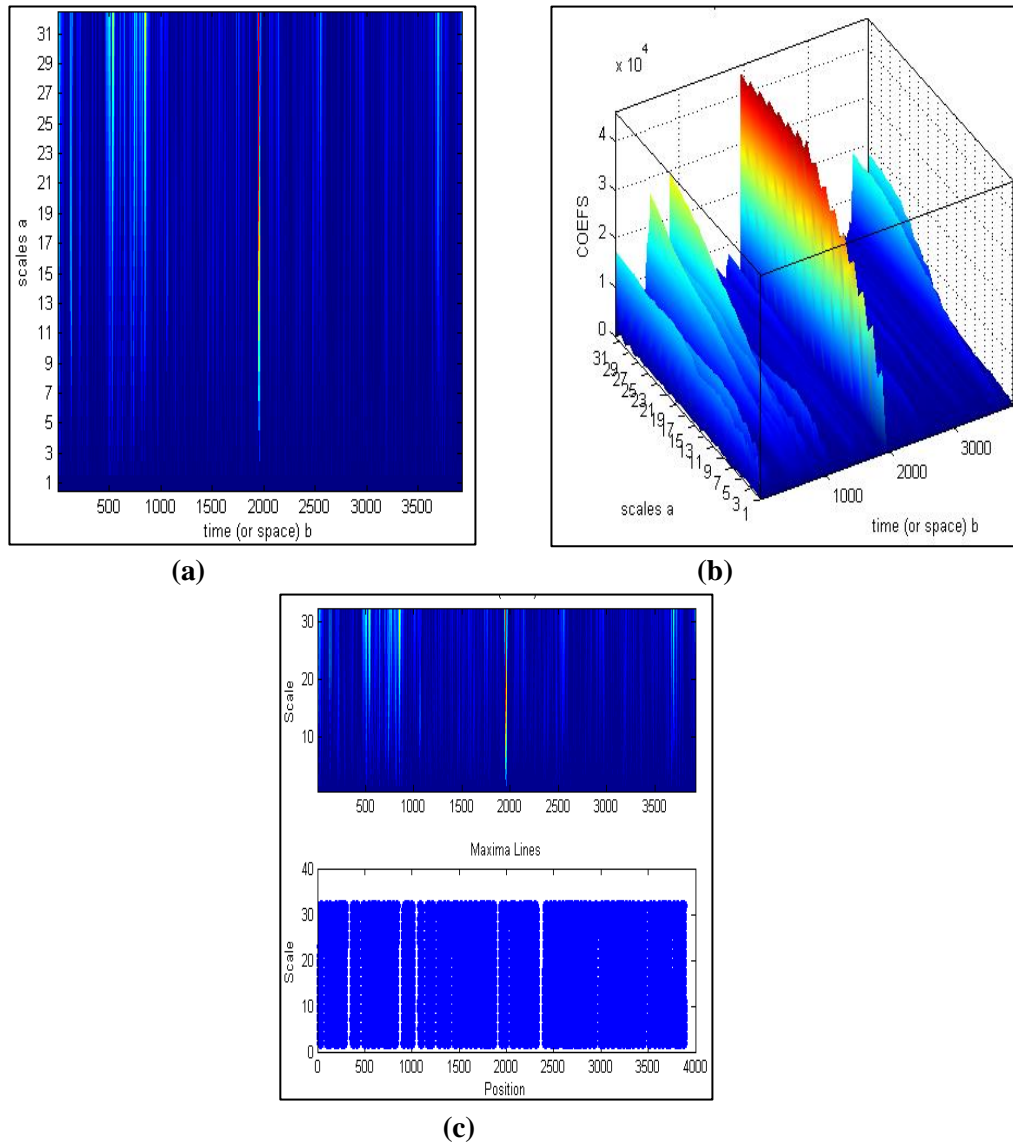
Figure 5.9 Results of Continuous Wavelet Transform on TMC image

The continuous wavelet coefficients have been visualized as 3D plot and surface plot. At lower value of s the image is compressed and high frequency (fine) details of the features (craters) are achieved. At higher value of s the image gets stretched and low frequency (coarse) details of the features are achieved. Figure 5.9 (a) shows the abrupt changes occurred in the TMC image in time-scale domain. These changes are due to the edges of craters. CWT finds the position of these changes with respect to scale varying from 1 to 32. Figure 5.9 (b) shows the 3-D plot of CWT, applied on the TMC image, with third variable as CWT coefficients. Figure 5.9 (c) shows the position of lines of maxima with respect to the scale for TMC image. The lines of maxima are calculated from the moduli of CWT coefficients.

- **Decomposition of North Pole MiniSAR image at scale (level) 1:**

(a)

(b)

(c)

(d)
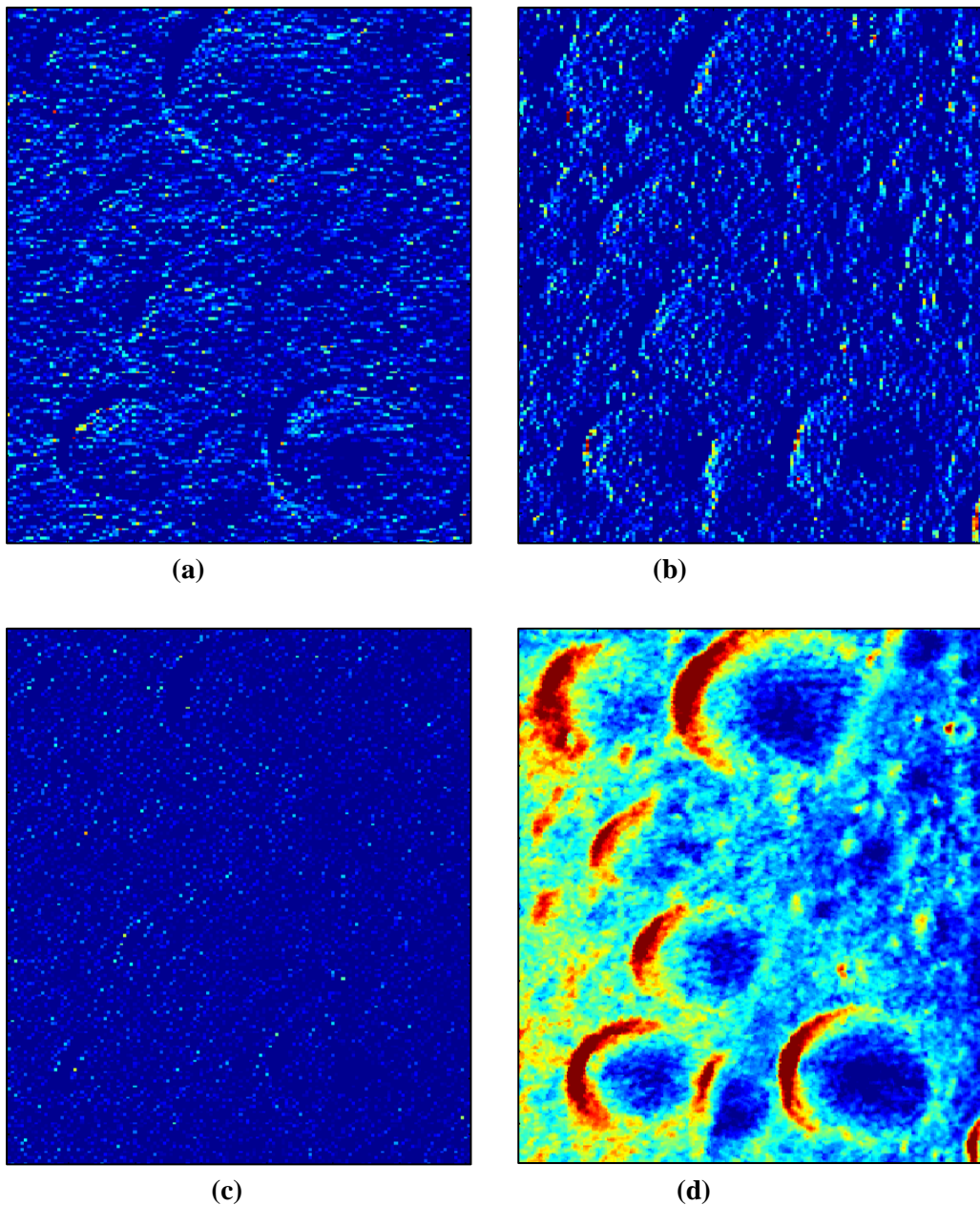
Figure 5.10 Results of Wavelet decomposition at scale 1 on North Pole MiniSAR image

The above results show the detected edges using Haar wavelet decomposition of the North Pole MiniSAR image at scale 1. Figure 5.10 (a) shows the horizontal coefficient obtained after wavelet decomposition at scale 1. The horizontal coefficient gives edge details in horizontal direction. Figure 5.10 (b) shows the vertical coefficient obtained after wavelet decomposition at scale 1. The vertical coefficient gives edge details in vertical direction. Figure 5.10 (c) shows the diagonal coefficient obtained after wavelet decomposition at scale 1. The diagonal coefficient gives diagonal edge details. Among all the three coefficients, vertical coefficient gives most clear and sharp edges. Figure 5.10 (d) shows the image reconstructed from the decomposition structure (matrix) at scale 1. The decomposition at scale 1 is giving the edge details at pixel level of the image and the shape of craters is also preserved.

- **Decomposition of North Pole MiniSAR image at scale (level) 2:**


(a)

(b)

(c)

(d)

Figure 5.11 Results of Wavelet decomposition at scale 2 on North Pole MiniSAR image

The above results show the detected edges using Haar wavelet decomposition of the North Pole MiniSAR image at scale 2. Figure 5.11 (a) shows the horizontal coefficient obtained after wavelet decomposition at scale 2. Figure 5.11 (b) shows the vertical coefficient obtained after wavelet decomposition at scale 2. Figure 5.11 (c) shows the diagonal coefficient obtained after wavelet decomposition at scale 2. Among all the three coefficients, vertical coefficient gives most clear and sharp edges. The coefficients obtained at scale 2 give lesser details than the coefficients at scale 1. Figure 5.11 (d) shows the image reconstructed from the decomposition structure (matrix) at scale 2. The decomposition at scale 2 does not give fine edge details at pixel level and at this scale of decomposition, shape of craters got destroyed. Hence the craters are not detectable at scale 2.

- **Decomposition of North Pole MiniSAR image at scale (level) 3:**
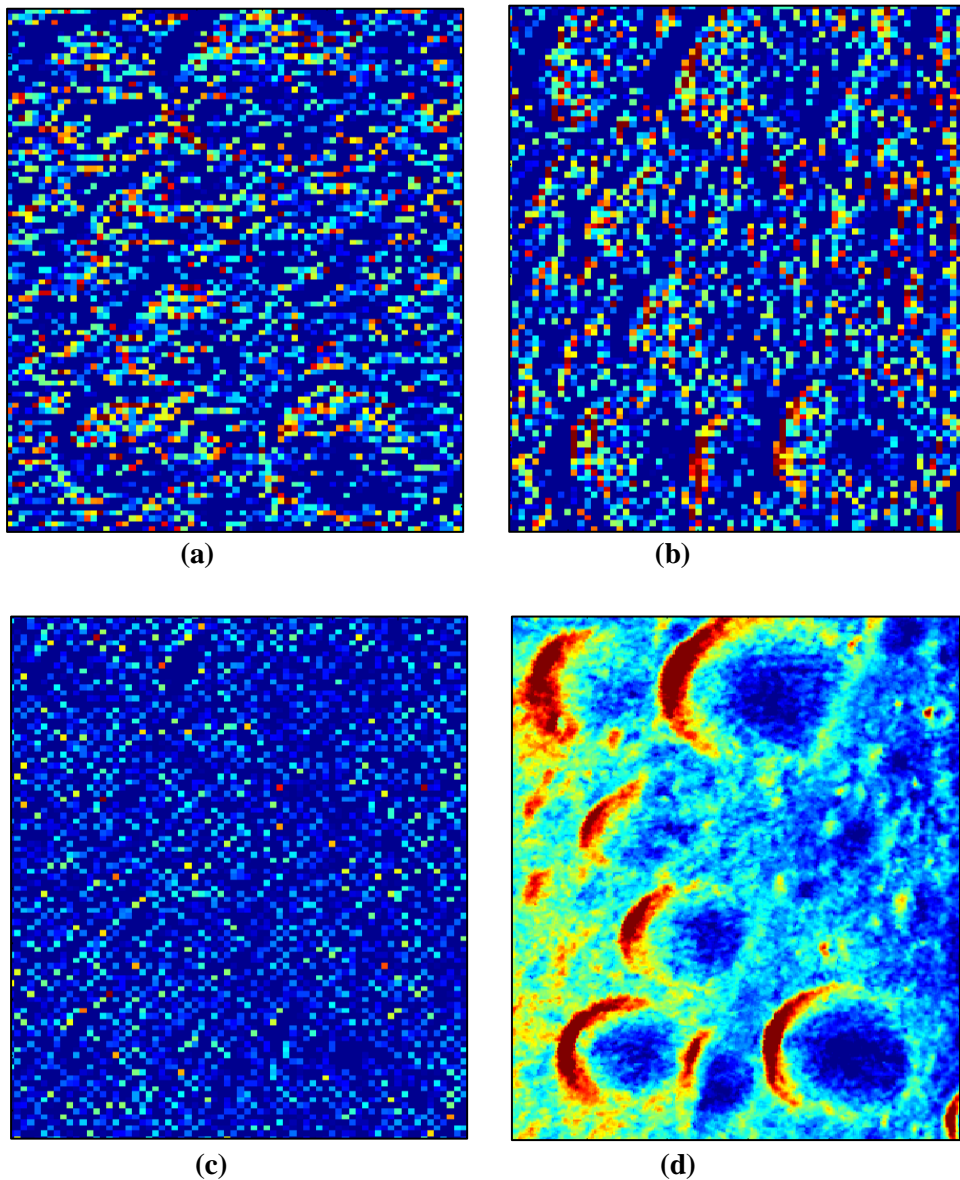

(a)

(b)

(c)

(d)
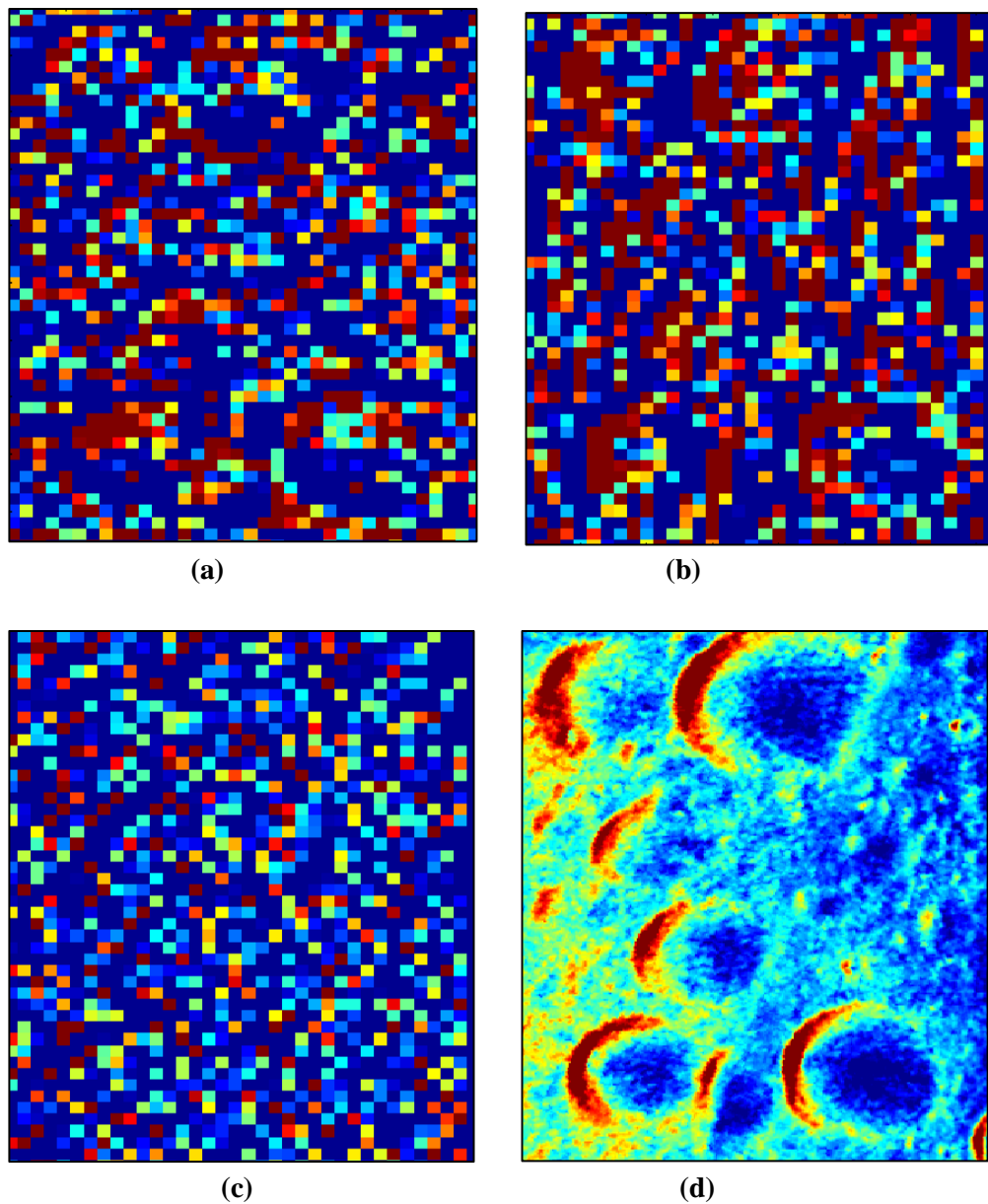
Figure 5.12 Results of Wavelet decomposition at scale 3 on North Pole MiniSAR image

The above results show the detected edges using Haar wavelet decomposition of the North Pole MiniSAR image at scale 3. Figure 5.12 (a) shows the horizontal coefficient obtained after wavelet decomposition at scale 3. Figure 5.12 (b) shows the vertical coefficient obtained after wavelet decomposition at scale 3. Figure 5.12 (c) shows the diagonal coefficient obtained after wavelet decomposition at scale 3. The coefficients obtained at scale 3 give lesser details than the coefficients at scale 1 and scale 2. Figure 5.12 (d) shows the image reconstructed from the decomposition structure (matrix) at scale 2. The decomposition at scale 3 gives lesser edge details at pixel level and at this scale of decomposition, shape of craters got more destroyed. Hence the craters are not detectable at scale 3.

As the scale of decomposition increases, edge details are less and the shape of craters is also getting destroyed. Hence the craters in the North Pole MiniSAR image are not detectable at scale larger than 1. Craters of North Pole MiniSAR image are best detected at level 1 with the preservation of their shapes.

- **Continuous Wavelet Transform (CWT) of North Pole MiniSAR image:**

(a)   (b)

(c)
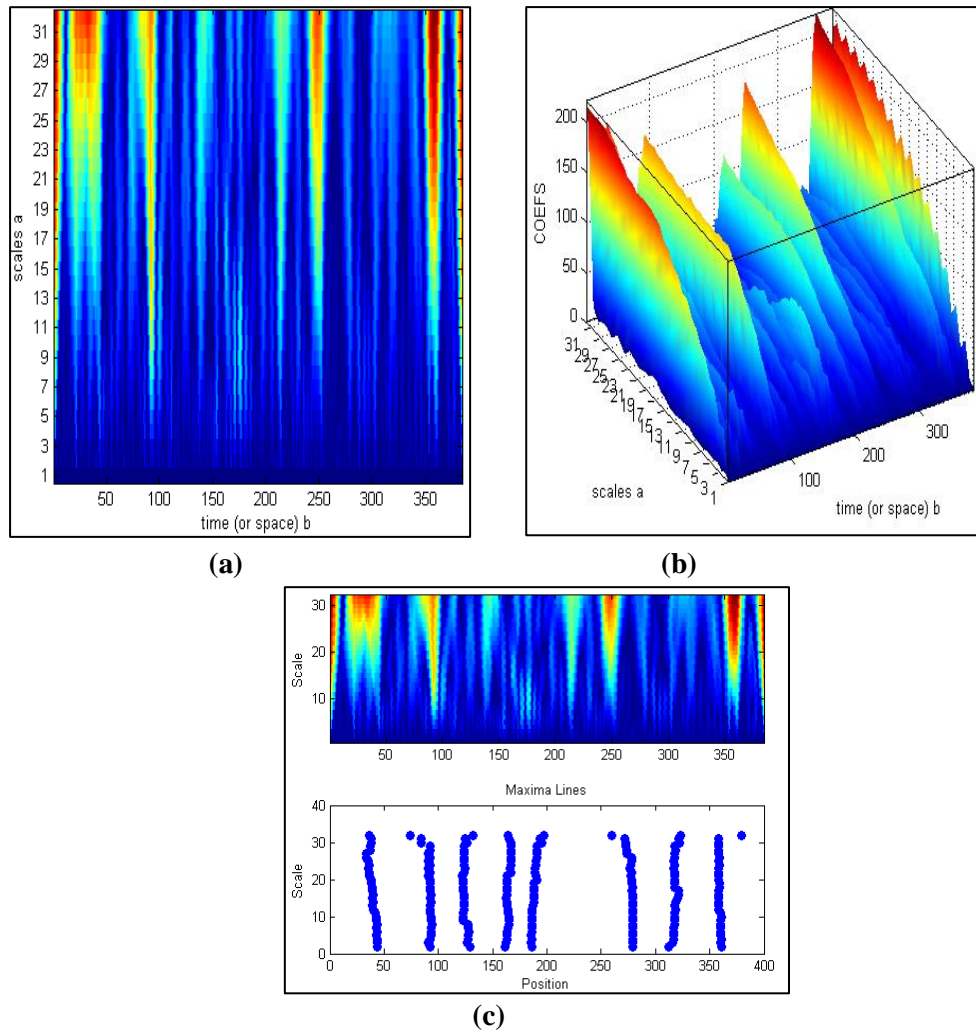
Figure 5.13 Results of Continuous Wavelet Transform on North Pole MiniSAR image

43

The continuous wavelet coefficients have been visualized as 3D plot and surface plot. At lower value of s the image is compressed and high frequency (fine) details of the features (craters) are achieved. At higher value of s the image gets stretched and low frequency (coarse) details of the features are achieved. Figure 5.13 (a) shows the abrupt changes occurred in the North Pole MiniSAR image in time-scale domain. These changes are due to the edges of craters. CWT finds the position of these changes with respect to scale varying from 1 to 32. Figure 5.13 (b) shows the 3-D plot of CWT, applied on the North Pole MiniSAR image, with third variable as CWT coefficients. Figure 5.13 (c) shows the position of lines of maxima with respect to the scale for North Pole MiniSAR image. The lines of maxima are calculated from the moduli of CWT coefficients.

- **Decomposition of South Pole MiniSAR image at scale (level) 1:**

(a)　　　　　　　　　　　**(b)**


(c)　　　　　　　　　　　**(d)**
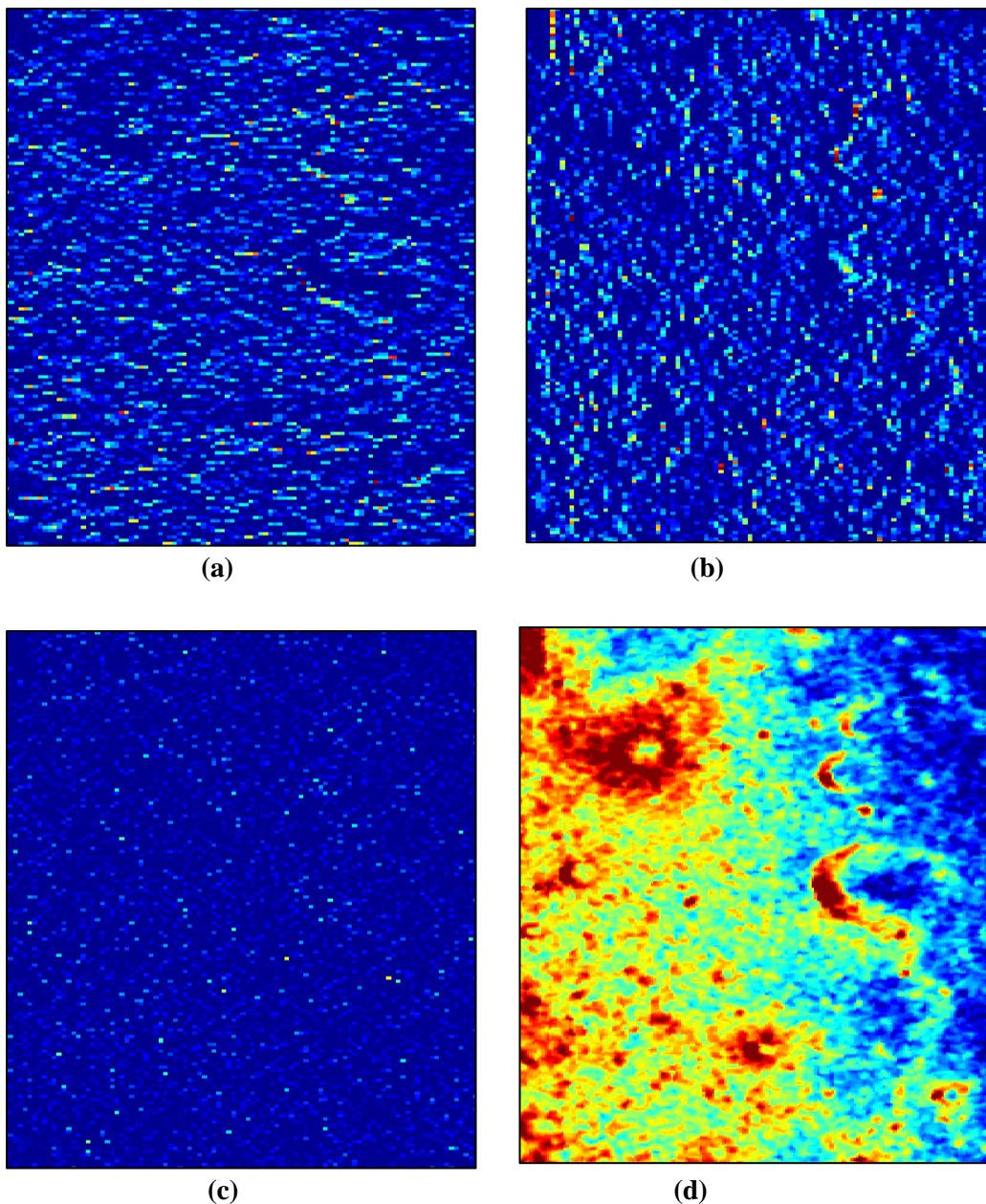
Figure 5.14 Results of Wavelet decomposition at scale 1 on South Pole MiniSAR image

The above results show the detected edges using Haar wavelet decomposition of the South Pole MiniSAR image at scale 1. Figure 5.14 (a) shows the horizontal coefficient obtained after wavelet decomposition at scale 1. The horizontal coefficient gives edge details in horizontal direction. Figure 5.14 (b) shows the vertical coefficient obtained after wavelet decomposition at scale 1. The vertical coefficient gives edge details in vertical direction. Figure 5.14 (c) shows the diagonal coefficient obtained after wavelet decomposition at scale 1. The diagonal coefficient gives diagonal edge details. Among all the three coefficients, vertical coefficient gives most clear and sharp edges. Figure 5.14 (d) shows the image reconstructed from the decomposition structure (matrix) at scale 1. The decomposition at scale 1 is giving the edge details at pixel level of the image and the shape of the craters is preserved.

- **Decomposition of South Pole MiniSAR image at scale (level) 2:**

(a)

(b)

(c)

(d)

Figure 5.15 Results of Wavelet decomposition at scale 2 on South Pole MiniSAR image

The above results show the detected edges using Haar wavelet decomposition of the South Pole MiniSAR image at scale 2. Figure 5.15 (a) shows the horizontal coefficient obtained after wavelet decomposition at scale 2. Figure 5.15 (b) shows the vertical coefficient obtained after wavelet decomposition at scale 2. Figure 5.15 (c) shows the diagonal coefficient obtained after wavelet decomposition at scale 2. Among all the three coefficients, vertical coefficient gives most clear and sharp edges. The coefficients obtained at scale 2 give lesser details than the coefficients at scale 1. Figure 5.15 (d) shows the image reconstructed from the decomposition structure (matrix) at scale 2. The decomposition at scale 2 gives lesser edge details at pixel level and at this scale of decomposition, shape of craters also got destroyed. Hence the craters are not detectable at scale 2.

- **Decomposition of South Pole MiniSAR image at scale (level) 3:**
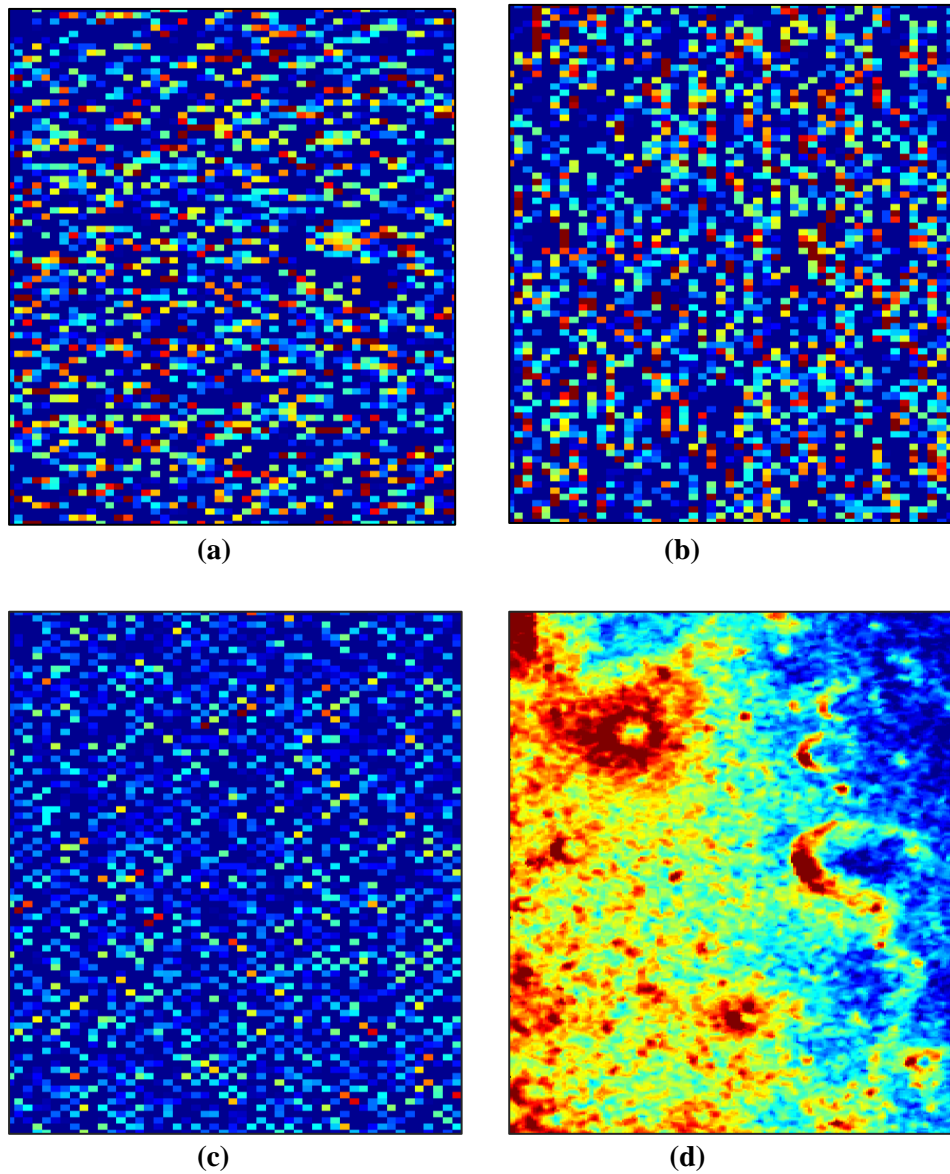

(a)

(b)

(c)

(d)
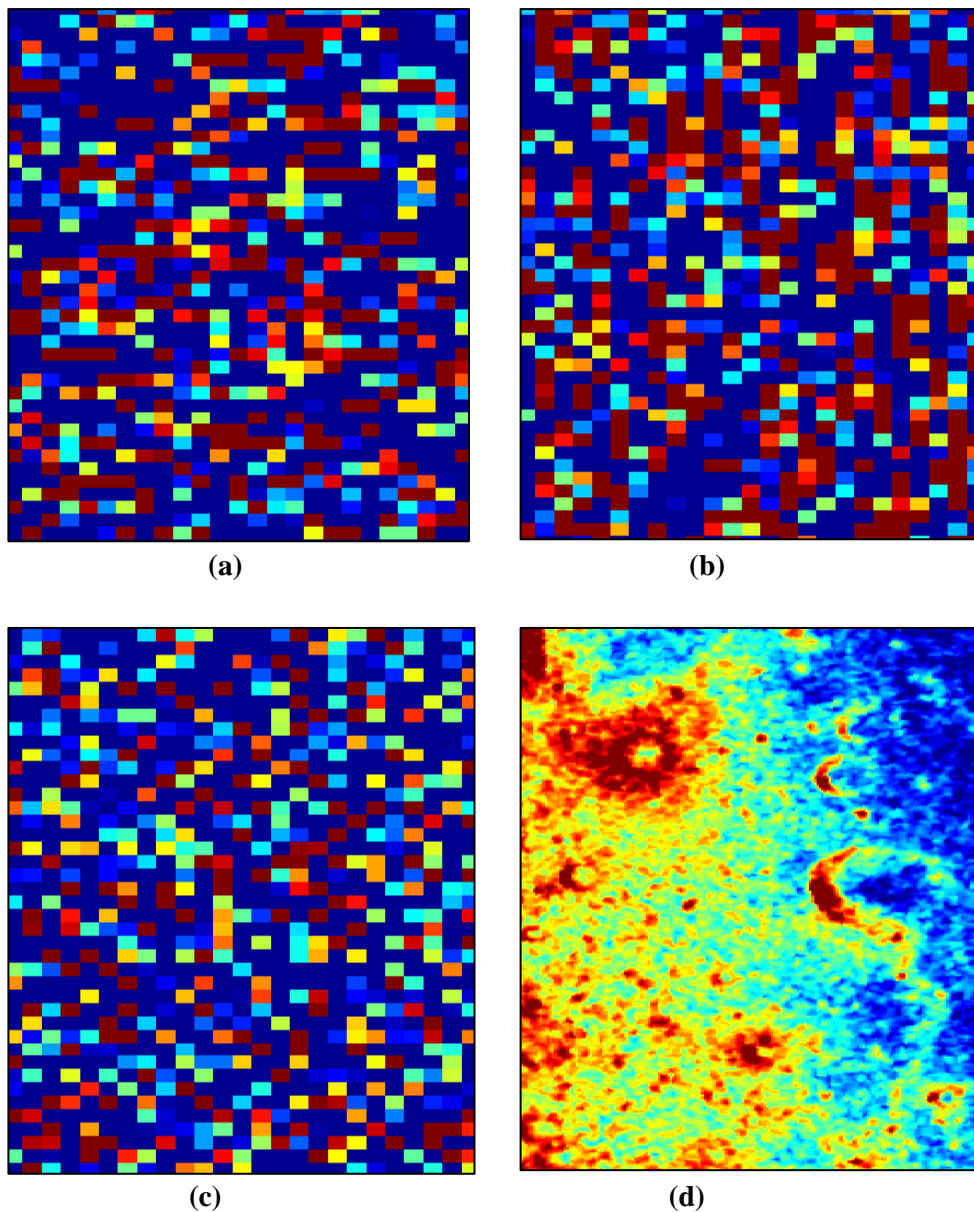
Figure 5.16 Results of Wavelet decomposition at scale 3 on South Pole MiniSAR image

The above results show the detected edges using Haar wavelet decomposition of the South Pole MiniSAR image at scale 3. Figure 5.16 (a) shows the horizontal coefficient obtained after wavelet decomposition at scale 3. Figure 5.16 (b) shows the vertical coefficient obtained after wavelet decomposition at scale 3. Figure 5.16 (c) shows the diagonal coefficient obtained after wavelet decomposition at scale 3. The coefficients obtained at scale 3 give lesser details than the coefficients at scale 1 and scale 2. Figure 5.16 (d) shows the image reconstructed from the decomposition structure (matrix) at scale 2. The decomposition at scale 3 gives lesser edge details at pixel level and at this scale of decomposition, shape of craters also got more destroyed. Hence the craters are not detectable at scale 3.

As the scale of decomposition increases, edge details are less and the shape of craters is also getting destroyed. Hence the craters in the South Pole MiniSAR image are not detectable at scale larger than 1. Craters of South Pole MiniSAR image are best detected at level 1 with the preservation of their shapes.

- **Continuous Wavelet Transform (CWT) of South Pole MiniSAR image:**

(a)   (b)

(c)
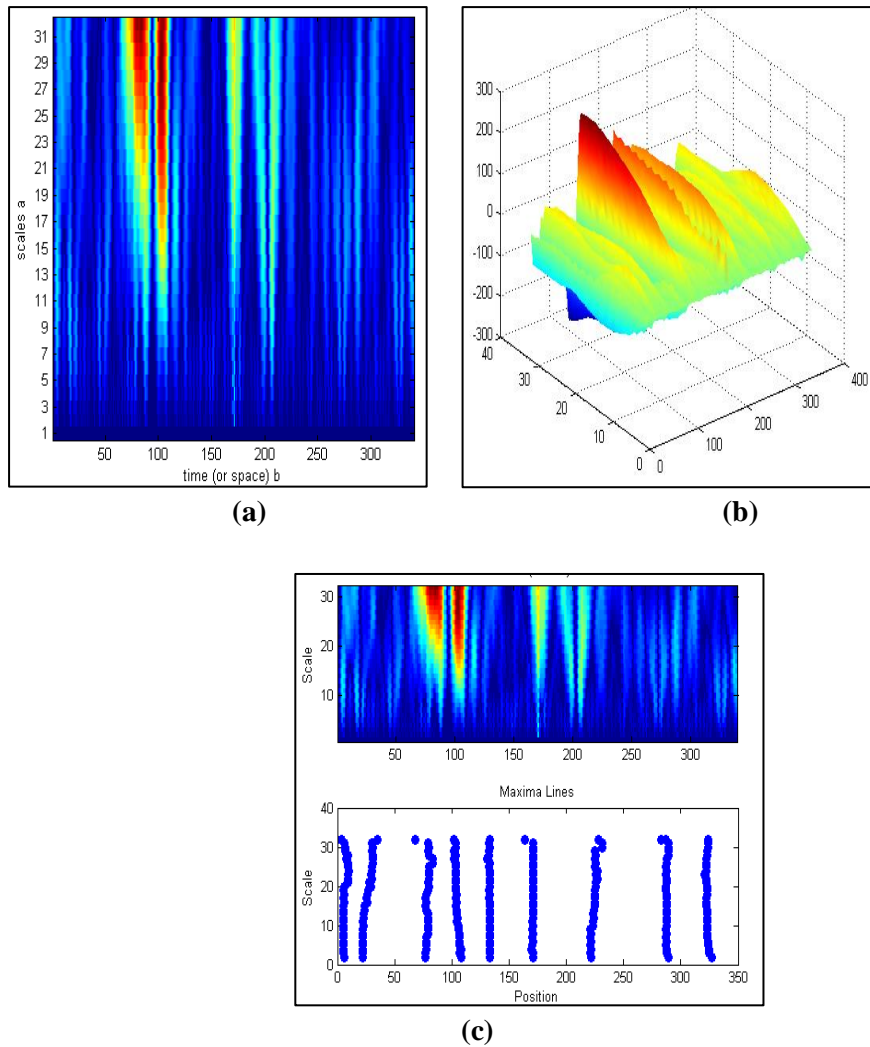
Figure 5.17 Results of Continuous Wavelet Transform on South Pole MiniSAR image

47

The continuous wavelet coefficients have been visualized as 3D plot and surface plot. At lower value of s the image is compressed and high frequency (fine) details of the features (craters) are achieved. At higher value of s the image gets stretched and low frequency (coarse) details of the features are achieved. Figure 5.17 (a) shows the abrupt changes occurred in the South Pole MiniSAR image in time-scale domain. These changes are due to the edges of craters. CWT finds the position of these changes with respect to scale varying from 1 to 32. Figure 5.17 (b) shows the 3-D plot of CWT, applied on the South Pole MiniSAR image, with third variable as CWT coefficients. Figure 5.17 (c) shows the position of lines of maxima with respect to the scale for South Pole MiniSAR image. The lines of maxima are calculated from the moduli of CWT coefficients.

5.2.2 Generalized Hough Transform

(a)

(b)

(c)

(d)
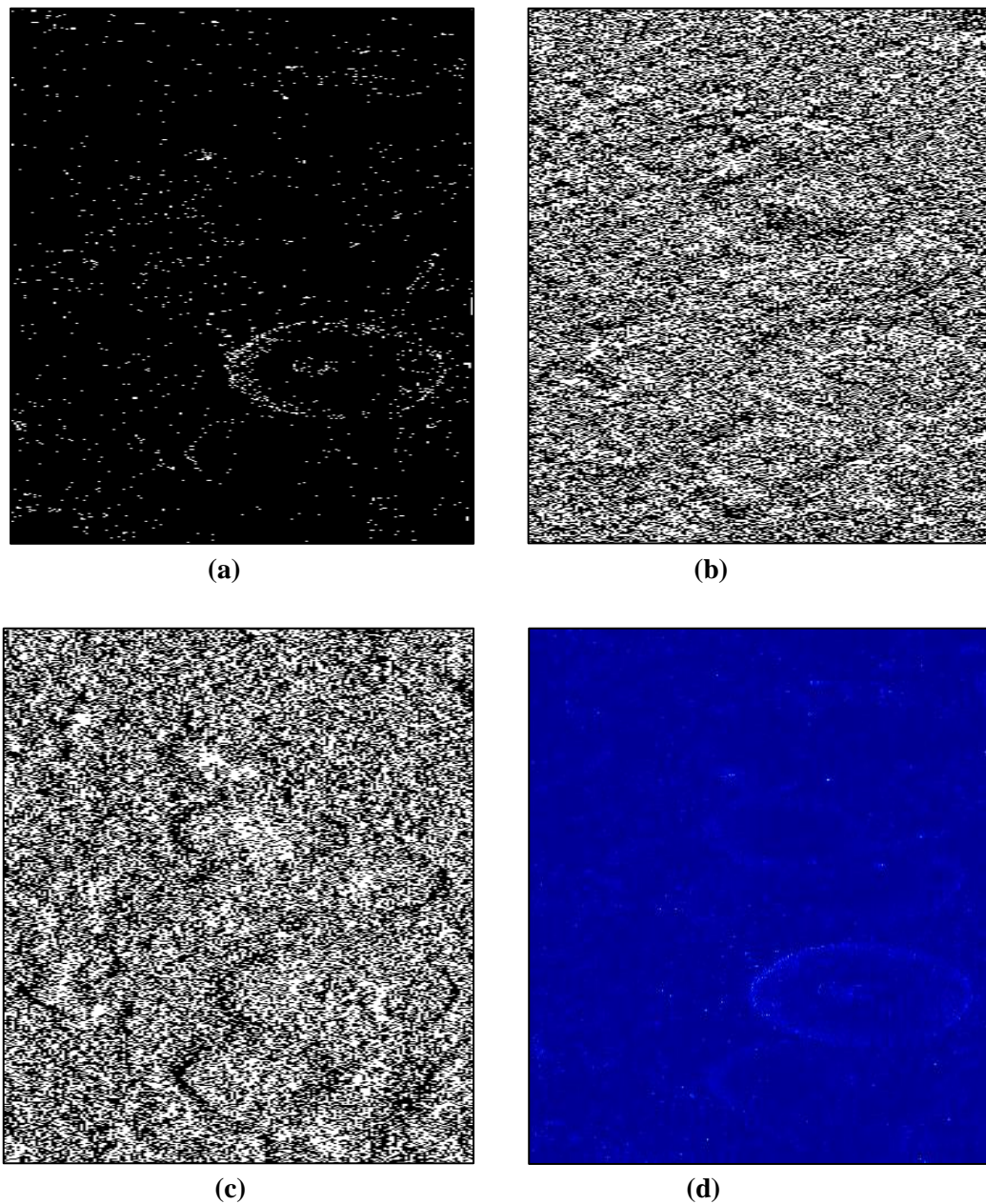
Figure 5.18 Results of Generalized Hough Transform on TMC image

These are the results of Generalized Hough Transform applied on TMC image. Figure 5.18 (a) shows all the edges of craters of TMC image. These edges are detected using Sobel edge detector. These edges are sparse means they are not linked. Figure 5.18 (b) shows the horizontal component of the detected edges of TMC image. The horizontal component shows the edges in horizontal direction of the image. Figure 5.18 (c) shows the vertical component of the detected edges of TMC image. The vertical component shows the edges in vertical direction of the image. Figure 5.18 (a), (b), (c) show the intermediate results of Generalized Hough Transform. Figure 5.18 (d) shows the final result of Generalized Hough Transform on TMC image. In the final result, all the edges are linked (grouped) by Hough Tranform. Thus the image got segmented and hence the craters have been detected in TMC image using image segmentation technique (Generalized Hough Transform).

(a)

(b)

(c)

(d)
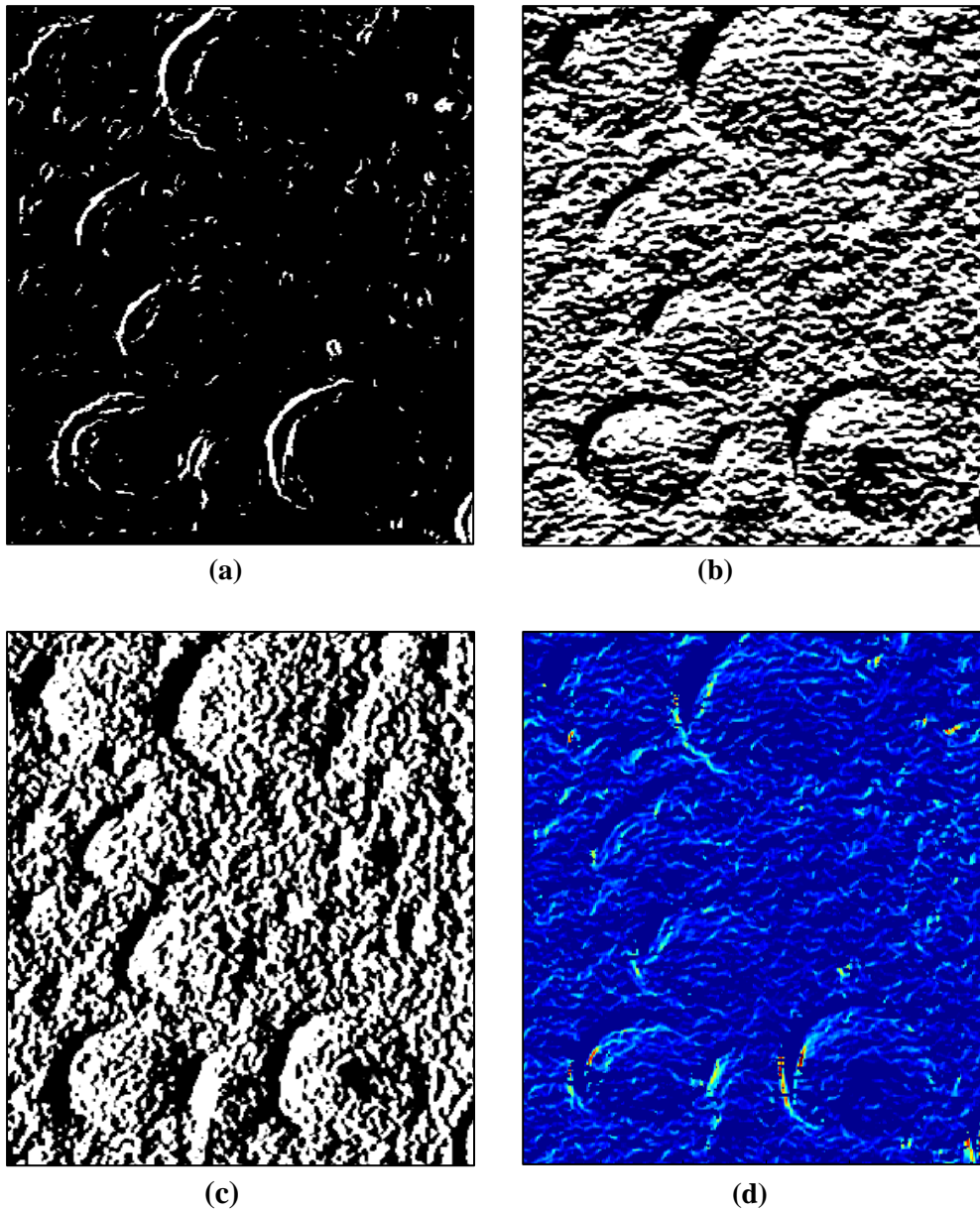
Figure 5.19 Results of Generalized Hough Transform on North Pole MiniSAR image

These are the results of Generalized Hough Transform applied on the North Pole MiniSAR image. Figure 5.19 (a) shows all the edges of craters of North Pole MiniSAR image.These edges are detected using Sobel edge detector. These edges are sparse means they are not linked. Figure 5.19 (b) shows the horizontal component of the detected edges of North Pole MiniSAR image.The horizontal component shows the edges in horizontal direction of the image. Figure 5.19 (c) shows the vertical component of the detected edges of North Pole MiniSAR image. The vertical component shows the edges in vertical direction of the image. Figure 5.19 (a), (b) and (c) show the intermediate results of Generalized Hough Transform. Figure 5.19 (d) shows the final result of Generalized Hough Transform on North Pole MiniSAR image. In the final result, all the edges are linked (grouped) by Hough Tranform. Thus the image got segmented and hence the craters have been detected in North Pole MiniSAR image using image segmentation technique (Generalized Hough Transform).

(a)

(b)

(c)

(d)
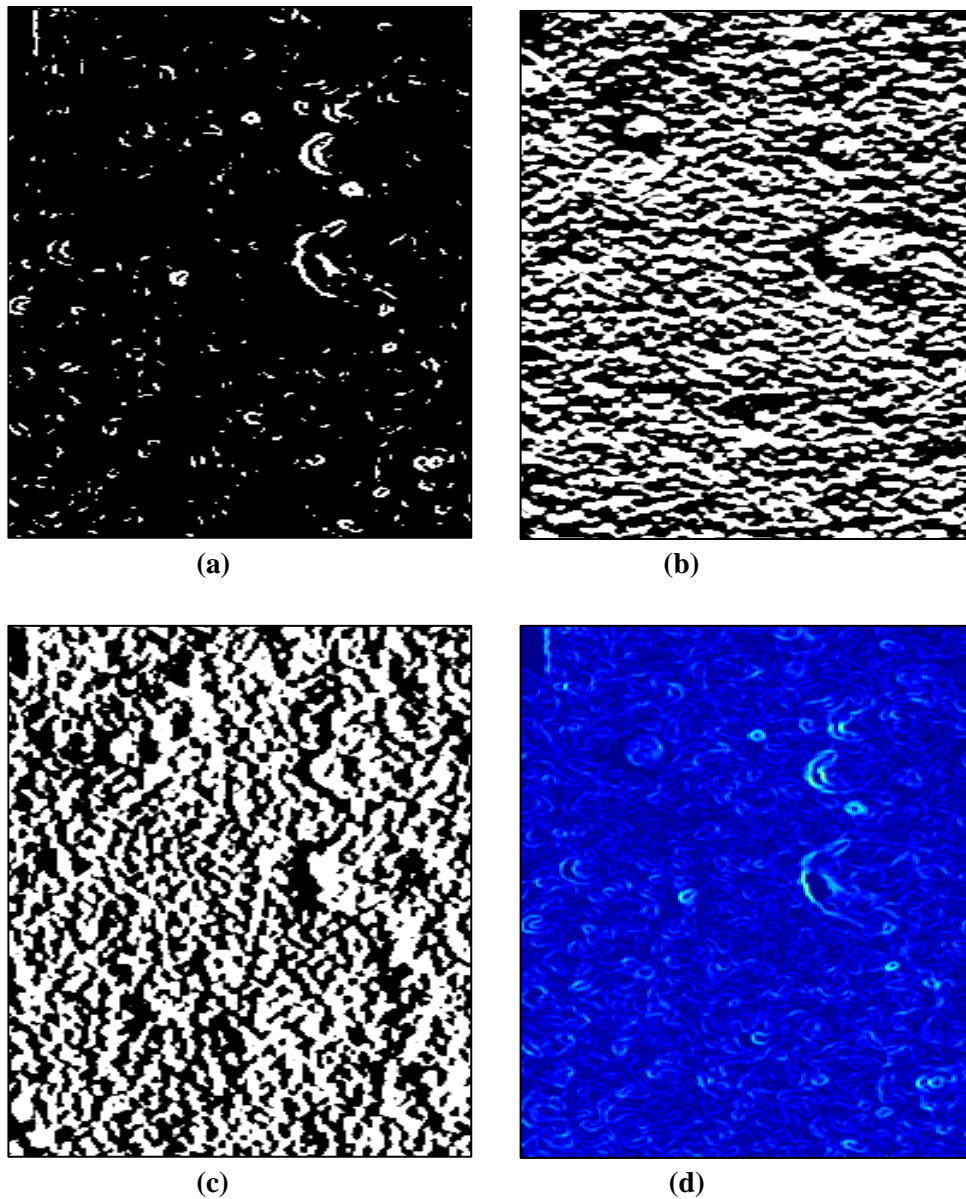
Figure 5.20 Results of Generalized Hough Transform on South Pole MiniSAR image

These are the results of Generalized Hough Transform applied on the South Pole MiniSAR image. Figure 5.20 (a) shows all the edges of craters of South Pole MiniSAR image.These edges are detected using Sobel edge detector. These edges are sparse means they are not linked. Figure 5.20 (b) shows the horizontal component of the detected edges of South Pole MiniSAR image.The horizontal component shows the edges in horizontal direction of the image. Figure 5.20 (c) shows the vertical component of the detected edges of South Pole MiniSAR image. The vertical component shows the edges in vertical direction of the image. Figure 5.20 (a), (b) and (c) show the intermediate results of Generalized Hough Transform. Figure 5.20 (d) shows the final result of Generalized Hough Transform on South Pole MiniSAR image. In the final result, all the edges are linked (grouped) by Hough Tranform. Thus the image got segmented and hence the craters have been detected in South Pole MiniSAR image using image segmentation technique (Generalized Hough Transform).

5.2.3 Watershed Transform

(a)

(b)

(c)

(d)

(e)

(f)

(g)

(h)
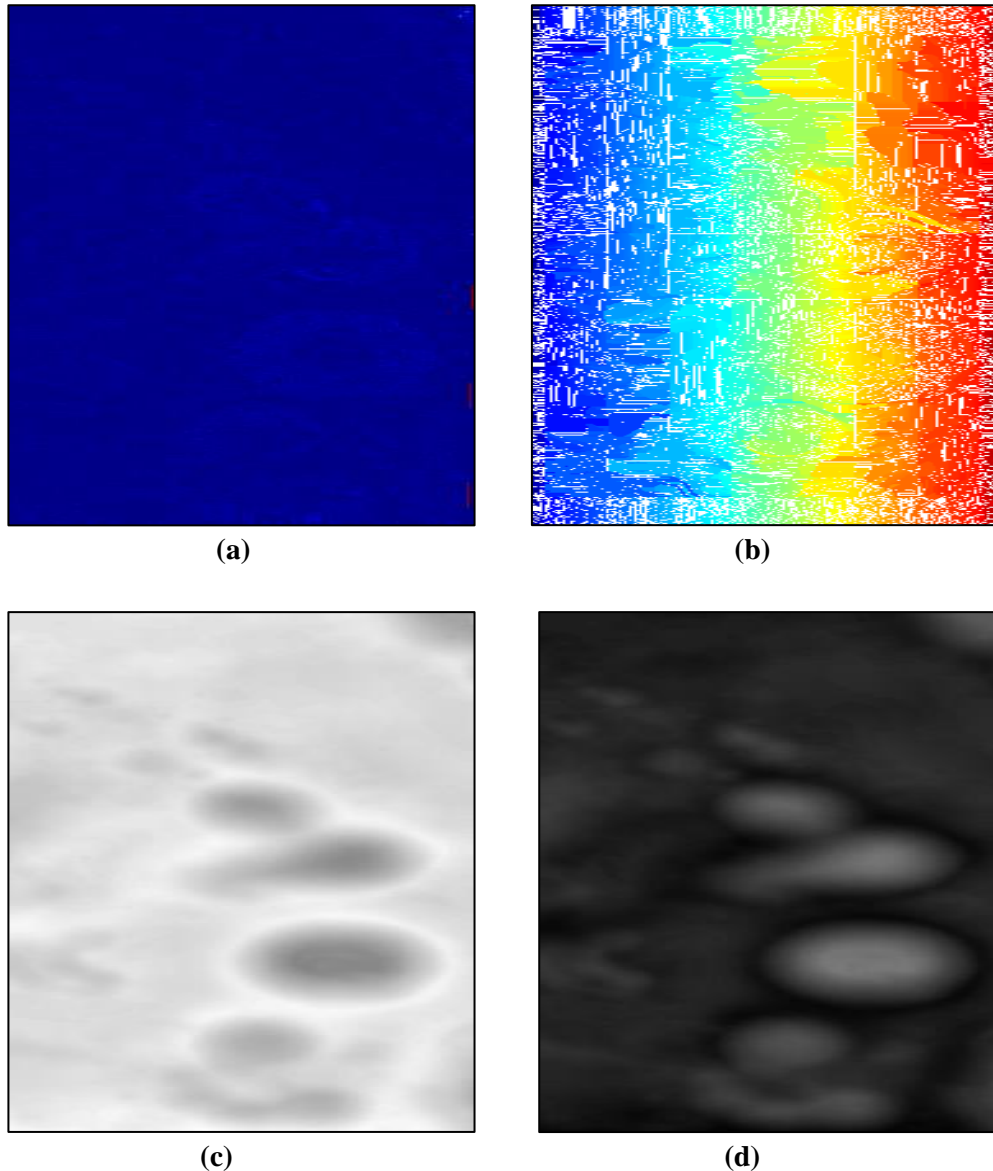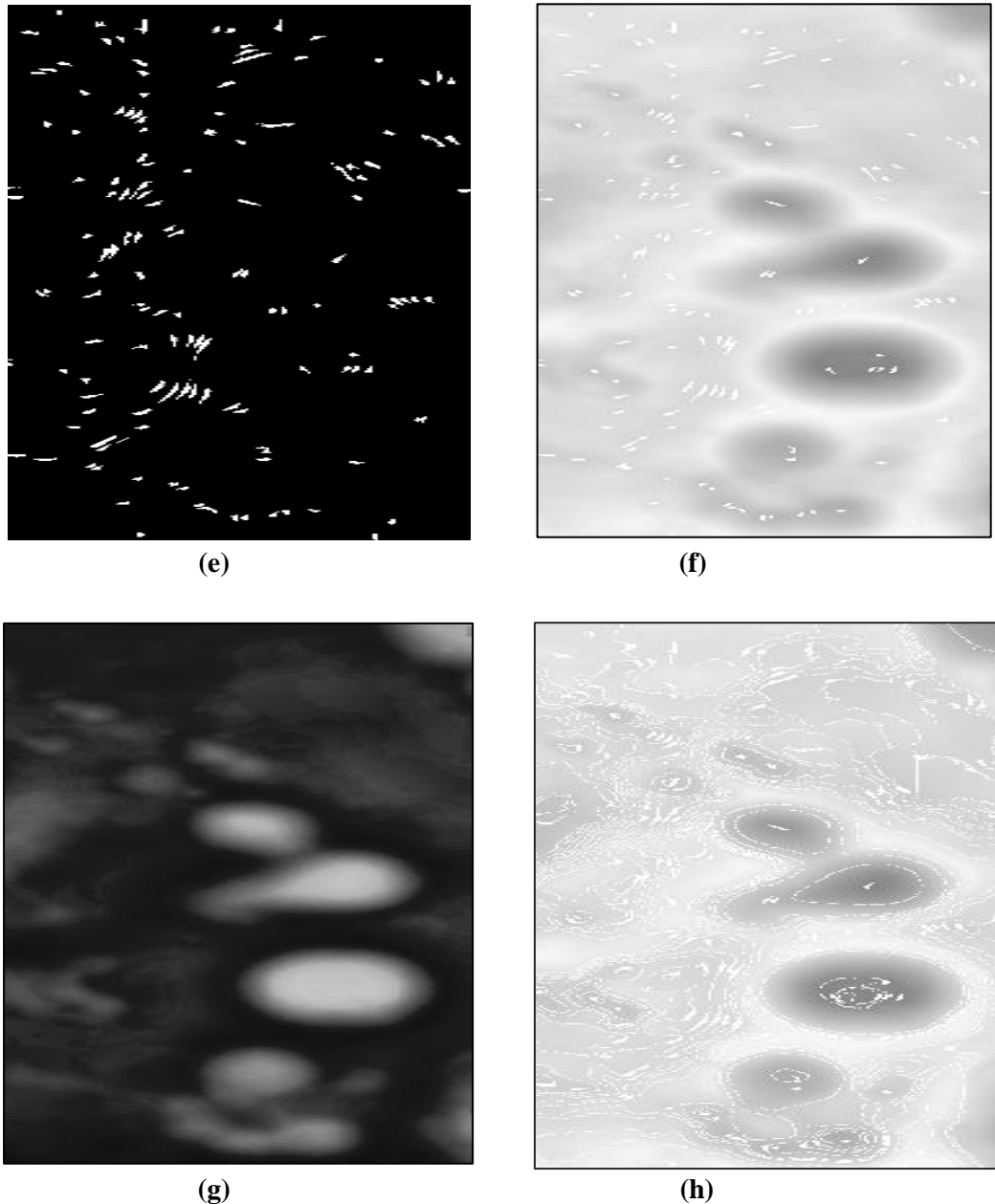
Figure 5.21 Results of Watershed Transform on TMC DEM

The Marker controlled watershed transformation has segmented the TMC DEM using the foreground and background markers. Figure 5.21 (a) shows the gradient magnitude, calculated by Sobel filter, as segmentation function. Figure 5.21 (b) shows the oversegmentation problem occurred due to watershed transformation of gradient magnitude image. Hence preprocessing like maker computations has been done to avoid this problem. Figure 5.21 (c) shows the result of the operation 'opening by reconstruction' which is an erosion followed by a morphological reconstruction It is used to mark the foreground objects (craters). Figure 5.21 (d) shows the result of 'opening-closing by reconstruction' wich is dilation followed by reconstruction. Reconstruction based opening and closing is

working without affecting the overall shapes of the objects. The foreground objects (connected blobs) are more clear in this image. Figure 5.21 (e) shows the regional maxima which is calculated to get the foreground markers. Figure 5.21 (f) shows the image of the foreground markers superimposed on the original image. Figure 5.21 (g) shows the thresholded binary image which is used for computing background markers. Finally the watershed transform has been computed. Figure 5.21 (h) shows the final result of watershed segmentation in which markers and object boundaries are superimposed on the TMC DEM.

5.2.4 Estimation of terrain derivatives

5.2.4.1 Slope and Aspect

(a)   (b)
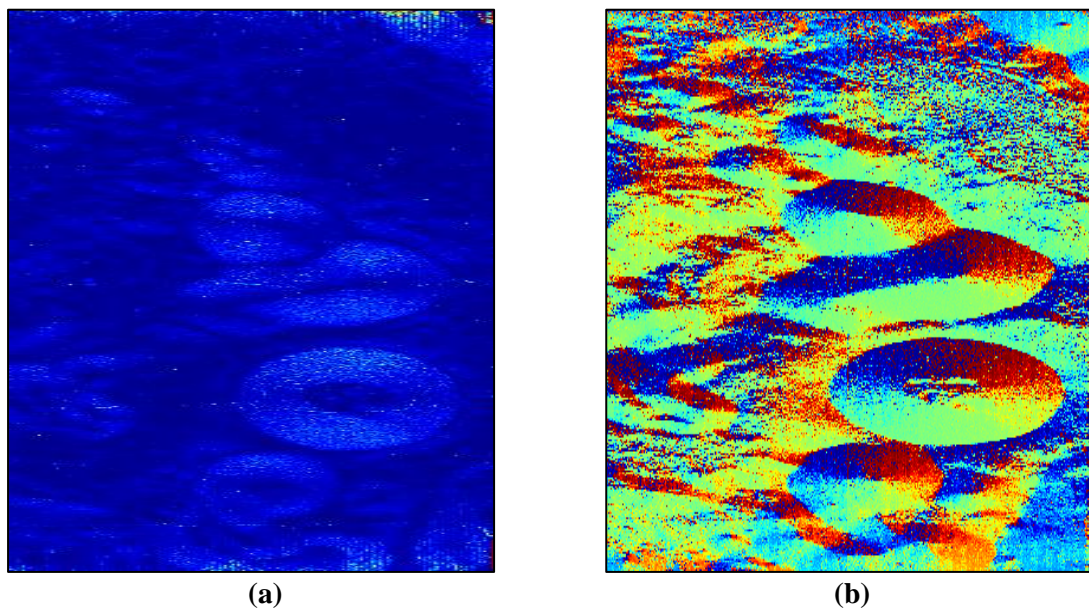
Figure 5.22 Results of Terrain Derivatives on TMC DEM

Figure 5.22 (a) shows the slope of TMC DEM. Figure 5.22 (b) shows the aspect of TMC DEM. The boundaries of the craters are very clearly defined by slope and aspect which have been estimated from TMC DEM. Hence craters have been detected with their clear boundaries using DEM derivatives (slope and aspect).

5.3 Decision

For the purpose of integration of image based and DEM based crater detection approaches, decision has been taken on the basis of edge strength and correlation coefficient for selecting one of the better image segmentation techniques used under both image based crater detection approach as well as DEM based crater detection approach.

5.3.1 Edge Strength

- **For Image based crater detection approach**

  The edge strength and edge density (normalized edge strength) have been calculated for image segmentation techniques (Wavelet Transform and Generalized Hough Transform) used under image based crater detection approach. Table 5.1 shows the values of edge strength and edge density.

Table 5.1 Values of edge strength and edge density for the output of image segmentation techniques under image based crater detection approach

Parameter	Wavelet Transform (Vertical coefficient at scale 3)	Generalized Hough Transform
Edge Strength	2244595.7	2048280349
Edge Density	24.18	350.90

From Table 5.1, the values of edge strength and edge density are higher for Generalized Hough Transform than the values for Wavelet Transform.

- **For DEM based crater detection approach**

  The edge strength and edge density (normalized edge strength) have been calculated for image segmentation techniques (Watershed Transform and Terrain Derivatives) used under DEM based crater detection approach. Table 5.2 shows the values of edge strength and edge density.

Table 5.2 Values of edge strength and edge density for the output of image segmentation techniques under DEM based crater detection approach

Parameter	Watershed Transform	Terrain Derivative (Aspect)
Edge Strength	328470	14783551
Edge Density	0.05	26.97

Table 5.2 shows that the values of edge strength and edge density are higher for Terrain Derivative than the values for Watershed Transform.

5.3.2 Image Details Preserving Coefficient (Correlation Coefficient)

- **For Image based crater detection approach**

  The correlation coefficient has been calculated between the results of image segmentation techniques (Wavelet Transform and Generalized Hough Transform) used under image based crater detection approach and the original image. Table 5.3 shows the values of correlation coefficient.

Table 5.3 Value of correlation coefficient for the output of image segmentation techniques under image based crater detection approach

Parameter	Wavelet Transform (Vertical coefficient at scale 3)	Generalized Hough Transform
Correlation Coefficient	0.05	-0.03

Table 5.3 shows that the value of correlation coefficient is higher for Wavelet Transform than the value for Generalized Hough Transform.

- **For DEM based crater detection approach**
  The correlation coefficient has been calculated between the results of image segmentation techniques (Watershed Transform and Terrain Derivatives) used under DEM based crater detection approach and the original DEM. Table 5.4 shows the values of correlation coefficient.

Table 5.4 Value of correlation coefficient for the output of image segmentation techniques under DEM based crater detection approach

Parameter	Watershed Transform	Terrain Derivatives (Aspect)
Correlation Coefficient	-0.03	0.32

Table 5.4 shows that the value of correlation coefficient is higher for Terrain Derivative than the value for Watershed Transform.

After evaluating the decision parameters under image based crater detection approach, it is found that the vertical coefficient of wavelet at scale 3 of TMC image show higher value of correlation coefficient as compared to that of Generalized Hough Transform. It means the image details of the original image are more preserved in the vertical coefficient at scale 3 than the details preserved by the Generalized Hough Transform. But the value of edge strength and edge density for Wavelet Transform, vertical coefficient at scale 3, is found lesser than the value for Generalized Hough Transform. It means that the edges are less strongly linked by the vertical coefficient at scale 3 as compared to that of the Generalized Hough Transform. Finally, the image details have been given more preference in this case and hence, vertical coefficient is selected as the better technique for integration purpose.

After evaluating the decision parameters under DEM based crater detection approach, it is found that Terrain Derivative, Aspect, of TMC DEM shows higher values of edge strength as well as correlation coefficient as compared to that of Watershed Transform technique. Hence, aspect is selected as the better technique for integration purpose.

5.4 Integration

The integrated approach of crater detection has been developed by integrating the result of crater detection using image and DEM. For this purpose, the result of Wavelet Transform technique under image based crater detection approach and the result of Terrain Derivatives

under DEM based crater detection approach have been integrated to do final detection of craters. These results act as inputs to the integration. The integration is done by multiplication of these inputs. Before doing integration, both these inputs have been converted into binary image format. Figure 5.23 (a) and (b) show the aspect and vertical coefficient of wavelet at level 3 respectively in binary image format. Hence both the binary images have been multiplied with each other and the output is the binary image of TMC shown in Figure 5.23 (c) with final craters detected. The multiplication is equivalent to the binary 'AND' operation.

(a) (b)

(c)
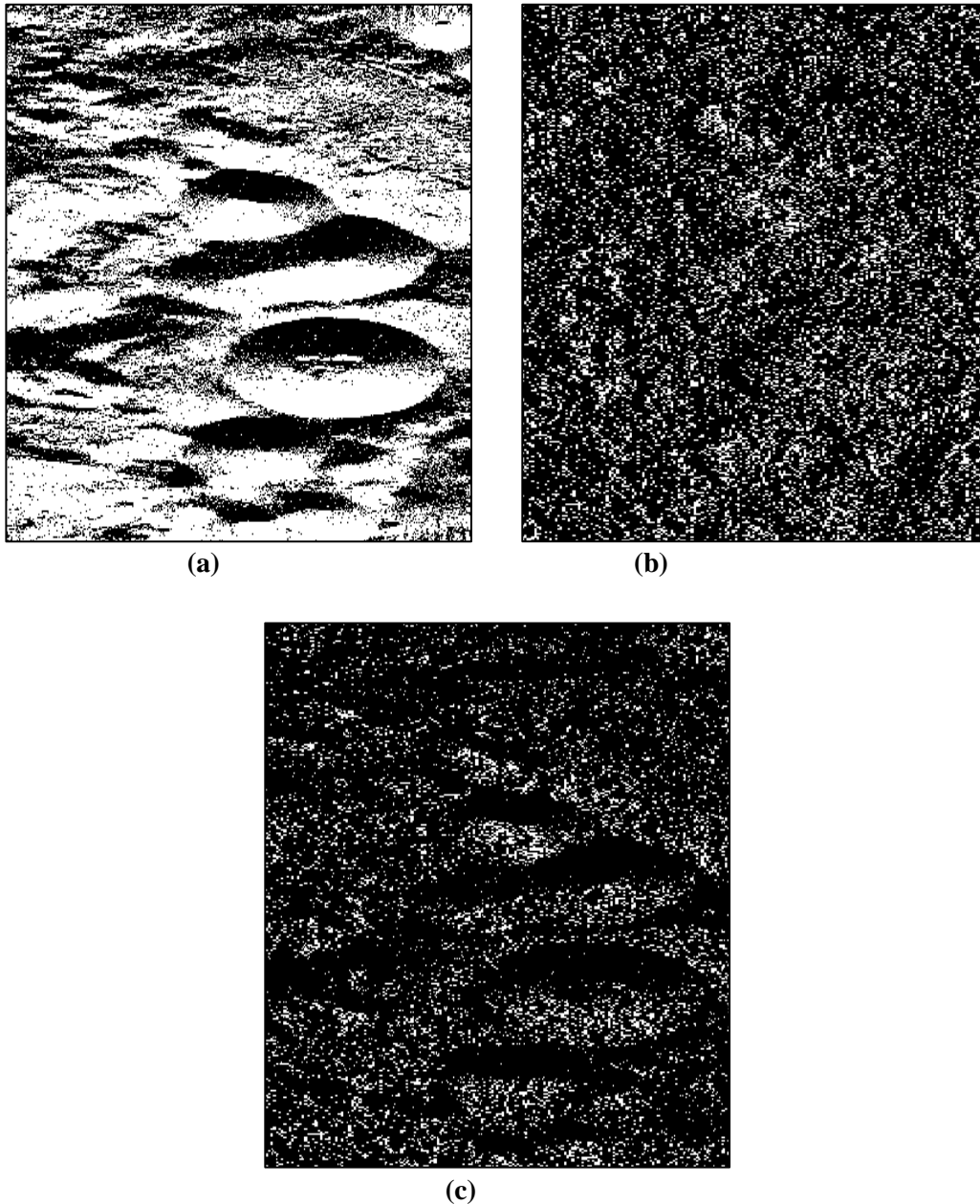
Figure 5.23 Results of Integration

5.5 Crater Attributes Measurement using Moment Measure Technique

5.5.1 Moment Measures

The shape and size attributes of crater have been computed using the moment measure technique in MATLAB. These attributes have been computed for the craters of the equatorial region as well as for the polar regions of moon. Hence the moment measure technique has been applied on the detected craters of TMC data and also on the North Pole and South Pole MiniSAR data.

- **For Equatorial Test site**

  The crater attributes for equatorial test site of moon have been shown in Table 5.5. Table 5.5 shows the values of shape and size attributes for different craters in the equatorial test site of moon.

Table 5.5 Crater attributes for equatorial test site of moon

Centroid		Diameter (m)	Eccentricity	Major Axis Length (m)	Minor Axis Length (m)	Area (pixel)
X (m)	Y (m)					
2.99E+02	5.92E+03	9.76E+02	**9.72E-01**	2.16E+03	5.05E+02	2.99E+04
2.56E+02	8.57E+03	3.60E+02	8.13E-01	4.91E+02	2.86E+02	4.08E+03
1.02E+03	9.71E+03	1.62E+03	8.62E-01	2.56E+03	1.30E+03	8.19E+04
3.58E+02	1.38E+04	8.33E+02	9.47E-01	1.65E+03	5.30E+02	2.18E+04
2.98E+02	1.52E+04	7.83E+02	9.41E-01	1.38E+03	4.67E+02	1.93E+04
2.91E+02	1.89E+04	6.89E+02	9.15E-01	1.10E+03	4.44E+02	1.49E+04
5.40E+02	4.61E+03	6.72E+02	8.73E-01	1.00E+03	4.88E+02	1.42E+04
5.84E+02	1.25E+03	3.99E+02	6.53E-01	4.81E+02	3.64E+02	5.00E+03
1.02E+03	2.95E+03	1.26E+03	9.05E-01	2.24E+03	9.52E+02	5.02E+04
4.68E+03	1.28E+04	**7.30E+03**	9.13E-01	1.63E+04	6.63E+03	1.68E+06
1.65E+03	1.91E+04	1.46E+03	7.78E-01	2.22E+03	1.39E+03	6.67E+04
2.11E+03	1.33E+04	1.16E+03	9.20E-01	2.33E+03	9.12E+02	4.21E+04
2.12E+03	5.70E+03	9.93E+02	8.32E-01	1.38E+03	7.65E+02	3.10E+04
3.24E+03	7.65E+01	**2.18E+02**	7.41E-01	2.73E+02	1.83E+02	1.49E+03
3.24E+03	3.22E+03	8.28E+02	3.69E-01	9.06E+02	8.42E+02	2.15E+04
3.01E+03	6.28E+03	3.49E+02	7.84E-01	4.51E+02	2.80E+02	3.82E+03
4.66E+03	2.30E+03	4.36E+02	4.68E-01	4.66E+02	4.12E+02	5.98E+03
4.71E+03	4.28E+03	4.08E+02	5.12E-01	4.48E+02	3.85E+02	5.23E+03
4.90E+03	1.07E+04	5.86E+02	8.39E-01	8.16E+02	4.43E+02	1.08E+04
5.61E+03	1.33E+04	8.26E+02	6.62E-01	1.35E+03	1.01E+03	2.14E+04
5.52E+03	1.33E+04	2.62E+02	7.46E-01	3.22E+02	2.14E+02	2.15E+03
6.49E+03	9.04E+02	1.70E+03	**2.97E-01**	1.97E+03	1.88E+03	9.05E+04
7.51E+03	2.41E+03	9.65E+02	9.14E-01	1.57E+03	6.37E+02	2.92E+04

Diameter and eccentricity describe the size and shape of craters respectively. Hence, the variation in the values of diameter and eccentricity parameters for different craters tells about the variation in the size and shape of craters in the equatorial test site of moon. From the Table 5.5, it clear that the size of craters varies from 218 m (0.22 km) to 7300 m (7 km). It means the equatorial region of the moon is having craters ranging from very small size to medium size. Similarly, the shape of the craters varies from 0.29 to 0.97. It means there are craters on the equatorial region having shape near circular to elliptical

- **For North Polar Test site**

   The same crater attributes have been computed for North Polar test site of moon shown in Table 5.6. Table 5.6 shows the values of shape and size attributes for different craters in the North Polar test site of moon. Diameter and eccentricity describe the size and shape of craters respectively. Hence, the variation in the values of diameter and eccentricity parameters for different craters tells about the variation in the size and shape of craters in the North Polar test site of moon. From the Table 5.6, it clear that the size of craters varies from 1610 m (1.6 km) to 13900 m (13.9 km). It means the north polar region of the moon is having craters ranging from small size to large size. Similarly, the shape of the craters varies from 0.36 to 0.93. It means there are craters on the North Polar Region having shape near circular to near elliptical.

Table 5.6 Crater attributes for North Polar test site of moon

Centroid		Diameter (m)	Eccentricity	Major Axis Length (m)	Minor Axis Length (m)	Area (pixel)
X (m)	Y (m)					
4.95E+03	2.66E+03	5.98E+03	**3.64E-01**	8.63E+03	8.03E+03	4.99E+03
1.04E+04	1.20E+04	**1.39E+04**	5.36E-01	2.36E+04	1.99E+04	2.68E+04
8.03E+03	2.26E+04	8.72E+03	8.56E-01	2.10E+04	1.09E+04	1.06E+04
5.80E+03	2.40E+04	4.08E+03	3.96E-01	4.38E+03	4.03E+03	2.33E+03
1.34E+04	2.79E+04	2.80E+03	8.76E-01	4.62E+03	2.23E+03	1.09E+03
1.61E+04	2.40E+04	5.25E+03	5.98E-01	5.95E+03	4.77E+03	3.85E+03
1.57E+04	5.31E+02	**1.61E+03**	8.64E-01	2.55E+03	1.29E+03	3.63E+02
1.92E+04	6.09E+03	7.89E+03	**9.33E-01**	1.40E+04	5.02E+03	8.70E+03
1.98E+04	2.65E+04	4.26E+03	8.96E-01	8.41E+03	3.74E+03	2.54E+03

- **For South Polar Test site**

   The same crater attributes have been computed for South Polar test site of moon shown   in Table 5.7. Table 5.7 shows the values of shape and size attributes for different craters in the South Polar test site of moon. Diameter and eccentricity describe the size and shape of craters respectively. Hence, the variation in the values of diameter and eccentricity parameters for different craters tells about the variation in the size and shape of craters in the South Polar test site of moon. From the Table 5.7, it clear that the size of craters varies from 1470 m (1.47 km) to 6360 m (6.36 km). It means the south polar region of the moon is having craters ranging from

small size to medium size. Similarly, the shape of the craters varies from 0 to 0.82. It means there are craters on the South Polar Region having shape circular to elliptical.

**Table 5.7** Crater attributes for South Polar test site of moon

Centroid		Diameter (m)	Eccentricity	Major Axis Length (m)	Minor Axis Length (m)	Area (pixel)
X (m)	Y (m)					
1.16E+03	2.01E+03	3.19E+03	7.07E-01	3.92E+03	2.77E+03	1.42E+03
1.28E+03	1.93E+04	3.43E+03	7.67E-01	4.70E+03	3.02E+03	1.64E+03
4.40E+03	5.25E+03	**6.36E+03**	7.88E-01	8.93E+03	5.49E+03	5.65E+03
3.92E+03	2.51E+04	**1.47E+03**	8.14E-01	1.97E+03	1.14E+03	3.00E+02
4.05E+03	1.44E+04	1.52E+03	**0.00E+00**	1.52E+03	1.52E+03	3.21E+02
7.04E+03	1.93E+04	4.14E+03	**8.16E-01**	5.59E+03	3.23E+03	2.39E+03
5.67E+03	9.93E+03	1.59E+03	2.30E-01	1.62E+03	1.58E+03	3.55E+02
7.03E+03	2.50E+04	1.55E+03	7.37E-01	1.94E+03	1.31E+03	3.35E+02
7.67E+03	1.48E+04	1.76E+03	3.05E-01	1.81E+03	1.73E+03	4.33E+02
1.10E+04	1.44E+04	3.52E+03	6.98E-01	4.55E+03	3.26E+03	1.73E+03
1.12E+04	2.40E+04	3.01E+03	4.10E-01	3.21E+03	2.93E+03	1.26E+03
1.14E+04	1.08E+04	1.91E+03	6.91E-01	2.26E+03	1.63E+03	5.10E+02
1.32E+04	2.17E+04	2.65E+03	6.26E-01	3.11E+03	2.43E+03	9.84E+02
1.30E+04	1.75E+04	1.69E+03	5.54E-01	1.86E+03	1.55E+03	3.97E+02

5.6 Surface Age Dating

The age of craters has been computed for the selected sites of Equatorial Region and Polar Regions of moon. Here, the age has been calculated on the basis of parameters (diameter and total area) of crater size frequency distribution (CSFD) calculated using Crater Tool as well as using Moment Measure Technique.

- **Age determination for equatorial test site using crater attributes**
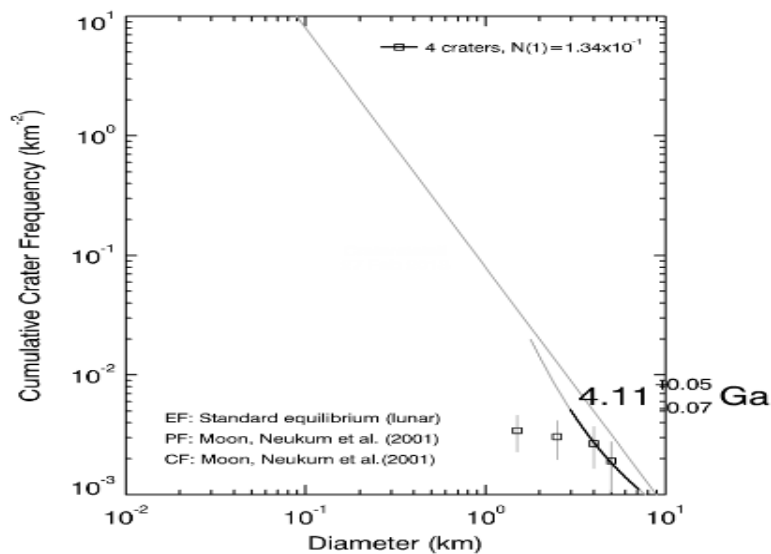 The equatorial test site age has been derived from the crater attributes obtained from the moment measures technique. The surface age plot from the moment measures techniques for the equatorial test site is shown in Figure 5.24. The age calculated for the equatorial test site is 1.32 Ga and the crater density (number of craters per unit area) is $1.10 * 10^{-3}$ per km^2.
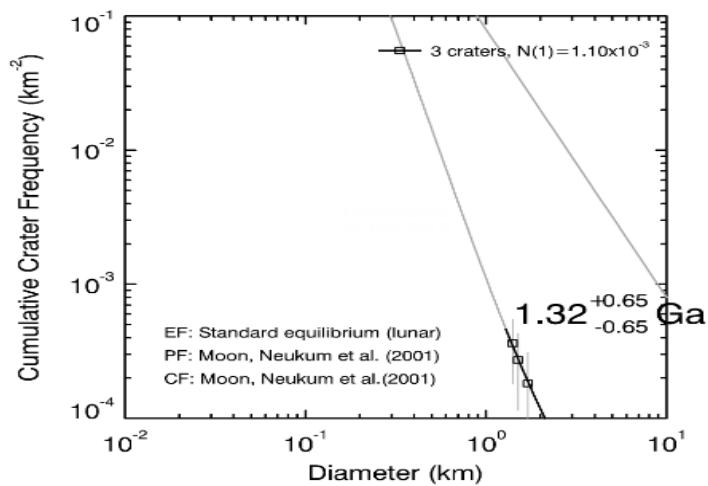
Figure 5.24 Age determination for equatorial test site

- **Age determination for north polar test site using crater attributes**
  The north polar test site age has been derived from the crater attributes obtained from the moment measures technique. The surface age plot from the moment measures techniques for the north polar test site is shown in Figure 5.25. The age calculated for the north polar test site is 4.11 Ga and the crater density (number of craters per unit area) is $1.34 * 10^{-1}$ per km^2.

Figure 5.25 Age determination for north polar test site

- **Age determination for south polar test site using crater attributes**
  The south polar test site age has been derived from the crater attributes obtained from the moment measures technique. The surface age plot from the moment measures techniques for the south polar test site is shown in Figure 5.26. The age calculated for the south polar test site is 3.95 Ga and the crater density (number of craters per unit area) is $4.64 * 10^{-2}$ per km^2.
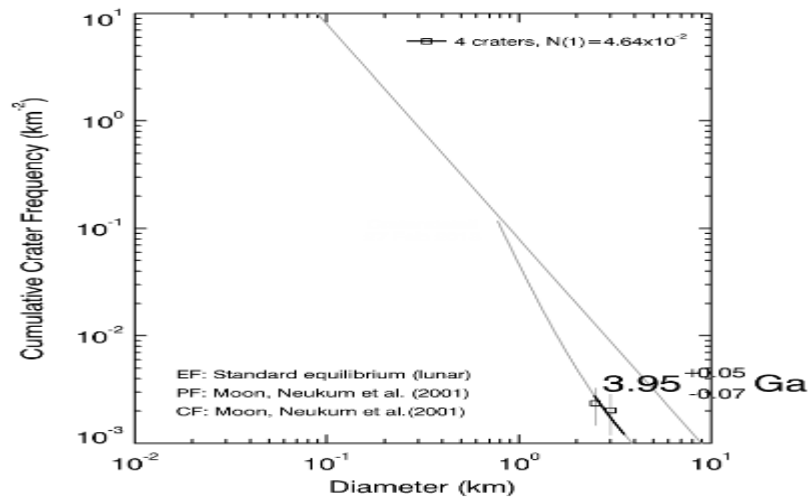
Figure 5.26 Age determination for south polar test site

Table 5.8 shows the age calculated for the Equatorial test site and Polar test sites (North Pole and South Pole) of moon.

Table 5.8 Derived ages for all the three test sites of moon:

Test Site	Number of craters	Diameter (km)		Total Area (km²)	Age (Ga)	
		Crater Tools	Moment Measures		Crater Tools	Moment Measures
Equatorial	23	0.4 - 6.5	0.26 - 7	0.11013E+05	1.50	1.32
North Pole	09	3 - 11	1.6 - 13.9	0.26177E+04	4.32	4.11
South Pole	14	1.9 - 4.5	1.4 - 6.3	0.29643E+04	4.10	3.95

From Table 5.8, it is clear that the age of the north polar test site of moon is highest and it is lowest for the equatorial test site. It means the lunar surface for the north polar test site is oldest while it is youngest for the equatorial test site.

5.7 Validation

The ages derived using Crater Tool and Moment Measure technique are compared with the USGS map as shown in Table 5.9.

Table 5.9 Comparison between derived ages and ages from USGS map

Test Site	Crater Tool	Moment Measures	USGS Map
Equatorial	1.50 Ga	1.32 Ga	None
North Pole	4.32 Ga	4.11 Ga	3.92 - 4.53 Ga
South Pole	4.10 Ga	3.95 Ga	3.92 - 4.53 Ga

6 Conclusions and Recommendations

6.1 Conclusions

The study confines to the following objectives: (a) Detection of craters automatically, (b) Morphological attributes measurement, (c) Analysis of spatial variation in the shape, size and density of impact craters over the lunar surface, (d) Analysis of variation in lunar surface age for selected test sites. This chapter summarizes the findings obtained from the adopted techniques and answers to the relevant research questions.

(a) **Which algorithm is best suited for image-based and topography-based crater detection?**

Image based crater detection has been done using Wavelet Transform and Generalized Hough Transform techniques. As per the decision parameters calculated for the results obtained from these two techniques, Wavelet Transform is best suited for image based crater detection. Topography (DEM) based crater detection has been done using Marker Controlled Watershed Transformation and Terrain (DEM) Derivatives. As per the decision parameters calculated for these two techniques, Terrain Derivatives are best suited for topography based crater detection.

(b) **How efficiently the regional descriptor based algorithm work for automatic retrieval of crater shape and size?**

Crater attributes (shape, size) have been computed using Moment Measure technique which uses the concept of regional shape descriptor. The algorithm based on this technique retrieved nine parameters (centroid, diameter, eccentricity, major axis length, minor axis length, perimeter, area, orientation, extent) for the craters in the image automatically. On the basis of the attributes like diameter and area, lunar surface age has been achieved successfully.

(c) **What is the spatial variation pattern of crater shape, size and density for the selected test sites over the lunar surface?**

As per the results, the shape of the craters on the lunar surface is found circular, near circular and near elliptical. The size (diameter) varies from 0.26 km to 7 km for the equatorial test site, 1.6 km to 13.9 km for the north polar test site and 1.4 km to 6.3 km for the south polar test site. As per the results, the crater density is highest for the north polar test site and lowest for the equatorial test site.

(d) **How does the age vary for the selected test sites over the lunar surface?**

Higher is the crater density, higher is the age. Lower is the crater density, lower is the age. As per the results, the lunar surface for the equatorial test site is youngest while it is oldest for the north polar test site. The age of south polar test site is in between the age of equatorial test site and north polar test site means it is middle aged.

6.2 Recommendations

Some limitations are there for which recommendations have been suggested for the future improvement in this work.

- Shadow is a major issue while retrieving the shape of craters from optical images. Shape retrieval of craters from the optical image (TMC image) can be improved by applying shape from shadow (SFS) technique.
- Microwave (MiniSAR) image and DEM can be used for detecting craters from polarimetric data using the integrated approach.
- Craters can be detected with more accuracy and details by fusion of multisensor data like optical (TMC) and microwave (MiniSAR) data.
- The Lee or Frost filter can be used as noise filters for better removal of speckle noise from SAR images.
- The microwave (MiniSAR) data has problems of layover and foreshortening which create problems in retrieving correct boundary (shape) of craters. These problems can be sorted out using ISIS (Integrated Software for Imagers and Spectrometers) software which is planetary image processing software.

References:

AL-HALABI, Y.S., ABD, H.J., 2005. New Wavelet based techniques for edge detection.8, 9.

Arya, A.S., Rajasekhar, R.P., Thangjam, G., Gujrati, A., Amitabh, S.T., Trivedi, S., Krishna, B.G., Ajai, Kumar, A.S., 2012. Lunar surface age determination using Chandrayaan-1 TMC data. Curr. Sci. 102, 783–788.

Ballard, D.H., 1981. Generalizing the Hough transform to detect arbitrary shapes. Pattern Recognit. 13, 111–122.

Barata, T., Alves, E.I., Saraiva, J., Pina, P., 2004. Automatic recognition of impact craters on the surface of Mars, in: Image Analysis and Recognition. Springer, pp. 489–496.

Benz, U.C., Hofmann, P., Willhauck, G., Lingenfelder, I., Heynen, M., 2004. Multi-resolution, object-oriented fuzzy analysis of remote sensing data for GIS-ready information. Isprs J. Photogramm. Remote Sens. 58, 239–258.

Beucher, S., 1992. The watershed transformation applied to image segmentation. Scanning Microsc.-Suppl.- 299–299.

Beveridge, J.R., Griffith, J., Kohler, R.R., Hanson, A.R., Riseman, E.M., 1989. Segmenting images using localized histograms and region merging. Int. J. Comput. Vis. 2, 311–347.

Bhagwat, M., Krishna, R.K., Pise, V., 2010. Simplified watershed transformation. Int. J. Comput. Sci. Commun. 1, 175–177.

Bijaoui, A., Slezak, E., Rué, F., Lega, E., 1996. Wavelets and the study of the distant Universe. Proc. Ieee 84, 670–679.

Blaschke, T., 2010. Object based image analysis for remote sensing. Isprs J. Photogramm. Remote Sens. 65, 2–16.

Bruzzone, L., Lizzi, L., Marchetti, P.G., Earl, J., Milnes, M., 2004. Recognition and detection of impact craters from EO products. Proc. Esa-Eusc.

Bue, B.D., Stepinski, T.F., 2007. Machine detection of martian impact craters from digital topography data. Geosci. Remote Sens. Ieee Trans. 45, 265–274.

Cheng, Y., Johnson, A.E., Matthies, L.H., Olson, C.F., 2003. Optical landmark detection for spacecraft navigation, in: In Proceedings of the 13th Annual AAS/AIAA Space Flight Mechanics Meeting.

Dey, V., Zhang, Y., Zhong, M., 2010. A review on image segmentation techniques with remote sensing perspective, in: Proceedings of the International Society for Photogrammetry and Remote Sensing Symposium (ISPRS10). pp. 5–7.

Earl, J., Chicarro, A.F., Koeberl, C., Marchetti, P.G., Milnes, M., 2005. Automatic recognition of crater-like structures in terrestrial and planetary images, in: 36th Annual Lunar and Planetary Science Conference. p. 1319.

Evans, I., 1980. An integrated system of terrain analysis and slope mapping. Z. Geomorphol. Suppl. Bd. 36, 274–295.

Gao, H., Siu, W.-C., Hou, C.-H., 2001. Improved techniques for automatic image segmentation. Circuits Syst. Video Technol. Ieee Trans. 11, 1273–1280.

Gao, H., Xue, P., Lin, W., 2004. A new marker-based watershed algorithm, in: Circuits and Systems, 2004. ISCAS'04. Proceedings of the 2004 International Symposium On. pp. II–81.

Gonzalez, R.C. and Paul Wintz (1977), Digital image processing. Second Edition. Addison-Wesley Publishing Company, 1977.

Gonzalez, R.C., Woods, R.E., Eddins, S.L., 2009. Digital image processing using MATLAB. Gatesmark Publishing Knoxville.

Guindon, B., 1997. Computer-based aerial image understanding: A review and assessment of its application to planimetric information extraction from very high resolution satellite images. Can. J. Remote Sens. 23, 38–47.

Hartmann, W.K., 1966. Early lunar cratering. Icarus 5, 406–418.

Haruyama, J., Ohtake, M., Matsunaga, T., Morota, T., Honda, C., Yokota, Y., Abe, M., Ogawa, Y., Miyamoto, H., Iwasaki, A., 2009. Long-lived volcanism on the lunar farside revealed by SELENE terrain camera. Science 323, 905–908.

Honda, R., Iijima, Y., Konishi, O., 2002. Mining of topographic feature from heterogeneous imagery and its application to lunar craters, in: Progress in Discovery Science. Springer, pp. 395–407.

Hough, P.V., 1962. Method and means for recognizing complex patterns. 3,069,654.

Ivanov, B.A., 2001. Mars/Moon cratering rate ratio estimates. Space Sci. Rev. 96, 87–104.

Jähne, B., 2004. Practical handbook on image processing for scientific and technical applications.

Kim, J.R., Muller, J., van Gasselt, S., Morley, J.G., Neukum, G., 2005. Automated crater detection, a new tool for Mars cartography and chronology. Photogramm. Eng. Remote Sens. 71, 1205.

Kneissl, T., van Gasselt, S., Neukum, G., 2011. Map-projection-independent crater size-frequency determination in GIS environments—New software tool for ArcGIS. Planet. Space Sci. 59, 1243–1254.

Lai Ru., Xiangdong Liu and Fujio Ohkawa (2008), A Fast Template Matching Algorithm based on Central Moment of images for a digital Images. Proceeding of the 2008 IEEE, International Conference on information and Automation, pp- 596-600.

Le Feuvre, M., Wieczorek, M.A., 2011. Nonuniform cratering of the Moon and a revised crater chronology of the inner Solar System. Icarus 214, 1–20.

Legrand, C., Chevalley, P., 2013. Virtual Moon Atlas. Lpi Contrib. 1719, 1021.

Mallat, S. (1989), A theory for multiresolution signals decomposition: the wavelet representation, IEEE Pattern Anal. and Machine Intell., vol. 11, no. 7, pp. 674–693.

Michael, G.G., Neukum, G., 2010. Planetary surface dating from crater size–frequency distribution measurements: Partial resurfacing events and statistical age uncertainty. Earth Planet. Sci. Lett. 294, 223–229.

Mohan S., Das, A., Chakraborty, M., 2011. Studies of polarimetric properties of lunar surface using Mini-SAR data, Current Science, 101(2), 159-164.

Morota, T., Haruyama, J., Honda, C., Yokota, Y., Ohtake, M., Ogawa, Y., Matsunaga, T., 2008. Lunar cratering chronology: Statistical fluctuation of crater production frequency and its effect on age determination. Earth Planets Space 60, 265.

Neukum, G., Ivanov, B.A., Hartmann, W.K., 2001. Cratering records in the inner solar system in relation to the lunar reference system. Space Sci. Rev. 96, 55–86.

Oberbeck, V.R., Quaide, W.L., Arvidson, R.E., Aggarwal, H.R., 1977. Comparative studies of lunar, martian, and mercurian craters and plains. J. Geophys. Res. 82, 1681–1698.

Open discontdemo.m Matlab 2012(a) Help

Otsu, N., A Threshold Selection Method from Gray-Level Histograms, IEEE Transactions on Systems, Man, and Cybernetics, Vol. 9, No. 1, 1979, pp. 62-66.

Pal, N.R., Pal, S.K., 1993. A review on image segmentation techniques. Pattern Recognit. 26, 1277–1294.

Pham, D.L., Xu, C., Prince, J.L., 2000. Current methods in medical image segmentation 1. Annu. Rev. Biomed. Eng. 2, 315–337.

Plesko, C., Brumby, S., Asphaug, E., Chamberlain, D., Engel, T., 2004. Automatic crater counts on Mars, in: Lunar and Planetary Institute Science Conference Abstracts. p. 1935.

Qiu, F., Berglund, J., Jensen, J.R., Thakkar, P., Ren, D., 2004. Speckle noise reduction in SAR imagery using a local adaptive median filter. Giscience Remote Sens. 41, 244–266.

R. K. Raney (2006), Dual-Polarized SAR and Stokes Parameters, IEEE Geoscience and Remote Sensing Letters, Vol. 3, Issue. 3, July 2006, 317-319.

Salamuniccar, G., Loncaric, S., 2010. Method for crater detection from Martian digital topography data using gradient value/orientation, morphometry, vote analysis, slip tuning, and calibration. Geosci. Remote Sens. Ieee Trans. 48, 2317–2329.

Salamuniccar, G., Loncaric, S., Grumpe, A., Wohler, C., 2011. Hybrid method for detection of lunar craters based on topography reconstruction from optical images, in: Image and Signal Processing and Analysis (ISPA), 2011 7th International Symposium On. pp. 597–602.

Sawabe, Y., Matsunaga, T., Rokugawa, S., 2006. Automated detection and classification of lunar craters using multiple approaches. Adv. Space Res. 37, 21–27.

Schiewe, J., 2002. Segmentation of high-resolution remotely sensed data-concepts, applications and problems. Int. Arch. Photogramm. Remote Sens. Spat. Inf. Sci. 34, 380–385.

Spirkovska, L., 1993. A summary of image segmentation techniques. Citeseer.

Stepinski, T.F., Ding, W., Vilalta, R., 2012. Detecting Impact Craters in Planetary Images Using Machine Learning. Intell. Data Anal. Real-Life Appl. Theory Pr. Igi Glob. 146–159.

Stöffler, D., Ryder, G., 2001. Stratigraphy and isotope ages of lunar geologic units: Chronological standard for the inner solar system. Space Sci. Rev. 96, 9–54.

Tamililakkiya, V., 2011. Linear and Non-Linear Feature Extraction Algorithms for Lunar Images. Signal Image Process. Int. J. 2, 161–172.

Tanaka, K.L., 1986. The stratigraphy of Mars. J. Geophys. Res. Solid Earth 1978–2012 91, E139–E158.

Urbach, E.R., Stepinski, T.F., 2009. Automatic detection of sub-km craters in high resolution planetary images. Planet. Space Sci. 57, 880–887.

Vinogradova, T., Burl, M., Mjolsness, E., 2002. Training of a crater detection algorithm for Mars crater imagery, in: Aerospace Conference Proceedings, 2002. IEEE. pp. 7–3201.

Werner, S.C., Tanaka, K.L., 2011. Redefinition of the crater-density and absolute-age boundaries for the chronostratigraphic system of Mars. Icarus 215, 603–607.

Wetzler, P.G., Honda, R., Enke, B., Merline, W.J., Chapman, C.R., Burl, M.C., 2005. Learning to detect small impact craters, in: Application of Computer Vision, 2005. WACV/MOTIONS'05 Volume 1. Seventh IEEE Workshops On. pp. 178–184.

Wise,U.D.,& Minkowski, G., 1980. Dating methodology of small, homogeneous crater populations applied to the tempe-utopia trough region on Mars. Goddard Space Flight. Greenbelt: NASA

You, J., Bhattacharya, P., 2000. Dynamic shape retrieval by hierarchical curve matching, snakes and data mining, in: Pattern Recognition, 2000. Proceedings. 15th International Conference On. pp. 1035–1038.

Yue, Z., Liu, J., Wu, G., 2008. Automated detection of lunar craters based on object-oriented approach. Chin. Sci. Bull. 53, 3699–3704.

Zhang, D., Lu, G., 2004. Review of shape representation and description techniques. Pattern Recognit. 37, 1–19.

Zhang, X.-P., Desai, M.D., 1997. Wavelet based automatic thresholding for image segmentation, in: Image Processing, 1997. Proceedings., International Conference On. pp. 224–227.

Zhang, Y., Maxwell, T., Tong, H., Dey, V., 2010. Developement of Supervised Software Tool for Automated Determination of Optimal Segmentation Parameters for Ecognition, in: Proceedings of ISPRS TC VII Symposium-100 Years ISPRS.

Zhou, Q., Yu, S., Wu, X., Gao, Q., Li, C., Xu, Y., 2009. HMMs-based human action recognition for an intelligent household surveillance robot, in: Robotics and Biomimetics (ROBIO), 2009 IEEE International Conference On. pp. 2295–2300.